PROTRACTED THRUSTING FOLLOWED BY LATE RAPID COOLING

OF THE GREATER HIMALAYAN SEQUENCE, ANNAPURNA HIMALAYA,

CENTRAL NEPAL: INSIGHTS FROM TITANITE PETROCHRONOLOGY

by

Jesse Bennett Walters

A thesis

submitted in partial fulfillment

of the requirements for the degree of

Master of Science in Geology

Boise State University

August 2016

BOISE STATE UNIVERSITY GRADUATE COLLEGE

DEFENSE COMMITTEE AND FINAL READING APPROVALS

of the thesis submitted by

Jesse Bennett Walters

Thesis Title: Protracted Thrusting Followed by Late Rapid Cooling of the Greater Himalayan Sequence, Annapurna Himalaya, Central Nepal: Insights from Titanite Petrochronology

Date of Final Oral Examination: 20 April 2016

The following individuals read and discussed the thesis submitted by student Jesse Bennett Walters, and they evaluated his presentation and response to questions during the final oral examination. They found that the student passed the final oral examination.

Matthew J. Kohn, Ph.D.	Chair, Supervisory Committee
Sean P. Long, Ph.D.	Member, Supervisory Committee
C. J. Northrup, Ph.D.	Member, Supervisory Committee
V. Dorsey Wanless, Ph.D.	Member, Supervisory Committee

The final reading approval of the thesis was granted by Matthew J. Kohn, Ph.D., Chair of the Supervisory Committee. The thesis was approved for the Graduate College by Jodi Chilson, M.F.A., Coordinator of Theses and Dissertations.

DEDICATION

I want to dedicate this work to my grandmother, Sue Bartholomew, who passed away during the writing of this thesis. She was a kindhearted person and extremely supportive of my career in geology. I will miss rock hounding with you.

ACKNOWLEDGEMENTS

ABSTRACT

Temperature-time (T-t) paths derived from coupled Zr-in-titanite thermometry and U-Pb geochronology are useful for examining middle-crustal tectonic processes. T-t data collected from the titanite-bearing calcsilicates of the upper Greater Himalayan Sequence (GHS) along the Marsyandi River, Annapurna Himalaya, illustrate a significantly different metamorphic history than previously recorded in central Nepal. Combined with traditional thermobarometry, textural relationships, and field mapping, titanite T-t data reveal a protracted history of mid-crustal tectonics. Peak Zr-in-titanite temperatures are 750-850 °C at 10-14 kbar. T-t paths are divided into two groups, which are separated by the Chame Shear Zone (CSZ). Group I (upper) rocks show cooling at rates of 1-10 °C/Ma between ca. 25 and ca. 10 Ma, while Group II (lower) rocks show heating at rates of 1-10 °C/Ma over the same time interval. Between ca. 25 and ca. 15 Ma, a thermal inversion occurs structurally upwards through Group I, but by ca. 10 Ma temperatures decrease structurally upwards. In opposition, temperatures decrease upwards in Group II rocks at all times and are as high as ~830 °C at ca. 9 Ma. While Group II rocks are interpreted as an intact, structurally-upright, section, the thermometric inversion within Group I is interpreted as thrusting of hotter rocks over colder from ca. 25 to ca. 15 Ma. The thrusting interpretation is also supported by simultaneous cooling and heating of Group I and II rocks, lithologic repetition of orthogneiss at the CSZ, and retrograde water-rich fluid flux restricted to Group I rocks. The CSZ is structurally higher than previously-identified intra-GHS thrusts in central Nepal, and thrusting duration was

~3-6 Ma longer than proposed for other identified intra-GHS thrusts in this region. Thrusting was followed by cooling at ~ 60 °C/Ma from ca. 10 Ma to Ar closure in muscovite at ca. 3.8 Ma; however, ~ 55 km to the west, cooling rates were ~ 20 °C/Ma and muscovite $^{40}Ar/^{39}Ar$ cooling ages ca. 10-15 Ma. These data suggest considerable along-strike variation in the position and duration of thrusting, as well as subsequent cooling, in the Himalaya. Formation of the Lesser Himalayan duplex in the late Miocene may have played a more important role in cooling and unroofing the GHS in the Marsyandi sector than at other locations. Additionally, exhumation from ~ 40 km depth requires erosion rates of ≥ 4.0 mm/yr, comparable to modern rates, for the past 10 Ma. Sector zoning of Zr in titanite suggests that diffusion rates are slower than determined experimentally, preserving thermometric constraints for metamorphism into the lower granulite facies.

TABLE OF CONTENTS

LIST OF TABLES

LIST OF FIGURES

LIST OF ABBREVIATIONS

LHS	Lesser Himalayan Sequence
GHS	Greater Himalayan Sequence
THS	Tethyan Himalayan Sequence
MCT	Main Central Thrust
CSZ	Chame Shear Zone
STDS	South Tibetan Detachment System
Qtz	Quartz
Kfs	K-feldspar
Pl	Plagioclase feldspar
An	Anorthite
Scp	Scapolite
Me	Meionite
Cal	Calcite
Cam	Ca-Amphibole
Act	Actinolite
Tr	Tremolite
Hbl	Hornblende
Di	Diopside
Bt	Biotite
Phl	Phlogopite

Ep	Epidote
Zo	Zoisite
Ttn	Titanite
Rt	Rutile
Aln	Allanite
Ap	Apatite
Zrn	Zircon
Tur	Tourmaline
Grt	Garnet
T	Temperature
P	Pressure
t	Time
TZARS	Titanite, Zoisite, Anorthite, Rutile, Silica equilibrium reaction
BSE	Backscattered Electron Imaging
ICPMS	Inductively Coupled Plasma Mass Spectrometry

CHAPTER ONE: INTRODUCTION

Extreme uplift and erosion in the Himalaya provide a > 2000 km long window into upper, middle, and lower crustal processes, forming a natural laboratory for developing and testing tectonic models. Shortening in the Himalayan orogen for the last 50-55 Ma (Najman et al., 2010) has juxtaposed four fault bounded litho-tectonic packages exposed along-strike with incredible lateral continuity. In particular, the high grade crystalline core, the Greater Himalayan Sequence (GHS), provides a view into processes that acted at mid-crustal levels during orogensis. Significant effort has focused on demonstrating coeval thrust- and normal-sense shearing on structures that bound the GHS (Burchfiel et al., 1992; Hodges et al., 1992; Godin, Grujic, Law, & Searle, 2006a; Yin, 2006), and development of an inverted metamorphic field gradient at the base of the GHS (Kohn, 2014). While thrust stacking has been invoked to account for a significant portion of shortening during the late Miocene in structurally lower units (DeCelles et al., 2001), many models treat the GHS as a large coherent deforming section (Beaumont et al., 2001). However, recent evidence has identified structural discontinuities within this high-grade lithotectonic unit (Larson, Ambrose, Webb, Cottle, & Shrestha, 2015).

One or more thrust-sense intra-GHS tectonometamorphic discontinuities have been located in 17 different transects in the Himalaya, spanning from just west of the Nepali-Indian border through Bhutan (see reviews in Larson et al., 2015 and Cottle, Larson, & Kellett, 2015). Early evidence from petrographic and kinematic observations led some researchers to argue that intra-GHS discontinuities are late-stage, post-peak-

metamorphic features (Vannay & Hodges, 1996). More recent studies have used coupled thermobarometry and chronology to demonstrate in-sequence behavior near the peak of metamorphism. For example, an in-sequence thrust was inferred that cuts the GHS in the Langtang region of central Nepal based on coincident cooling of structurally high rocks and heating of structurally lower rocks from 21-15 Ma (Kohn, Wieland, Parkinson, & Upreti, 2004). Once the structurally higher thrust ceased moving, active thrusting shifted structurally downwards, transferring former footwall rocks into the hanging wall of a newly activated thrust – the Main Central Thrust (MCT) – at the base of the GHS (Kohn et al., 2004). Along the Modi Khola river in the Annapurna region ~ 200 km west of Langtang there are two intra-GHS thrusts above the MCT (Corrie & Kohn, 2011). Here, monazite growth ages record cooling of the Main Central Thrust sheet from 20-16 Ma (Corrie & Kohn, 2011). While these examples and others support models in which the GHS was assembled through in-sequence thrust imbrication (Kohn et al., 2004; Kohn, 2008; Corrie & Kohn, 2011; Ambrose et al., 2015; Montomoli, Iaccarino, Carosi, Largone, & Visona, 2015; Larson et al., 2015; Cottle et al., 2015), they also indicate that the number, structural position, age, and duration of intra-GHS thrusts is highly variable. Corrie and Kohn (2011) argued that the presence of lateral ramps along strike or non-continual thrust planes could explain synchronous movement of thrusts at different structural levels. Intra-GHS thrusting also has implications for when and by what mechanism the high-grade package cools: Does intra-GHS thrusting continuously cool each sheet during thrust imbrication? Or does the entire process take place at depth where rocks remain hot until some later process exhumes them? More importantly, do different processes occur in two areas separated by tens or hundreds of km? Unforgiving

topography complicates tracing major structures along-strike, so more closely-spaced transects are required to fully assess variability in intra-GHS structures.

This study examines the thermal history of titanite-bearing upper GHS lithologies in the Annapurna region, Central Nepal. The incorporation of Zr into titanite is temperature sensitive (Hayde, Watson, & Work, 2008); therefore, in combination with relatively high U contents and potentially slow diffusion rates for Pb and Zr (Kohn & Corrie, 2011, Spencer et al., 2013; Stearns, Cottle, Hacker, & Kylander-Clark, 2016), titanite can provide a robust record of temperature-time (T-t) data for mid-crustal rocks. In this study, we use titanite T-t paths to infer protracted, high temperatures (~750-850 °C) from the late Oligocene to mid-Miocene, and make comparisons with intra-GHS thrusts identified elsewhere in Central Nepal. This comparison illustrates the large variability in position, duration, age, and related cooling history over tens of kilometers along strike.

CHAPTER TWO: GEOLOGIC SETTING
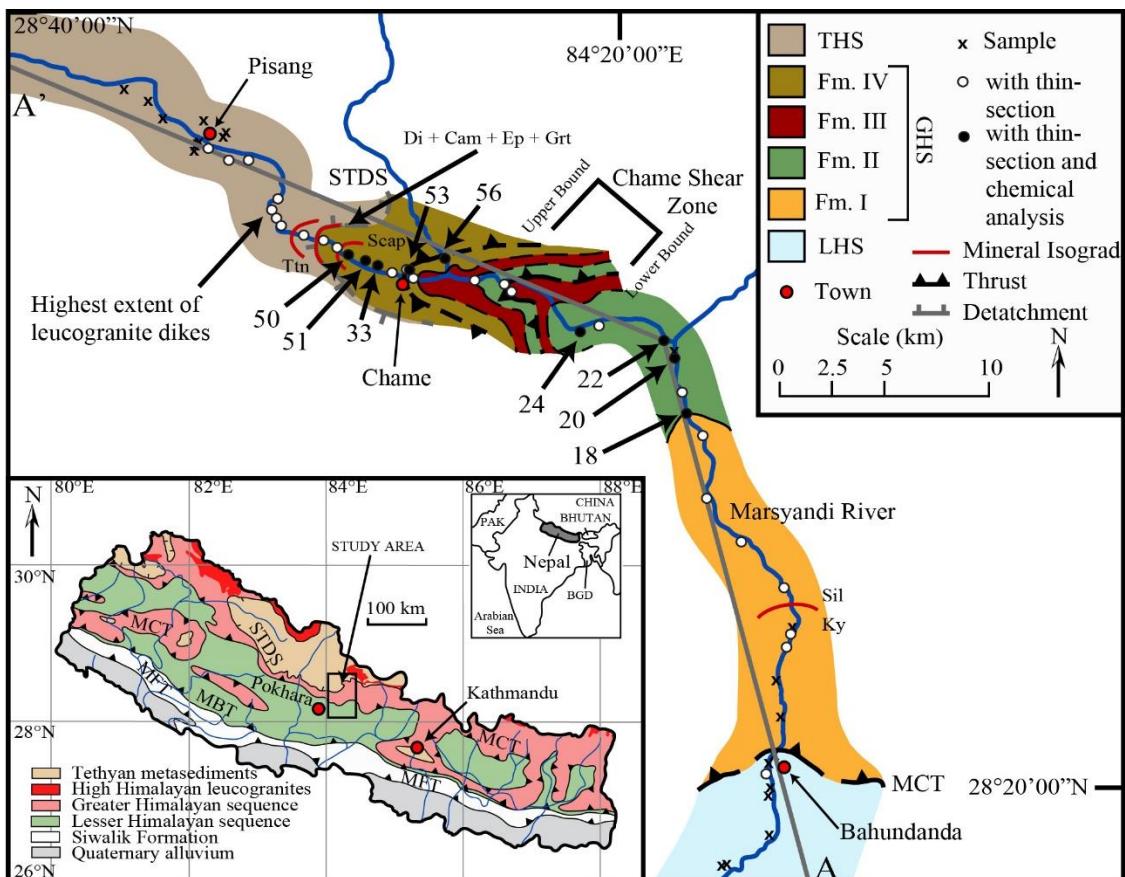
Figure 1. **Geologic map of the Marsyandi River Valley showing sample locations, major structures, and mineral isograds (inset modified from Corrie & Kohn, 2011). A-A' shows location of cross-section. See Table 1 for mineral abbreviations.**

From south to north, the Himalaya can be divided into four fault-bounded

packages: unmetamorphosed Tertiary synorogenic sedimentary rocks of the

SubHimalayan sequence, greenschist to mid-amphibolite facies metasedimentary and

meta-igneous rocks of the Lesser Himalayan Sequence (LHS), mid-amphibolite to lower

granulite facies metasedimentary and meta-igneous rocks of the Greater Himalayan

Sequence (GHS), and mid-amphibolite facies to unmetamorphosed sedimentary rocks of the Tethyan Himalayan Sequence (THS). For a more in depth review of Himalayan geology and metamorphism see recent reviews in Yin and Harrison (2000), Yin (2006), and Kohn (2014). The Marsyandi River valley in the Annapurna region of central Nepal (Figs. 1 and 2) exposes the upper LHS through a complete section of the GHS into unmetamorphosed THS sediments. The GHS in central Nepal is commonly divided into three lithotectonic units: Formation I, Formation II, and Formation III (LeFort, 1975; Colchen, Le Fort, Pêcher, 1986; Pêcher & LeFort, 1986). Formation I consists predominantly of metapelitic schist and paragneiss, with dispersed lenses of orthogneiss and rare calc-silicate. The mid to upper sections of Formation I commonly display migmatitic textures, inferred to reflect muscovite dehydration-melting, as well as melt pooling, and melt escape textures. Formation II consists of layered calc-silicate, metapsammite, marble, and minor schist, gneiss, and migmatite. Formation III is defined by migmatitic orthogneiss. Some exposures of the upper orthogneiss display ≤ 4 cm alkali-feldspar augen in a fine grained mylonitic matrix (Coleman, 1996). We define Formation IV of the GHS as diopside-amphibole calc-silicate, metapsammite, and marble overlying the upper orthogneiss. The THS directly overlies Formation IV and consists of a large section of banded biotite marble, often having a mottled texture with 1-12 mm wide pockets of Cal + Dol + Ms (see Table 1 for mineral abbreviations). Tourmaline bearing leucogranites pervasively cut the upper section of Formation I through Formation IV, and into the lower THS (Fig. 1). In the THS, leucogranite dikes are extensively deformed and adjacent marble is locally altered to form diopside.

The study area includes at least three major structures: from structurally lowest to highest these are the Main Central Thrust (MCT), Chame Shear Zone (CSZ), and the South Tibetan Detachment System (STDS). In the Marsyandi valley, the MCT occurs just above the ky-isograd and defines the LHS-GHS boundary immediately north of Bahundanda (Colchen et al., 1986; Catlos et al., 2001). Demarcated by abundant top-to-the-west ductile shear sense indicators, the CSZ identified near the town of Chame has previously been interpreted as the STDS dividing upper GHS units (Formation III and an overlying calc-silicate unit) from THS calc-silicates (Coleman, 1996, 1998; Coleman & Hodges, 1998; Godin, Gleeson, Searle, Ulrich, & Parrish, 2006b; Searle, 2010). However, as discussed below, we interpret the CSZ as either a ~2.5-3 km wide thrust-sense shear zone or multiple (at least two) localized thrusts. The lithologic repetition of Formations II and III (Figs. 1 and 2), first mapped by Coleman (1996), marks the lower bound of the CSZ. The upper bound is indicated by a change in the trajectory of titanite T-t paths (see discussion). Top-to-the-west shear sense indicators overprint older reverse sense indicators. The STDS is located ~1 km above the CSZ, and is marked by a structurally upward (west-ward) rapid transition over ~200 m from diopside bearing calc-silicates to biotite marble, roughly equivalent to a transition from sillimanite- to biotite-grade in meta-pelites (Ferry, 1976). At the same location Coleman (1996) identified a 200-300 m thick shear zone with S-C mylonitic fabric that indicates top-to-the-west-south-west, strike-parallel shearing.
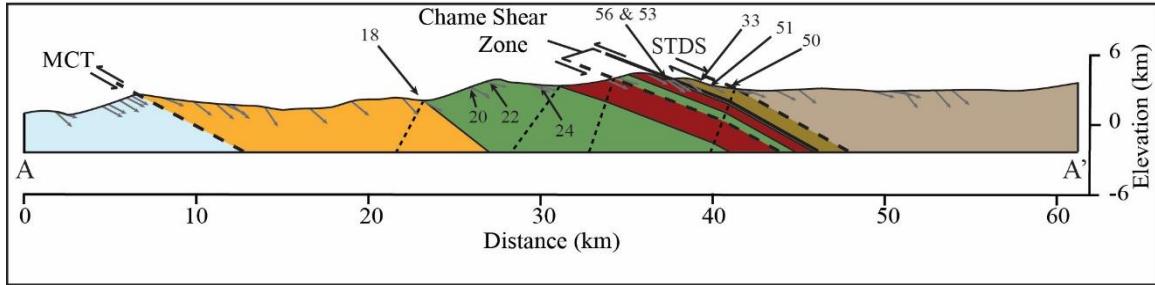
Figure 2. Geologic cross-section along the Marsyandi River showing lithologic divisions, major structures, apparent dips (gray arrows) of tectonic foliation measurements, and key sample locations. Cross-section is constructed using the kink-band (light dashed lines) method of Suppe (1983).

Metamorphic grade appears to increase continuously from biotite-grade in the LHS to sillimanite-grade in the migmatitic center of the GHS. Diopside-scapolite bearing calc-silicates and marbles in Formations II and IV are compatible with sillimanite-grade conditions. While thermobarometric assessments of the upper reaches of the Marsyandi valley are sparse (Catlos et al., 2001), our mineralogical observations are consistent with P-T conditions of other sections in Central Nepal. Generally peak metamorphic temperatures increase from 600-700 °C at the base of the GHS (i.e. the MCT) to ~ 800 °C within ~ 5 km above the MCT (Kohn, 2014). From the core of the GHS temperatures remain approximately constant to the STDS (Kohn, 2014). Carbonate solvus thermometry in the Marsyandi River valley demonstrates a decrease in temperature from 530 to 370 °C within ~ 2.5 km above the STDS (Schneider & Masch, 1993). Changes in pressure through the GHS are more variable in Central Nepal. In the nearby Modi Khola drainage, pressures increase from ~ 11 kbar to ~13 kbar at 0.5 to 3 km structural distance above the MCT (Corrie & Kohn, 2011), whereas further east in the Darondi and Langtang regions pressures gradually decrease from ~12 kbar at the MCT to ~ 8 kbar at ~ 10 km structural distance above the MCT (Kohn, Catlos, Ryerson, & Harrison, 2001; Kohn, 2008).

Ages systematically increase upwards across the GHS in the Marsyandi River section. Metamorphic monazite Th-Pb ages increase from < 10 Ma below the MCT to 32.2 ± 1.4 Ma in Formation III (Catlos et al., 2001). Monazite U-Pb ages of 18-35 Ma from migmatites and leucogranite dikes (Coleman, 1998) are broadly commensurate with the Th-Pb ages, but cannot be interpreted with confidence because they mix different monazite generations, possibly including Paleozoic detrital grains, and are affected by excess ^{206}Pb (Harrison, Catlos, & Montel, 2002; Kohn, Wieland, Parkinson, & Upreti, 2005). ^{40}Ar/^{39}Ar hornblende, biotite, and muscovite cooling ages also show an increase from 3-6 Ma in the upper LHS to ca. 15-16 Ma near Chame (Edwards, 1995; Coleman, 1996; Coleman & Hodges, 1998; Bollinger et al., 2004; Huntington & Hodges, 2006; Godin et al., 2006b). Problems with the ^{40}Ar/^{39}Ar system in hornblende and biotite have long been recognized in the Himalaya (e.g. Copeland et al., 1991; Herman et al., 2010; Martin, Copeland, & Benowitz, 2014), and are not considered in later interpretations. Low-temperature cooling ages give ranges of ca. 1-2 Ma (zircon fission track), ca. 0.5-2 Ma (apatite fission track), and ca. 0.25-1 Ma (apatite [U-Th]/He) for cooling from ~ 300 °C to ~85 °C (Blythe, Burbank, Carter, Schmidt, & Putkonen, 2007).

CHAPTER THREE: PETROGRAPHY AND MINERAL CHEMISTRY

Samples from the base of Formation II to the STDS were characterized using back-scattered electron imaging (BSE) and energy dispersive spectrometry analysis at Boise State University using a Hitachi S-3400N. We focused on nine titanite bearing calc-silicates collected from units II and IV (Fig. 1). Major element compositions (see appendix A) were collected with a Cameca SX-50 electron probe microanalyzer (EPMA) at Brigham Young University using a beam diameter of 1 µm at 15 kV and 10 nA, with the exception of feldspars where we used a diameter of 10 µm at 15 kV and 20 nA. Peak and background count times were 20 s and 10 s respectively. Standards used are tabulated in Table 11, appendix A.

The common metamorphic assemblage analyzed in granoblastic to gneissic calc-silicates is Di + Cam + Scap + Pl + Kfs + Ep ± Ttn ± Ap ± Zrn ± Tur (Table 1). Appendix B lists detailed petrographic and textural descriptions of each sample. Formation II and IV calc-silicates are extensively retrogressed and rarely preserve prograde metamorphic textures. The majority of EPMA analyses avoided obvious retrograde textures.

Some mineralogical textures reflect prograde reactions (described in the endmember K_2O-CaO-MgO-Al_2O_3-SiO_2-H_2O-CO_2 system following Ferry, 1976):

Zoisite zone: (a) Lenses of epidote growing near calcite and zoned plagioclase may indicate the hydration/decarbonation reaction $An + Cal + H_2O = Zo + CO_2$ (Fig. 3A). (b) Hornblende replacing optically continuous biotite (Fig. 3B) possibly marks the

decarbonation/dehydration reaction 5 Phl + 6 Cal + 24 Qtz = 3 Tr + 5 Kfs + 6 CO_3 + 2 H_2O. (c) Actinolite cores in hornblende (Fig. 3C) are consistent with a general increase in amphibole Al and Fe contents with increasing metamorphism.

Table 1   Modal Abundances[1,2]

Sample[3]	18B	20E2	22B	24A	56B	53A	33B	51A	50A
Qtz	10	12	10	10	15	0-40	7-10	10-25	10-40
Kfs	10	8	10		40	0-10	1	10	5
Pl	5	10	2	10	2	0-5	<1	5-10	<1-2
Scp	20	<1	15	15			2-4		5-30
Cal	8	5-15	20	20		5-10	50-70	5-55	10-55
Cam	5	10-30	<1	<1	35	5-95	5-10	1-15	<1
Di	35		35	40		0-40	0-20	20	
Bt		20-40	<1		5	0-25	8		20-60
Ep	5	<1	5	2	<1	<1	0-2		<1
Ttn	2	5	3	3	3	5	<1	<1	<1
Aln	<1	<1	<1	<1	<1	<1	<1		<1
Ap	<1	<1		<1		<1	<1		<1
Zrn	<1	<1	<1	<1	<1	<1	<1	<1	<1
Tur						5	<1		
Grt									<1

[1] Abbreviations after Kretz (1983): Quartz (Qtz), alkali-feldspar (Kfs), plagioclase (Pl), scapolite (Scp), calcite (Cal), Ca-amphibole (Cam), actinolite (Act), hornblende (Hbl), diopside (Di), biotite (Bt), epidote (Ep), titanite (Ttn), allanite (Aln), apatite (Ap), zircon (Zrn), tourmaline (Tur), garnet (Grt), anorthite (An), zoisite (Zo), phlogopite (Phl), tremolite (Tr), rutile (Rt). We use Me to refer to the meionite endmember of scapolite.
[2] Abundances estimated visually.
[3] Sample names begin with KN14-.

Diopside zone: Embayments and islands of epidote in scapolite (Fig. 3D) suggest the reaction Zo + CO_2 = Me + H_2O. At 10 kbar, the zoisite-meionite reaction occurs at $X_{CO2} < 0.3$ and ~ 800-975 °C in the CaO-Al_2O_3-SiO_2-H_2O-CO_2 system (Moecher & Essene, 1990). Similarly, garnet and/or wollasonite would become stable at $X_{CO2} < 0.2$ at temperatures > 800 °C, providing a minimum CO_2 composition during prograde and peak
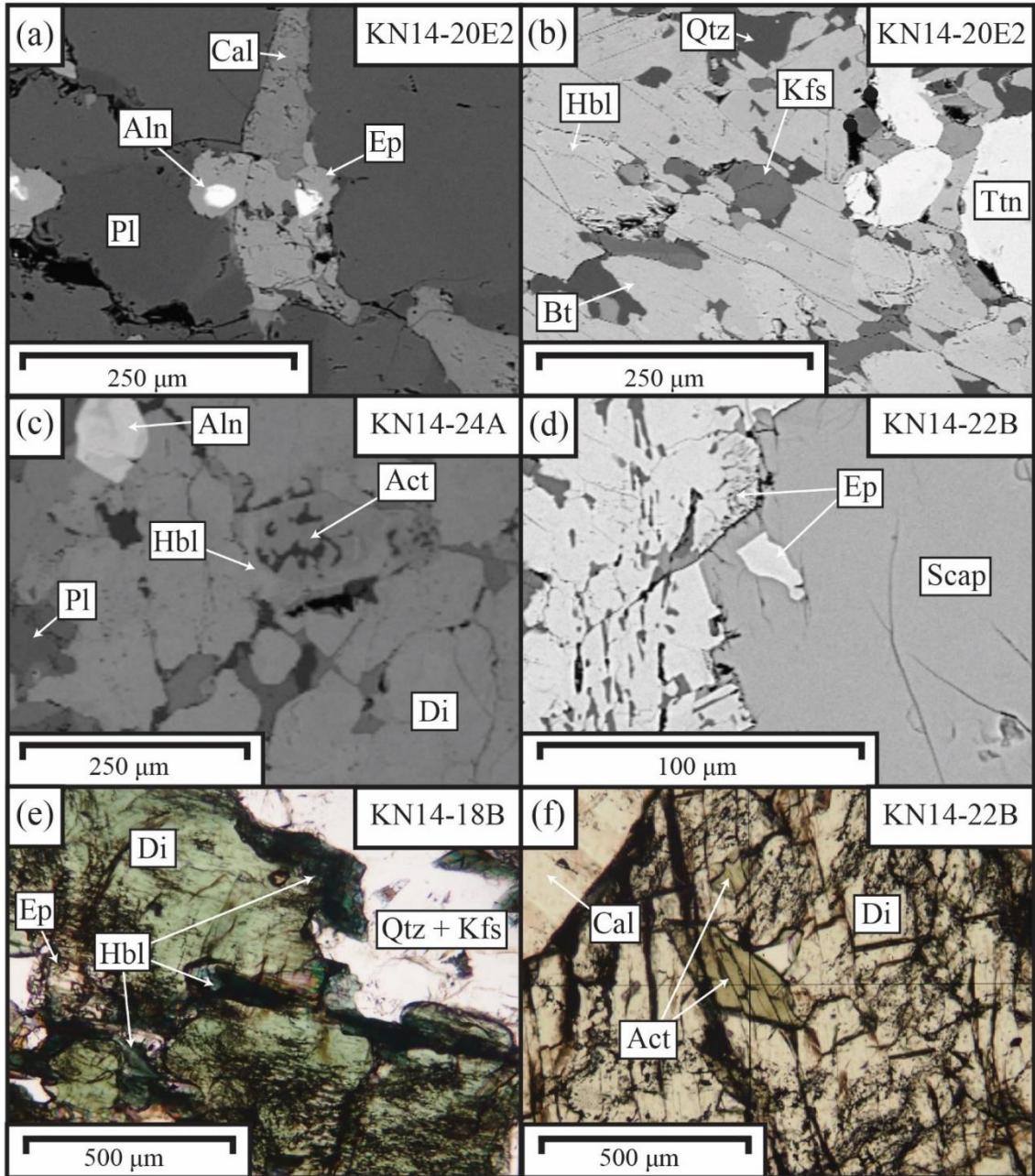
Figure 3. **Prograde reaction textures: (a) epidote replacing calcite and zoned plagioclase, (b) optically continuous biotite replaced by hornblende, (c) hornblende with an actinolite core, (d) islands and embayments of epidote against scapolite, (e) optically continuous hornblende replaced by diopside, (f) actinolite inclusion in diopside.**

metamorphism (Moecher & Essene, 1990). Diopside replacing hornblende (Fig. 3E) and

actinolite inclusions in diopside (Fig. 3F) suggest the reaction $Tr + Cal + Qtz = Di + H_2O + CO_2$ during late prograde metamorphism.

Calc-silicates are generally regarded as resistive to melting (Sawyer, 2008); however, partial melting may have been initiated by high peak temperatures (> 750 °C). Alkali feldspar replacing plagioclase (Fig. 4A) could represent biotite dehydration melting. Experiments by Gardien, Thompson, Grujic, and Ulmer (1995) at 10 kbar produced 3 vol % melt from the reaction Bt + Pl + Qtz = Kfs + melt + Rt at 750 and 800 °C, while orthopyroxene and garnet began to form at $\geq$ 825 °C and $\geq$ 9 vol % melt. While the Bt + Pl + Qtz system is a good approximation for low degrees of partial melting, orthopyroxene is not observed in high-grade calc-silicates worldwide. Calc-silicates may produce only small degrees of melt, or bulk compositional differences preclude direct comparison with experiments. However, small degrees of partial melting at 750-800 °C are consistent with our peak Zr-in-titanite temperatures. Biotite-quartz symplectites, feldspar-quartz symplectites, and graphophyre, such as we observe in our rocks (Fig. 4B-D), are common textures in anatectic rocks and may represent crystallization of partial melt during cooling (Sawyer, 2008).

Retrograde metamorphic textures are common but are markedly different above the CSZ than below it:

Diopside retrogression: Texturally-late actinolite occurs only in samples above the CSZ (Fig.5b) where actinolite and calcite rim and replace diopside, indicating the reaction Di + H_2O + CO_2 = Cal + Tr + Qtz. The diopside breakdown reaction requires an H_2O-rich fluid influx (see later section for interpretation). Diopside compositions above the CSZ are more Mg rich, and show zoning in Fe and Mg indicating retrograde re-equilibration (Fig. 5b).
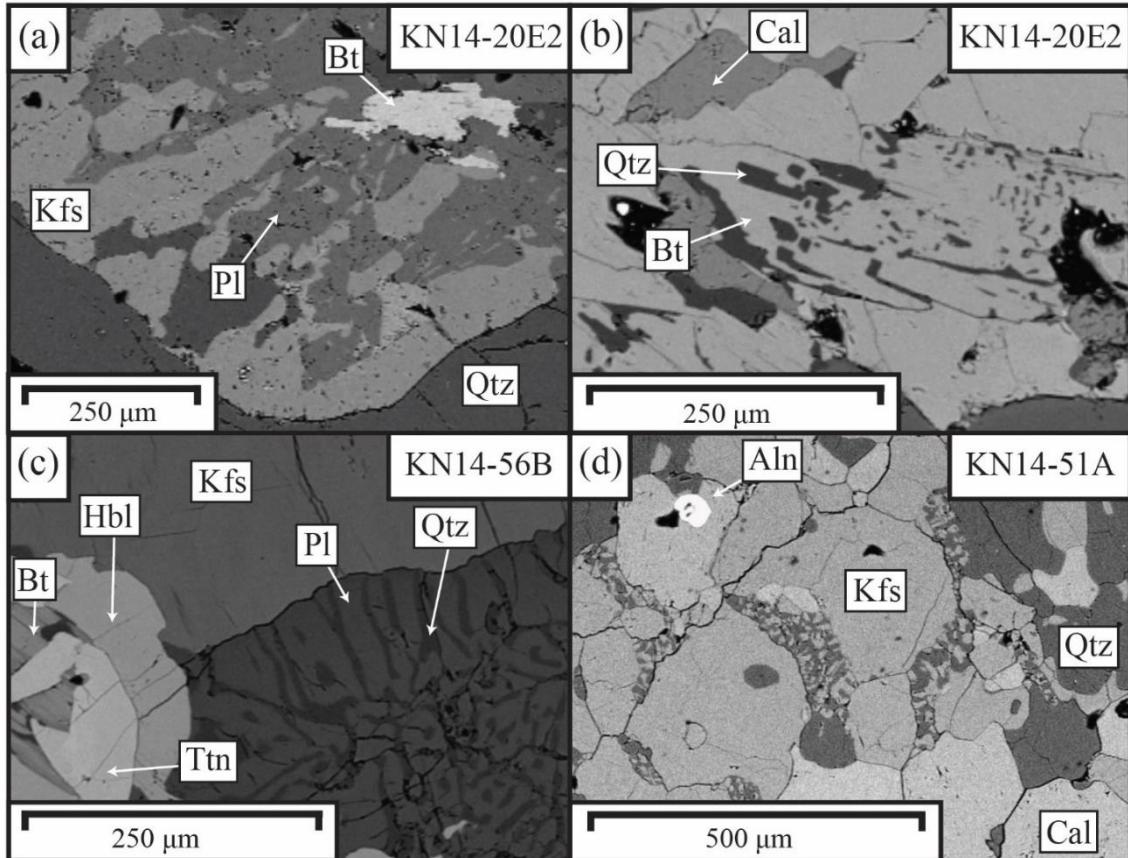
Figure 4. **Possible melting and melt crystallization textures: (a) Alkali feldspar growing into plagioclase, (b) biotite-quartz symplectite, (c) plagioclase-quartz symplectite, and (d) granophyric texture (fine-grained mottled segregations).**

Scapolite retrogression: Scapolite is commonly rimmed by retrograde plagioclase (Fig. 5a) indicating the reaction Me = 3 An + Cal and is found throughout Formations II and IV. The scapolite to plagioclase breakdown reaction occurs at ~800 °C at 10 kbar in the CaO-Al_2O_3-SiO_2-CO_2-H_2O system (Moecher & Essene, 1990). The anorthite content of plagioclase decreases rapidly from the grain boundary and transitions into plagioclase-quartz symplectites in some samples. In KN14-24A, epidote fills grain boundaries adjacent to scapolite and suggests the reaction Zo + CO_2 = Me + H_2O. Scapolite breakdown into plagioclase, rather than epidote, in most samples suggests either no free fluid was present or that little H_2O infiltrated during retrograde metamorphism (Moecher

& Essene, 1990). This reaction is not present in most rocks above the CSZ, where H_2O-bearing fluids helped to drive diopside retrogression to amphibole.
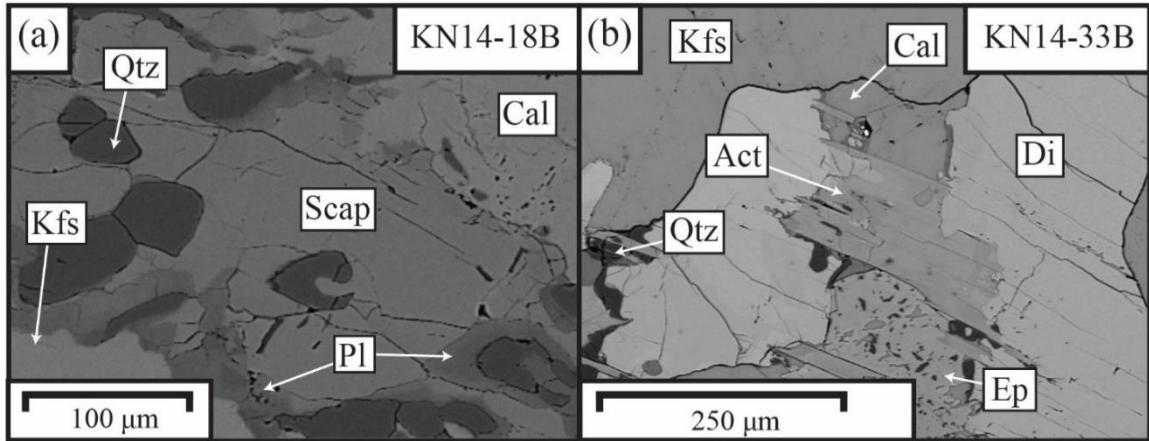
Figure 5.   **Retrograde reaction textures: (a) plagioclase replacing scapolite, and (b) diopside breakdown to form actinolite.**

CHAPTER FOUR: THERMOBAROMETRY

Several thermobarometric methods were applied to mineral compositions, and results generally reflect different aspects of prograde and retrograde metamorphism.

Hbl-Pl Thermometry and TZARS Barometry

Major element compositions from samples KN14-18B, -20E2, -56B, -50A were selected for Hbl-Pl cation exchange thermometry (2 equilibria; Holland & Blundy, 1994) and TZARS barometry (1 equilibrium; Kapp, Manning, & Tropper, 2009). Hornblende and plagioclase analyses were restricted to the compositional criteria of the calibration. Edenite-tremolite thermometry requires hornblende compositions of $Na^A > 0.02$, Al^{vi} <1.8, Si = 6.0-7.7, and plagioclase with $X_{An} < 0.90$. Edenite-richterite thermometry requires hornblende compositions with $X_{Na}^{M4} > 0.03$, $Al^{vi} < 1.8$, Si = 6.0-7.7, and plagioclase compositions of $0.10 < X_{An} < 0.90$.

TZARS barometry employs the pressure-sensitive net-transfer reaction 2 Zo + Rt + Qz = 3 An + Ttn + H_2O. Pressures were calculated using the average pressure function in Thermocalc (Powell & Holland, 1994; Powell & Holland, 1998) following the methods of Kapp et al. (2009). Activities of zoisite were calculated using the program AX of Holland (2002). Anorthite activities were averaged between the output of AX and the model of Fuhrman & Lindsley (1988). Following Kapp et al. (2009), an ideal mixing model was used for a_{Ttn}, while a_{Rt}, a_{H20}, and a_{Qtz} were assumed to be 0.75 ± 0.25, 0.95 ± 0.05 and unity respectively. High Mg compositions of amphibole and biotite in our samples prevented direct calculation of a_{Rt} using the method of Chambers and Kohn

(2012). Titanite and zoisite activities were based on averages of all analyses. Error in the

TZARS pressure assumes a ± 40 °C calibration error in the Hbl-Pl temperature (Holland

& Blundy, 1994). Calculated P-T conditions are reported to the nearest 5 °C and 0.1 kbar.

Table 2   Hbl-Pl thermometry[1,2] and TZARS Barometry

Sample (KN14-)	P (kbar)	2σ	T[3] (°C)	T[4] (°C)	T[Ave] (°C)	2σ
18B	11.9	2.8	670	685	680	25
20E2 high An	10	2.5	730	730	730	0
20E2 low An	10.5	2.6	705	700	700	5
Wtd Ave	10.2				725	
56B high An	11.1	2.7	690	725	710	25
56B low An	11.5	2.8	670	695	685	20
Wtd Ave	11.3				695	
50A high An	10.6	2.5	675	710	690	50
50A low An	10.2	2.6	655	680	670	40
Wtd Ave	10.4				680	

[1]Temperatures rounded to the nearest 5 °C.
[2]Calibration error is ± 40 °C.
[3]Edenite-tremolite
[4]Edenite-richterite

Average pressure and temperature from TZARS barometry and Hbl-Pl

thermometry are 10.25-12.0 kbar and 675-725 °C respectively (Table 2). The two

different Hbl-Pl thermometers are generally consistent to ± 25 °C in individual samples,

suggesting near-equilibrium for hornblende and plagioclase compositions. Observed

variation in plagioclase compositions (~ 10 % An) results in temperature and pressure

variations of 20-30 °C and 0.4-0.5 kbar. P-T estimates from different rocks are typically

within 2σ error regardless of structural position (Fig. 6).

Thermocalc Average P-T

Major element compositions of minerals from samples KN14-22B, -24A, -53A, -33B, -50A were used to calculate average P-T conditions in Thermocalc (Table 3). Titanite, rutile, H_2O, and plagioclase activities were treated the same as for TZARS barometry. For minerals with multiple analyses, activities calculated by AX were averaged. Amphiboles and garnet often show core-rim zoning; therefore, only rim compositions were used. Mineral endmembers with outlier behavior were removed during Average P-T calculations using diagnostics in Powell and Holland (1994).

Table 3   Thermobarometry Continued[1]

Thermocalc Average P-T							Gt-Bt	Scap-Pl
Sample (KN14-)	P (kbar)	2σ	T (°C)	2σ	Corr.	Fit	T (°C)	T (°C)
18B								735
20E2 high An								725
20E2 low An								630
Wtd Ave								680
22B high An	13.4	2.6	795	65	0.97	1.2		755
22B low An	12	3.6	705	100	0.98	0.69		660
Wtd Ave	12.9		770					710
24A	9.4	2.4	715	70	0.95	1.24		625
53A high An	9.3	3	660	95	0.95	0.79		
53A low An	12.3	3.6	675	95	0.9	0.87		
Wtd Ave	10.5		670					
33B high An	13.3	3	790	80	0.97	1.23		775
33B low An	13.1	4.6	730	130	0.98	1.12		655
Wtd Ave	13.2		770					715
50A high An	10.2	1.8	685	60	0.92	0.76	670	795
50A low An	11.2	1.8	680	60	0.88	0.83		710
Wtd Ave	10.7		685					750
[1]Temperatures rounded to the nearest 5 °C.								

Pressures and temperatures range from 9.5-13.5 kbar and 660 - 795 °C respectively, and do not correlate with structural position (Fig. 6). Uncertainties are large in both temperature (~ 50 °C, 2σ) and pressure (~ 2 kbar).

Other methods

The reaction Me = 3 An + Cal observed in most scapolite-bearing samples has an extremely steep Clapeyron slope and may be thermometrically useful. Temperatures were calculated using the thermodynamic data presented by Baker and Newton (1995) and TZARS pressures, and range from 625 to 750 °C (Table 3). However, variation of plagioclase compositions within each sample results in temperature variations of ~ ± 100 °C. Anorthite content commonly decreases with distance from the contact with scapolite; the highest X_{An} plagioclase adjacent to scapolite produces a temperature of 629 °C, 141 °C lower than the temperature indicated by Thermocalc. The discrepancy between scapolite-plagioclase thermometry and other methods may reflect uncertainties in thermodynamic properties, uncertainties in activity models, or the temperature at which the meionite breakdown reaction initiated.
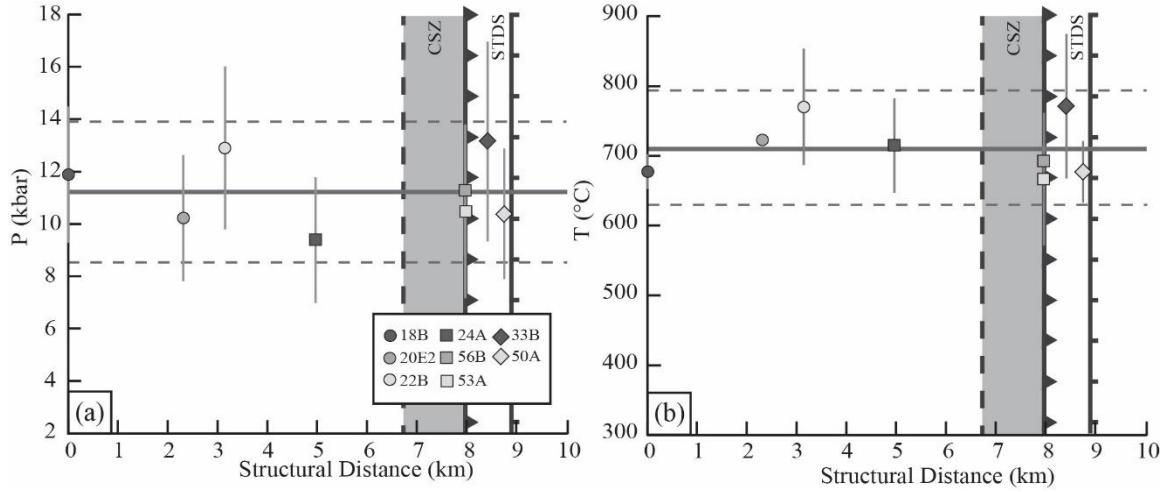
Figure 6. **(a) Pressure and (b) temperature plotted against structural level above the Formation I-II boundary. Solid lines show average pressure and temperature. Dashed lines represent 2σ bounds.**

Garnet-biotite thermometry in sample KN14-50A, using the Ferry and Spear (1978) calibration with the Berman (1990) garnet activity model produces a temperature of 670 °C at 10.4 kbar (Table 3), well within the range of both Hbl-Pl and Thermocalc results.

CHAPTER FIVE: TITANITE PETROCHRONOLOGY

Back-scattered electron images were collected for titanite grains using a Hitachi S-3400-II scanning electron microscope, housed in the Boise State Center for Materials Characterization, Department of Materials Science and Engineering, Boise State University, to discriminate specific growth zones that could be separately targeted for chemical and chronologic analysis. ^{27}Al (3 ms) , ^{29}Si (5 ms), ^{43}Ca (5 ms), ^{49}Ti (10 ms), ^{90}Zr (5 ms), ^{204}Pb + ^{204}Hg (10 ms), ^{206}Pb (50 ms), ^{207}Pb (50 ms), ^{232}Th (5 ms), ^{235}U (20 ms), and ^{238}U (20 ms) were collected using a Thermoelectron X-Series II quadrupole ICPMS and New Wave Research UP-213 Nd:Yag UV (213 nm) laser ablation system at Boise State University. A relatively small element list was chosen to improve counting statistics for Pb and U isotopes. Analyses used laser spot sizes of 25 and 40 µm with 319 sweeps, a repetition rate of 10 Hz, and power density within the range of 4-6 J/cm^2. Five standards each for both 25 and 40 µm spot sizes were collected before and after each sample using BLR-1 (Aleinikoff et al., 2007; Mazdab, 2009) or MKED1 titanite standards (Spandler et al., 2016).

Data were processed using Iolite v 2.5 (Paton, Hellstrom, Paul, Woodhead, & Hergt, 2011). Si and Ca were used as the internal standard on 25 and 40 µm spots respectively. U-Pb ages were calculated using the inverse (2-pt) isochron method in Isoplot v 4.0 (Ludwig, 2012) assuming an initial ^{207}Pb/^{206}Pb composition measured on U poor minerals: clinopyroxene, amphibole, biotite, tourmaline, and alkali feldspar (Kohn & Corrie, 2011). 2σ errors were commonly ≤ ± 5 Ma, but high common Pb in some

samples results in large errors of $\geq \pm 10$ Ma. Zr-in-titanite temperatures were calculated using the formulation of Thomas et al. (2010). An a_{Rt} of 0.85 ± 0.10 and an error of ± 1.0 kbar (2σ) in pressure were assumed, resulting in uncertainties of ~8 and ~10 °C (2σ) respectively. Measurement precision on Zr concentrations resulted in 2σ errors of ± 1-3 °C. Analyses that intersected inclusions or quickly ablated into an underlying mineral grain were not considered.

Titanite T-t data were assessed for sector zoning. The preferential incorporation of trace and minor elements to crystal faces faces, indicative of sector zoning, is common in titanite (e.g. Paterson & Stephens, 1991), and may bias calculated temperatures. Hayden et al. (2008) observed sector zoning in Zr and argued that lower Zr concentration sectors are a better approximation of equilibrium conditions. Thus, their calibration is based on low-Zr sectors (when present). The maximum enrichment of Zr in sector zones increases temperatures by ~ 50 °C at 600 °C and ~ 70 °C at 800 °C (Hayden et al., 2008). Zr zoning cannot be directly imaged in BSE, but Zr likely follows sector zoning in other elements. Most samples display weak to no zoning in BSE, and age correlates well with Zr content (e.g. Fig. 7A). Nonetheless, three types of sector zoning are identifiable in our samples in the form of systematically higher Zr and U (Fig. 7B-D), although Al content varies. Sample KN14-51A displays the most noticeable effects of sector zoning with a parallel T-t trend elevated by ~ 40 °C, ~ 10-30 °C less than the maximum increase in apparent temperature measured by Hayden et al. (2008). Therefore, analyses from sharply defined polygonal zones imaged in BSE with increased U and Zr are not considered in interpretations. Preservation of sector zoning argues for minimal re-equilibration of Zr-in-titanite temperatures (see discussion).

Zr-in-Titanite temperatures are fairly sensitive to pressure, with an increase of 10 °C/kbar (Hayden et al., 2008; Thomas et al., 2010). Temperatures were adjusted for sample position across the section. If pressures represent conditions along an intact section, then pressure should increase structurally downwards along a lithostatic gradient. However, large uncertainties in our pressures prevent observing a lithostatic gradient over a thickness of ~ 9 km. For temperature calculations, we use a pressure of 10.4 kbar calculated for KN14-50A, constrained by both TZARS barometry and Thermocalc Average PT, and calculate nominal pressures downward for each sample along a lithostatic gradient (Fig. 7). Pressures are assumed constant with time; however, large changes in pressure would be required to significantly affect calculated rates of cooling or heating. For example, adjusting the T-t path of sample KN14-18B for increasing pressure from ~8 kbar at ca. 40 Ma to ~12 kbar at ca. 20 Ma increases heating rates from ~1 to ~ 3 °C/Ma.
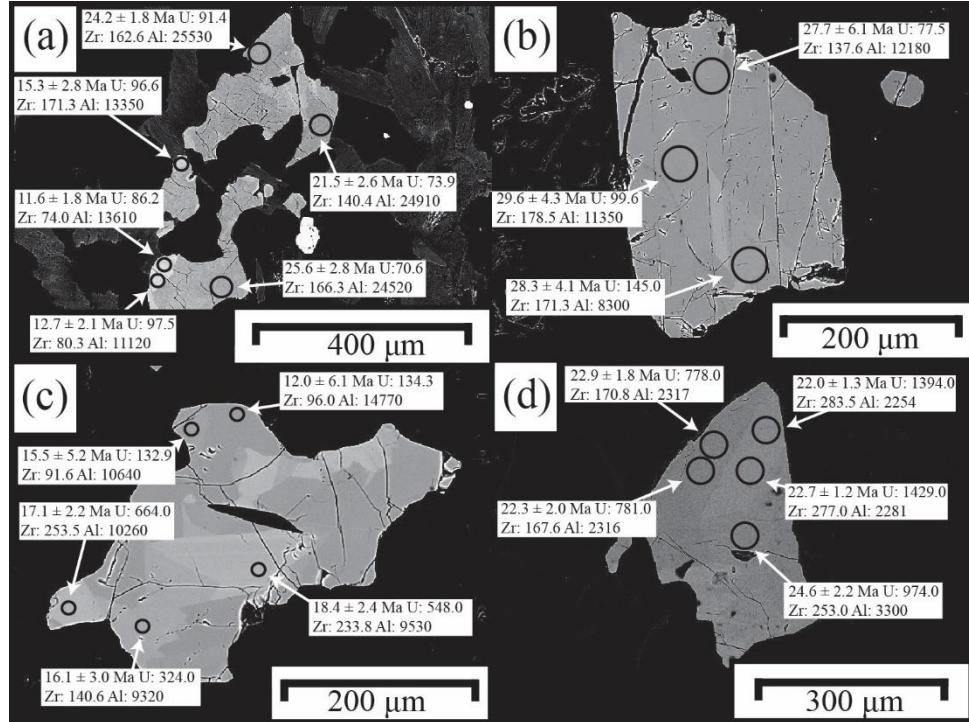
Figure 7. **BSE images of titanite showing age, [U] (ppm), [Zr] (ppm), and [Al] (ppm): (a) A single grain from sample KN14-50A showing decreasing [Zr] with age, (b-d) show possible sector zones with increasing [U] and [Zr], but variable [Al]. Ppm notation is on a weight basis.**

One key question we wished to address was whether petrochronologic data revealed any structural discontinuities within the section. Discontinuities are often identified at a specific time through thermobarometrically-defined inversions, such as the prominent inverted metamorphism observed proximal to the MCT (Kohn, 2014). Large barometric uncertainties in our samples prevent direct identification of pressure inversions; however, we can potentially identify thermal inversions, subject to some assumptions. We chose the Zr-in-titanite thermometer for this comparison: Zr appears unaffected by diffusive re-equilibration (see discussion), the thermometer has a high precision (a few degrees), and concurrent U-Pb data from the same analyses allows us to compare temperatures for specific times. We circumvent the issue of pressure-dependence for the thermometer by first hypothesizing a lithostatic pressure gradient

through the section at a time of interest, i.e. we first assume that no structural

discontinuity was present. We then correct temperatures for structural position and make

a *post hoc* comparison of temperature-time paths vs. structural position. If temperatures

decrease upwards for all times, the temperature distribution is consistent with a

structurally intact section. However, if temperatures increase upwards through part of the

section, we infer a thrust-sense shear zone either within or below the zone exhibiting the

inverted temperatures. Movement of the shear zone must have occurred either during or

after the time the temperature inversion is recorded. We calculated pressures structurally

downward relative to sample KN14-50A, whose pressure is best constrained via both

TZARS barometry and Thermocalc Average PT at ~10.4 kbar.
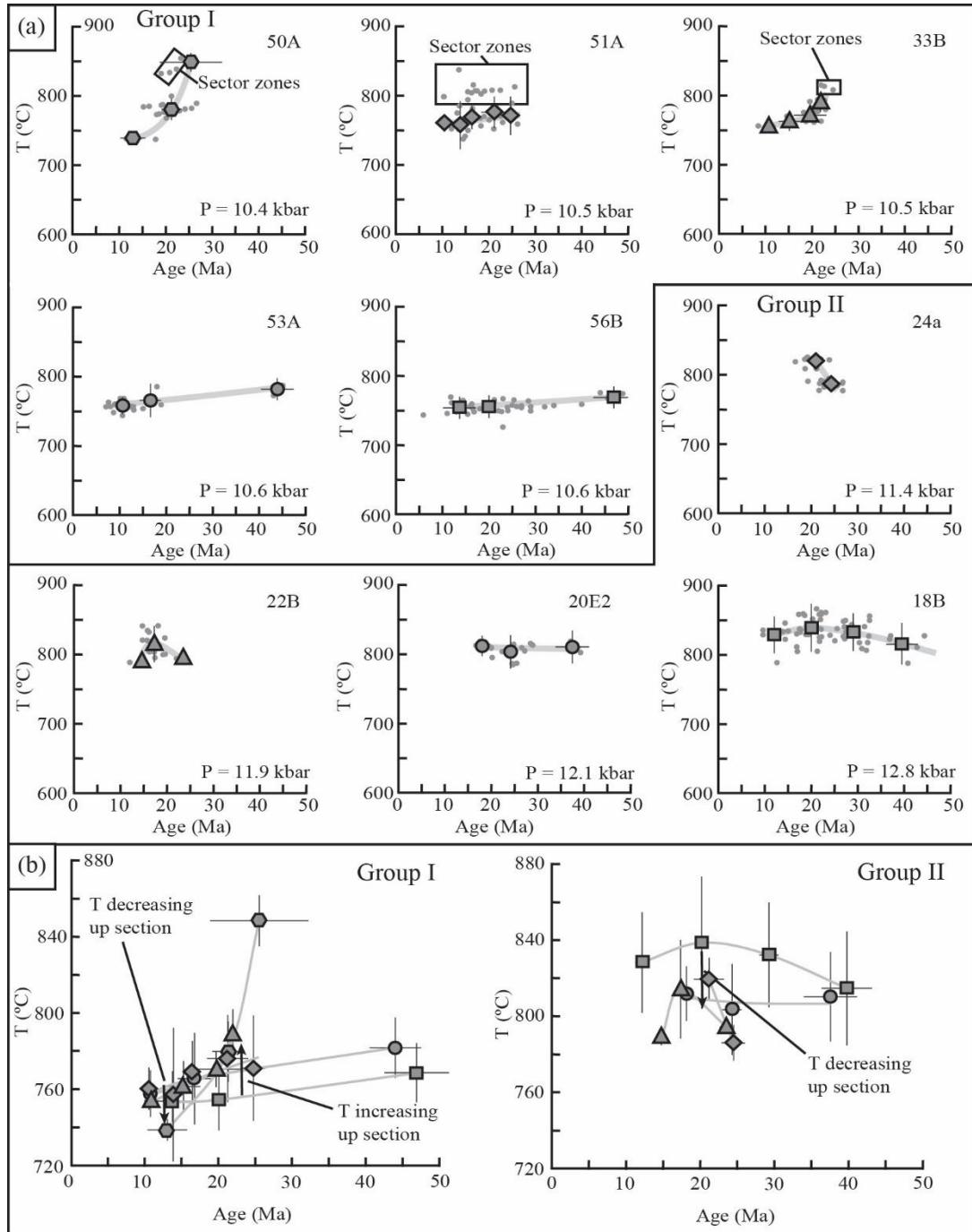
Figure 8. **(a) Titanite T-t data organized in decreasing structural level. Age groupings, processed together in Isoplot, are plotted with corresponding average temperature and 2σ. Light gray lines illustrate T-t paths. (b) Compiled T-t paths for each group. Temperatures decrease structurally up section at all times in Group II, while temperatures transition from increasing to decreasing structurally upward after ca. 15 Ma in Group I.**

Overall, our sample set can be divided into two groups based on T-t paths, mineralogy, and structural position (Fig. 8a). Group I rocks (KN14-50A, -51A, -33B, -53A, and -56B) were collected above the repetition of Formation III orthogneiss and contain significant retrograde alteration. Group I rocks show peak temperatures of ~ 750-850 °C, with a flat or decreasing trend towards 10 Ma (Fig. 8a). Cooling rates range from 1-10 °C/Ma. Between ca. 25-15 Ma temperatures increase structurally upwards through Group I (Fig 8b). By ca. 10 Ma Group I T-t paths converge at 750-760 °C and show no thermal inversion.

Group II rocks (KN14-24A, -22B, -20E2, and -18B) lie below Formation III and show decreasing temperatures structurally upward, as expected for a normal geotherm, but the reverse of Group I. T-t paths for Group II rocks show an increase in temperature of 20-30 °C between ca. 27 Ma and ca. 15-20 Ma, reaching peak temperatures of 810-840 °C. Group II heating rates range from 1-10 °C/Ma. Temperatures of ~830 °C persisted to ca. 9 Ma in Group II and demonstrate higher temperatures and younger ages than those reported by Kohn and Corrie (2011) in the Modi Khola valley ~ 55 km to the west.

CHAPTER SIX: DISCUSSION

Diffusion of Pb and Zr

Previous studies have documented retention of radiogenic Pb at temperatures ≥ 775 °C (Kohn & Corrie, 2011; Spencer et al., 2013; Stearns et al., 2016), and Zr-in-titanite temperatures may also remain unaffected. Experimental data (Cherniak, 2006) imply diffusion distances of ~ 80 µm at 750 °C and ~ 300 µm at 830 °C for 10 Myr. The preservation of high Zr in sector zones as small as 30 µm over 15 Myr at temperatures of ~760 °C demonstrates that diffusion of Zr in titanite is slower than experimental data suggest. Diffusion of Zr may be significant at temperatures of ≥ 800 °C or over timescales longer than 15 Myr. Nonetheless, our data require that Zr must diffuse over an order of magnitude slower than implied from experimental data.

Evolution of the Chame Shear Zone

Protracted thrusting can explain the titanite T-t data, including: the inverted temperature gradient in Group I, and simultaneous heating of structurally-lower rocks (Group II) during cooling of structurally higher rocks (Group I). We place the upper limit of the CSZ at the transition between shallow (KN14-56B and -53A) and steeper (KN14-33B and -50A) cooling T-t paths of Group I, just above Formation III. The occurrence of retrograde actinolite, which is restricted to higher level rocks (KN14-53A, -33B, and -50A), also occurs near this position. If thrusting occurred along the CSZ, fluids sourced from the foot wall could have driven diopside breakdown and hydration during cooling in the hanging wall. The location of the CSZ also occurs close to a repetition of Formation

II calc-silicates and Formation III orthogneiss (Coleman, 1996; Fig. 1). Repetition of

Formation III orthogneiss requires either a ~1.3 km thick zone of imbrication or localized

strain on two discrete thrusts (Fig. 9). The lower limit of the CSZ is at the base of the

calc-silicate between the repetitions of Formation III (Fig. 9), although the intermediate

calc-silicate may be related to Formation IV rather than Formation II. We acknowledge

that the upper and lower orthogneiss may be distinct. The upper orthogneiss contains

abundant feldspar augen in some locations, whereas none have been identified in the

lower orthogneiss. Also, shearing on the structurally-overlying STDS may have

facilitated fluid flow during retrograde metamorphism, rather than thrust sense shear on

the CSZ. While we recognize these possibilities, the combination of lithologic repetition,

retrograde fluid flux above the CSZ, and titanite T-t paths is better explained through

thrust-sense shearing on the CSZ. In addition, structurally-high, protracted thrusting to

ca. 15 Ma provides a mechanism to explain late cooling of the GHS.

In our model, thrusting between Group I and Group II rocks occurred from ≥ 25

Ma to ca. 15 Ma (Fig. 9). At depth the thrust zone ramps upward through Formation III,

repeating the orthogneiss and calc-silicate. Thrusting also juxtaposes locally hotter rocks

on top of colder rocks within the base of Group I. Group II rocks represent a coherent

unit where temperatures increase with depth. Increasing temperature from ≥ 25 Ma to ca.

15 Ma in Group II rocks is a result of discrete shear within the overlying CSZ. Cooling

and heating rates were ≤ 10 °C/Ma. Thrusting must have ceased by ca. 15 Ma, when

titanite T-t paths in Group I begin to converge. Between ca. 15 Ma and ca. 10 Ma,

temperatures generally increase downwards through the entire section. After ca. 10 Ma,

Formation II, III, and IV rocks cooled coherently post-thrusting, perhaps due to structural

uplift and erosion as these rocks were passively translated over younger, structurally-lower, thrust faults. The end of thrusting at ca. 15 Ma may have shut off fluid transfer across the CSZ, marking the end of H_2O driven the breakdown of scapolite to epidote and diopside to actinolite, and initiating the fluid absent breakdown of scapolite to plagioclase.
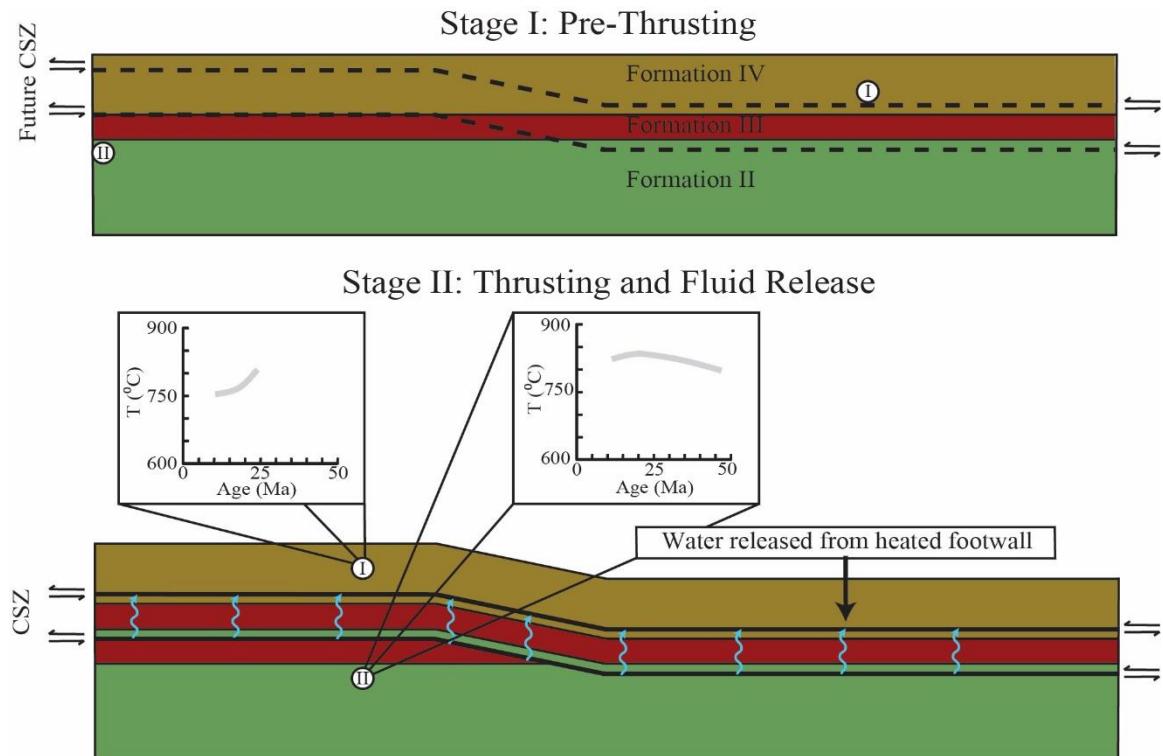
Figure 9. **Conceptual structural evolution of the CSZ. White circles represent particle locations of Group I and II rocks with representative T-t paths. The CSZ ramps upward through Formation III (red), sandwiching a layer of calc-silicate between orthogneiss. While the CSZ was active, fluids sourced from the dehydrating footwall fluxed the cooling hanging wall, initiating diopside breakdown into actinolite.**

Temperatures of 750-830 °C persisted until ca. 10 Ma. Hbl-Pl and Thermocalc temperatures are as much as 140 °C lower than Zr-in-Titanite temperatures at ca. 10 Ma and reflect the closure of net-transfer reactions at T~700°C. Thus, retrograde resetting of peak temperatures occurred between ca. 10 Ma and Ar closure in muscovite at 425 °C

and ca. 3.8 Ma (Huntington & Hodges, 2006). Minor variability in P-T conditions from sample to sample may reflect variable retrogression. A possible explanation for the lack of a gradient in pressure across the section is that if rocks were exhuming as they cooled, similar pressures might be recorded at different structural levels, but at different times. That is, the 11 kbar – 700 °C P-T condition was reached earlier at higher structural levels (Group 1) than deeper in the section (Group II). Large pressure uncertainties also compromise resolution of small pressure changes across the section.

While there may be structurally lower intra-GHS thrusts in the Marsyandi transect, movement along the MCT dated at ca. 16 to ca. 9 Ma at Langtang is consistent with the MCT as the next active thrust. Thrusts between the CSZ and MCT would require out-of-sequence thrusting (intervening thrusts are older than the structurally higher CSZ), coincident movement on multiple thrusts (synchronous with the CSZ, MCT, or both), or younger movement along the MCT.

Normal sense shear indicators in the region (Coleman, 1996) suggest that between 10 and 3.8 Ma the CSZ was reactivated with ductile normal sense top-to-the-west-northwest shear. Regardless of whether thrusting occurred on the CSZ, normal shear before ca. 10 Ma would result in cooling of Group II rocks, for which we find no evidence. Depending on the timing of STDS movement, these overprinting fabrics could represent the downward partitioning of ongoing extensional strain. Alternatively, several strands of the STDS might have formed post thrusting. Strongly deformed leucogranite dikes crossing the uppermost trace of the STDS suggest that it was active during anatexis and melt escape in the underlying GHS. Significant displacement on the STDS is required to explain the steep decline in temperature between the THS and GHS observed

in the Marsyandi and elsewhere, but our data do not directly constrain the timing or conditions of STDS movement.

Along-strike variability in the Himalaya

Our interpretation of structurally high intra-GHS thrusting is consistent with models that employ thrust imbrication as the primary mode of shortening in the Himalaya, even within high-grade metamorphic rocks (Kohn et al., 2008). Interestingly, of the 14 previously identified intra-GHS thrusts with ages constraints, 11 were in part active over the same ca. 25 – ca. 15 Ma time interval as the CSZ (Larson et al., 2015). More detailed comparison with other intra-GHS thrusts illustrates profound along-strike changes in structural position, metamorphic histories, and durations.

The position and duration of the CSZ is strikingly different when compared to intra-GHS thrusts in the nearby (~55 km to the west) Modi Khola valley. There, two thrusts have been identified within Formation I (Martin, Ganguly, & DeCelles, 2010; Martin, Copeland, & Benowitz, 2014; Corrie & Kohn, 2011). The upper Sinuwa Thrust juxtaposes locally anatectic Grt-Ky metapelites in the foot wall against Grt-Ky migmatites in the hanging wall (Corrie & Kohn, 2011). The lower Bhanuwa Thrust bounds locally anatectic metapelites that show diffusionally reset garnet compositions above Grt-Ky metapelites that preserve prograde garnet zoning (Corrie & Kohn, 2011). Similarly most intra-GHS thrusts elsewhere cut Unit I metapelites (Kohn et al., 2004; Carosi, Rubatto, & Visona, 2010; Montomoli et al., 2013). In contrast, the CSZ uniquely lies above Formation III orthogneiss (Fig. 9).

If we assume along-strike continuity of the structures at the Modi Khola valley, they may correlate to unidentified thrusts in the Marsyandi in the foot wall of the CSZ.

However, the timing of the Sinuwa (ca. 27 – ca. 23 Ma), Bhanuwa (ca. 23 – 19 Ma), and Main Central (ca. 22 – ca. 15 Ma) thrusts along the Modi Khola section all overlap with movement along the CSZ (Corrie & Kohn, 2011). The timing of intra-GHS thrusting in the Langtang region (ca. 23 – ca. 16 Ma), ~ 145 km to the east, also overlaps with that of shearing along the CSZ (Kohn et al., 2004). Duration of shear on these structures is also shorter (4-7 Ma) compared to the CSZ (ca. 10 Ma)

Structures coeval with the CSZ in the Modi Khola and Langtang valleys might be related along strike through ramping across GHS formations (Corrie & Kohn, 2011). That is, the Sinuwa, Bhanuwa, and Main Central thrusts at Modi Khola, might merge into a single thrust surface at the CSZ via upward-cutting lateral ramps between the Modi Khola and Marsyandi drainages. The downwards progression from the Sinuwa thrust to the MCT implies any ramp connecting the active thrust surface in the Modi Khola drainage to the CSZ steepens over time. Similarly, a second downward trending ramp may connect the CSZ with the Langtang thrust. Intervening high topography (Annapurna, Himal Chuli, and Ganesh Himal regions) will make detailed mapping, and therefore direct correlation, difficult.

Coincident movement of intra-GHS thrusts at different structural levels could also imply that these thrusts die out laterally, eliminating the need for lateral ramps (Corrie & Kohn, 2011). The transition in the duration of thrusting, age, and thickness between thrusting surfaces from the Marsyandi to the Modi Khola corresponds to a significant along-strike decrease in thickness. In the Marsyandi the GHS is ~ 16 km thick, westward along-strike the thickness of the GHS decreases to ~4.5 km at the Modi Khola. In principle, a tectonic mechanism resulting in the change in thickness might also drive the

observed differences in intra-GHS thrusts. However, further west Carosi, Montamoli, and Visona (2007; Carosi et al. 2010) identified a single intra-GHS thrust active from ca. 26 – ca. 17 Ma, overlapping the timing of movement on the Sinuwa, Bhanuwa, and Main Central thrusts at Modi Khola, in a region where the GHS is only ~ 3 km thick. This observation suggests that variation in the position and number of thrusts does not necessarily may not be related to thickness of the GHS. If thrust stacking forms the GHS, thickness depends not just on the number of thrusts, but also on the thickness of individual sheets and the duration of emplacement.

Cooling the Greater Himalayan Sequence

Thermochronologic data illustrate anomalous late cooling in the Marsyandi relative to the Modi Khola drainge ~ 55 km to the west, and Langtang drainage ~ 145 km to the east (Fig. 10). The oldest titanite T-t data in the Marsyandi are similar to those from the Modi Khola, with temperatures of ≥ 700 °C in late-Eocene (Kohn & Corrie, 2011). In the Marsyandi temperatures of 750-830 °C persist to ca. 10 Ma, whereas titanite T-t in the Modi Khola reach peak temperatures of ~750 °C at ca. 20 Ma and subsequently cool. From west-to-east [40]Ar/[39]Ar muscovite cooling ages from Formation I decrease from ca. 10 Ma at Modi Khola to ca. 4 Ma in the Marsyandi drainage (Huntington & Hodges, 2006; Martin et al., 2014) and increase to ca. 7 Ma at Langtang (Herman et al., 2010). Zircon fission track ages in the Marsyandi are ca. 1.5 Ma (Blythe et al., 2007). Apatite fission track and (U-Th)/He ages in the Modi Khola, Marsyandi, and Langtang drainages all give similar < 1 Ma cooling ages (Blythe et al., 2007; Robert et al., 2009; Nadin & Martin, 2012).

Cooling rates for samples KN14-50A (Group I) and -18B (Group II) were ~ 35-50 °C/Ma from ca. 12 Ma to Ar closure in muscovite at ca. 4.0 Ma (Fig. 10). Similar to the Marsyandi, cooling rates in Langtang were also ~ 60 °C/Ma, but ca. 5 Ma earlier, when cooling rates in the Modi Khola were as low as ~ 20 °C/Ma (for the MCT thrust sheet).
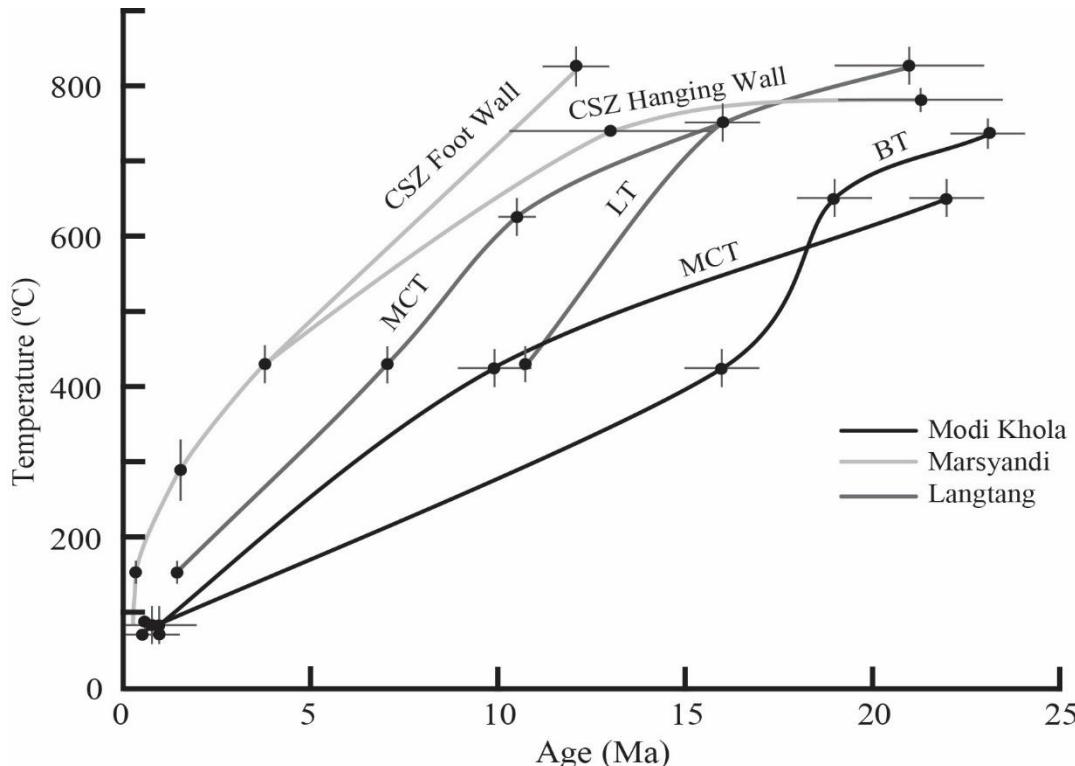
Figure 10.   Comparison of cooling in central Nepal. Data for each path are from the same structural level, except Ar[40]/Ar[39] muscovite and zircon fission track cooling ages in the Marsyandi. The early > 500 °C portions of the Modi Khola and Langtang paths come from monazite cooling ages (Kohn et al., 2004; Corrie & Kohn, 2011). Closure temperatures were calculated at 10 °C/Ma for the Modi Khola rocks , and 100 °C/Ma for the Marsyandi and Langtang rocks: 425 and 430 ± 25 °C (Ar[40]/Ar[39] muscovite, Harrison et al., 2009), 290 ± 40 °C (zircon fission tracks, Tagami & Dumitru, 1996; Tagami et al., 1996, 1998; Rahn et al., 2004), 85 ± 25 °C and 155 ± 40 °C (Apatite fission tracks, Green et al., 1986; Ketcham et al., 1999), and 72.5 and 90 ±2.5 °C (Apatite [U-Th]/He, Farley, 2000). Cooling ages from: Huntington & Hodges (2006), Blythe et al. (2007), Robert et al. (2009), Herman et al. (2010), Nadin & Martin (2012), and Martin et al. (2014).

In the Marsyandi drainage, the cooling rate between Ar closure in muscovite and fission track closure in zircon at ca. 1.5 Ma was 60 °C/Ma (Huntington & Hodges, 2006;

Blythe et al., 2007). The cooling rate drastically increased between zircon fission track closure and apatite fission track closure at ca. 0.3 Ma to 110 °C/Ma, increasing further to > 200 °C/Ma between apatite closure and the present (Blythe et al., 2007). No zircon fission track ages exist for the Modi Khola and Langtang drainages, so whether late stage rapid cooling is shared along-strike is unknown.

The transition of slow cooling (group I) or heating (group II) to rapid cooling at ca. 10 Ma may represent the initiation of exhumation or increase in exhumation rate. Assuming a lithostatic gradient, density of 2.7 g/cm^3, and pressure of 10.4 kbar result results in exhumation from a minimum of ~ 40 km depth at ca. 10 Ma. Therefore, an average erosion rate of ≥ 4.0 mm/yr would be required to expose the present surface during uplift. Erosion rates of 1.5-5 mm/yr calculated by Blythe et al. (2007) are in good agreement with our data. Modern erosion rates at the Himalayan front can exceed 5 mm/yr (Lavé & Avouac, 2001). Therefore, it is plausible that erosion could balance uplift and cooling of the GHS.

If slip on the MCT ceased by 10 Ma in the Marsyandi drainage, as it did at Langtang, another mechanism must be responsible for the majority of exhumation. The onset of rapid cooling in the Marsyandi is coincident with the initiation and main phase of growth for the Lesser Himalayan Duplex (DeCelles et al., 2001). We propose that once movement along the MCT ended, the hot rocks of the GHS may have cooled through unroofing as the GHS was passively uplifted and exhumed atop the growing Lesser Himalayan Duplex. An alternative explanation is that cooling occurred along the MCT, however, at a much later time than other locations. Both processes are also possible, i.e., shear along the MCT continued as the Lesser Himalayan Duplex formed, and exhumation

was driven by a combination of lateral and vertical movement. However, $^{40}Ar/^{39}Ar$

muscovite cooling ages are similar across MCT in the Marsyandi (Bollinger et al., 2004;

Huntington & Hodges, 2006), implying that the uppermost LHS and lowermost GHS

cooled coherently at ca. 3.8 Ma.

CHAPTER SEVEN: CONCLUSIONS

Titanite T-t data demonstrate extreme along-strike variability in structural and cooling histories within the GHS, highlighting the difficulty of laterally propagating observations made at any one location. Most striking are temperatures in excess of 750 °C at ~ 10 kbar until ca. 10 Ma and subsequent rapid cooling. This thermal history is more similar to the Namche Barwa massif in the eastern syntaxis, where rocks were ~800 °C at ~ 13 kbar until ca. 10 Ma (Booth, Chamberlain, Kidd, & Zeitler, 2009), than other transects of the central Himalaya. More work is required to assess if the more protracted construction of the GHS as a composite tectonic unit in the Marsyandi, followed by Lesser Himalayan duplexes is the best explanation for differences in T-t histories among the Modi Khola, Marsyandi, and Langtang drainages. Our model makes specific predictions for the timing of movement along the MCT and any intermediate thrusts in the Marsyandi. If our model is correct, the age and duration of slip on the MCT in the Marsyandi should be comparable to Langtang. Also, any intra-GHS thrusts between the MCT and CSZ would likely be short lived. While topography limits access to upper GHS lithologies in the Annapurna region, preventing study of a possible ramp between the Marsyandi and Modi Khola drainages, P-T-t studies of more accessible MCT related rocks along-strike can constrain how the timing of structurally higher processes may evolve laterally.

Our data have implications for future thermobarometric studies. Titanite preserves T-t information into the granulite facies, whereas other systems are more easily reset.

While sector zoning complicates interpretations, it also requires slow diffusion of Zr at 750-800 °C. Also, scapolite-plagioclase equilibria may be a useful thermometer for high-grade rocks, recording either metamorphic or metasomatic events. However, the thermometer is extremely sensitive to a_{An}, and careful consideration to equilibrium in heavily retrogressed rocks with a wide range of X_{An}.

REFERENCES

Aleinikoff, J.N., Wintsch, R.P., Tollo, R.P., Unruh, D.M., Fanning, C.J. & Schmitz, M.D., 2007. Ages and origins of rocks of the Killingworth dome, south-central Connecticut: Implications for the tectonic evolution of southern New England. *American Journal of Science*, **307**, 63-118.

Ambrose, T.K., Larson, K.P., Guilmette, C., Cottle, J.M., Buckingham, H. & Rai, S., 2015. Lateral extrusion, underplating, and out-of-sequence thrusting within the Himalayan metamorphic core, Kachenjunga, Nepal. *Lithosphere*, **L437**, 1-24.

Baker, J. & Newton, R.C., 1995. Experimentally determined activity-composition relations for Ca-rich scapolite in the system $CaAl_2Si_2O_8$-$NaAlSi_2O_8$-$CaCO_3$ at 7 kbar. *American Mineralogist*, **80**, 744-751.

Beaumont, C., Jamieson, R.A., Nguyen, M.H. & Lee, B., 2001. Himalayan tectonics explained by extrusion of a low-viscosity crustal channel coupled to focused surface denudation. *Nature*, **414**, 738-742.

Berman, R.G., 1990. Mixing properties of Ca-Mg-Fe-Mn garnets. *American Mineralogist*, **75**, 328-344.

Bollinger, L., Avouac, J.P., Beyssac, O., Catlos, E.J., Harrison, T.M., Grove, M., Goffé, B. & Sapkota, S., 2004. Thermal structure and exhumation history of the Lesser Himalaya in central Nepal. *Tectonics*, **23**, TC5015.

Booth, A.L., Chamberlain, C.P., Kidd, W.S.F. & Zeitler, P.K., 2009. Constraints on the metamorphic evolution of the eastern Himalayan syntaxis from geochronologic and petrologic studies of Namche Barwa. *GSA Bulletin*, **121**, 385-407.

Blythe, A.E., Burbank, D.W., Carter, A., Schmidt, K. & Putkonen, J., 2007. Plio-Quarternary exhumation history of the central Nepalese Himalaya: 1. Apatite and zircon fission track and apatite [U-Th]/He analyses. *Tectonics*, **26**, 1-16.

Burchfiel, B.C., Zhiliang, C., Hodges, K.V., Yuping, L., Royden, L.H., Changrong, D. & Jiene, X., 1992. The South Tibetan Detachment System, Himalayan Orogen: Extension contemporaneous with and parallel to shortening in a collisional mountain belt. *Geological Society of America Special Papers*, **269**, 1-41.

Carosi, R., Montomoli, C. & Visonà, D., 2007. A structural transect in the lower Dolpo: Insights on the tectonic evolution of western Nepal. *Journal of Asian Earth Sciences*, **29**, 407-423.

Carosi, R. Montomoli, C., Rubatto, D. & Visonà, D., 2010. Late Oligocene high-temperature shear zones in the core of the Higher Himalayan Crystallines (lower Dolpo, western Nepal). *Tectonics*, **29**, TC4029.

Catlos, E.J., Harrison, T.M., Kohn, M.J., Grove, M., Ryerson, F.J., Manning, C.E. & Upreti, B.N., 2001. Geochronologic and thermobarometric constraints on the evolution of the Main Central Thrust, central Nepal Himalaya. *Journal of Geophysical Research*, **106**, 16177-16204.

Chambers, J.A. & Kohn, M.J., 2012. Titanium in muscovite, biotite, and hornblende: modeling, thermometry, and rutile activities of metapelites and amphibolites. *American Mineralogist*, **97**, 543-555.

Cherniak, D.J., 2006. Zr diffusion in titanite. *Contributions to Mineralogy and Petrology*, **152**, 639-647.

Colchen, M., Le Fort, P. & Pêcher, A., 1986. Annapurna-Manaslu-Ganesh Himal. *Paris, Centre National de la Recherches Scientifques*, 136.

Coleman, M.E., 1996. Orogen-parallel and orogen-perpendicular extension in the central Nepalese Himalayas. *Geological Society of America Bulletin*, **108**, 1594-1607.

Coleman, M.E., 1998. U-Pb constraints on Oligocene-Miocene deformation and anataxis within the central Himalaya, Marsyandi Valley, Nepal. *American Journal of Science*, **298**, 553-571.

Coleman, M.E. & Hodges, K.V., 1998. Contrasting Oligocene and Miocene thermal histories from the hanging wall and footwall of the South Tibetan detachment in

the central Himalaya from ^{40}Ar/^{39}Ar thermochronology, Marsysandi valley, central Nepal. *Tectonics*, **17**, 726-740.

Copeland, P., Harrison, T.M., Hodges, K.V., Maruéjol, P., LeFort, P. & Pecher, A., 1991. An early Pliocene thermal disturbance in the Main Central Thrust, central Nepal: implications for Himalayan tectonics. *Journal of Geophysical Research*, **96**, 8475-8500.

Corrie, S.L. & Kohn, M.J., 2011. Metamorphic history of the Central Himalaya, Annapurna region, Nepal, and implications for tectonic models. *Geological Society of America Bulletin*, **123**, 1863-1879.

Cottle, J.M., Larson, K.P. & Kellett, D.A., 2015. How does the mid-crust accommodate deformation in large, hot collisional orogens? A review of recent research in the Himalayan orogen. *Journal of Structural Geology*, **78**, 119-133.

DeCelles, P.G., Robinson, D.M., Quade, J., Ojha, T.P., Garzione, C.N., Copeland, P. & Upreti, B.N., 2001. Stratigraphy, structure, and tectonic evolution of the Himalyan fold-thrust belt in western Nepal. *Tectonics*, **20**, 487-509.

Edwards, R.M., 1995. ^{40}Ar/^{39}Ar geochronology of the Main Central Thrust (MCT) region: evidence for late Miocene to Pliocene disturbances along the MCT, Marsyandi River valley, west-central Nepal Himalaya. *Journal of the Nepal Geological Society*, **10**, 41-46.

Farley, K.A , 2000. Helium diffusion from apatite: general behavior as illustrated by Durango fluor-apatite. *Journal of Geophysical Research*, **95**, 2903

Ferry, J.M., 1976. Metamorphism of calcareous sediments in the Waterville-Vassalboro area, south-central Maine: Mineral reactions and graphical analysis. *American Journal of Science*, **276**, 841-882.

Ferry, J.M. & Spear, F.S., 1978. Experimental calibration of the partitioning of Fe and Mg between Biotite and Garnet. *Contributions to Mineralogy and Petrology*, **66**, 113-117.

Fuhrman, M.L. & Lindsley, D., 1988. Ternary-feldspar modeling and thermometry. *American Mineralogist*, **73**, 201-215.

Gardien, V., Thompson, A.B., Grujic, D. & Ulmer, P., 1995. Experimental melting of biotite + plagioclase + quartz ± muscovite assemblages and implications for crustal melting. *Journal of Geophysical Research*, **100**, 15581-15591.

Godin, L., Grujic, D., Law, R.D. & Searle, M.P., 2006a. Channel flow, ductile extrusion, and exhumation in continental collision zones: an introduction. In:*Channel Flow, Ductile Extrusion and Exhumation in Continental Collision Zones* (eds Law, R.D., Searle, M.P. & Godin, L.), *Geological Society of London Special Publications*, **268**, 1-28.

Godin, L., Gleeson, T.P., Searle, M.P., Ullrich, T.D. & Parrish, R.R., 2006b. Locking of southward extrusion in favour of rapid crustal-scale buckling of the Greater Himalayan Sequence, Nar valley, central Nepal. In: *Channel Flow, Ductile Extrusion and Exhumation in Continental Collision Zones* (eds Law, R.D., Searle, M.P. & Godin, L.), *Geological Society of London Special Publications*, **268**, 269-292.

Green, P.F., Duddy, I.R., Gleadow, A.J.W., Tingate, P.R., & Laslett, G.M., 1986. Thermal annealing of fission tracks in Apatite: 1, A qualitative description. *Chemical Geology*, **59**, 237-253.

Harrison, T.M., Catlos, E.J. & Montel, J.M., 2002. U-Th-Pb dating of phosphate minerals. *Reviews in Mineralogy*, **48**, 523-558.

Harrison, T.M., Celerier, J., Aikman, A.B., Herman, J., & Heizler, M.T., 2009. Diffusion of ^{40}Ar in muscovite. *Geochemica et Cosmochimica Acta*, **73**, 1039-1051.

Hayden, L.A., Watson, E.B. & Wark, D.A., 2008. A thermobarometer for sphene (titanite). *Contributions to Mineralogy and Petrology*, **155**, 529-540.

Herman, F., Copeland, P., Avouac, J.P., Bollinger, L., Mahéo, G., LeFort, P., Rai, S., Foster, D., Pêcher, A., Stüwe, K. & Henry, P., 2010. Exhumation, crustal deformation, and thermal structure of the Nepal Himalaya derived from the inversion of thermochronological and thermobarometric data and modeling of the topography. *Journal of Geophysical Research*, **115**, B06407.

Hodges, K.V., Parrish, R.R., Housch, T.B., Lux, D.r., Burchfiel, B.C. & Royden, L.H., 1992. Simultaneous Miocene extension and shortening in the Himalayan orogeny. *Science*, **258**, 1466-1470.

Holland, T. & Blundy, J., 1994. Non-ideal interactions in calcic amphiboles and their bearing on amphibole-plagioclase thermometry. *Contributions to Mineralogy and Petrology*, **116**, 433-447.

Holland, T.J.B., 2002. AX: A program to calculate activities of mineral endmembers from chemical analyses. http://www.esc.cam.ac.uk/research/research-groups/research-projects/tim-hollands-software-pages/ax.

Huntington, K.W. & Hodges, K.V., 2006. A comparative study of detrital mineral and bedrock age-elevation methods for estimating erosion rates. *Journal of Geophysical Research*, **111**, F03011.

Kapp, P., Manning, C.E. & Tropper, P., 2009. Phase-equilibrium constraints on titanite and rutile activities in mafic epidote amphibolites and geobarometry using titanite-rutile equilibria. *Journal of Metamorphic Geology*, **27**, 509-521.

Ketcham, R., Donelick, R.A., & Carlson, W.D., 1999. Variability of apatite fission-track annealing kinetics: III. Extrapolation to geologic time scales. American Mineralogist,

Kohn, M.J., 2008. P-T-t data from central Nepal support critical taper and repudiate large-scale channel flow of the Greater Himalayan Sequence. *Geological Society of America Bulletin*, **120**, 259-273.

Kohn, M.J., 2014. Himalayan metamorphism and its tectonic implications. Annual Review of Earth and Planetary Sciences, **42**, 381-419.

Kohn, M.J., Catlos, E.J., Ryerson, F.J. & Harrison, M.T., 2001. Pressure-temperature-time path discontinuity in the Main Central thrust zone, central Nepal. *Geology*, **29**, 571-574.

Kohn, M.J., Wieland, M.S., Parkinson, C.D. & Upreti, B.N., 2004. Miocene faulting at plate tectonic velocity in the Himalaya of central Nepal. *Earth and Planetary Science Letters*, **228**, 299-310.

Kohn, M.J., Wieland, M.S., Parkinson, C.D. & Upreti, B.N., 2005. Five generators of monazite in Langtang gneisses: implications for chronology of the Himalayan metamorphic core. *Journal of Metamorphic Geology*, **23**, 399-406.

Kohn, M.J. & Corrie, S.L., 2011. Preserved Zr-temperatures and U-Pb ages in high-grade metamorphic titanite: Evidence for a static hot channel in the Himalayan orogen. *Earth and Planetary Science Letters*, **311**, 136-143.

Larson, K.P., Ambrose, T.K., Webb, A.A.G., Cottle, J.M. & Shrestha, S., 2015. Reconciling Himalayan midcrustal discontinuities: The Main Central thrust system. *Earth and Planetary Science Letters*, **429**, 139–146.

Lavé, J. & Avouac, J.P., 2001. Fluvial incision and tectonic uplift across the Himalayas of central Nepal. *Journal of Geophysical Research*, **106**, 26561-26591.

Le Fort, P., 1975. Himalayas: The collided range. Present knowledge of the continental arc. *American Journal of Science*, **275A**, 1-44.

Ludwig, K.R., 2012. Isoplot 3.75: a geochronological toolkit for Microsoft Excel. *Berkeley Geochronology Center Special Publication*, **5**, 1-75.

Martin, A.J., Ganguly, J. & DeCelles, P.G., 2010. Metamorphism of Greater and Lesser Himalayan rocks exposed in the Modi Khola valley, central Nepal. *Contributions to Mineralogy and Petrology*, **159**, 203-223.

Martin, A.J., Copeland, P. & Benowitz, J.A., 2014. Muscovite $^{40}Ar/^{39}Ar$ ages help reveal the Neogene tectonic evolution of the southern Annapurna Range, central Nepal. In: *Tectonics of the Himalaya* (eds Mukherjee, S., Carosi, R., van der Beek, P.A., Mukherjee, B.K. & Robinson, D.M.), *Geological Society of London Special Publications*, **412**, 199-220.

Mazdab, F.K., 2009. Characterization of flux-grown trace-element-doped titanite using high-mass-resolution ion microprobe (SHRIMP-RG). *Canadian Mineralogist*, **47**, 813-831.

Moecher, D.P. & Essene, E.J., 1990. Phase Equilibria for calcic scapolite, and implications of variable Al-Si disorder for P-T, $T-X_{CO2}$, and a-X relations. *Journal of Petrology*, **31**, 997-1024.

Montomoli, C., Iaccarino, S., Carosi, R., Langone, A. & Visonà, D., 2013. Tectonometamorphic discontinuities within the Greater Himalayan Sequence in western Nepal (central Himalaya): Insights on the exhumation of crystalline rocks. *Tectonophysics*, **608**, 1349-1370.

Montomoli, C., Carosi, R. & Iaccarino, S., 2015. Tectonometamorphic discontinuities in the Gearter Himalayan Sequence: a local or a regional feature? In: *Tectonics of the Himalaya* (eds Mukherjee, S., Carosi, R., van der Beek, P., Mukherjee, B.K. & Robinson, D.), *Geological Society of London Special Publications,* **412**, 1-41.

Nadin, E.S. & Martin, A.J., 2012. Apatite thermochronometry within a knickzone near the Higher Himalaya front, central Nepal: No resolvable fault motion in the past one million years. *Tectonics*, **31**, TC2010.

Najman, Y., Appel, E., Boudagher-Fadel, M., Bown, P., Carter, A., Garzanti, E., Godin, L., Han, J., Liebke, U., Oliver, G., Parrish, R. & Vezzoli, G., 2010. Timing of India-Asia collision: Geological, biostratigraphic, and palaeomagnetic constraints. *Journal of Geophysical Research*, **115**, B12416.

Paton, C., Hellstrom, J., Paul, B., Woodhead, J. & Hergt, J., 2011. Iolite: freeware for the visualization and processing of mass spectrometric data. *Journal of Analytical Spectrometry*, **26**, 2508.

Paterson, B.A. & Stephens, W.E., 1992. Kinetically induced compositional zoning in titanite: implications for accessory-phase/melt partitioning of trace elements. *Contributions to Mineralogy and Petrology*, **109**, 373-385.

Pêcher, A. & Le Fort, P., 1986. The metamorphism in central Himalaya, its relations with thrust tectonics. In: *Évolution des domains orogéniques d'Asie meridional (de la Turquie à l'Indoneasie)* (eds Le Fort, P., Cholchen, M. & Montenat, C.), *Science de la Terre*, **47**, 285-309.

Powell, R. & Holland, T., 1994. Optimal geothermometry and geobarometry. *American Mineralogist*, **79**, 120-133.

Powell, R. & Holland, T., 1998. Calculating phase diagrams involving solid solutions via non-linear equations, with examples using THERMOCALC. *Journal of Metamorphic Geology*, **16**, 577-588.

Robert, X., van der Beek, P., Braun, J., Perry, C., Dubille, M. & Mugnier, J.L., 2009. Assessing Quarternary reactivation of the Main Central Thrust zone (central Nepal Himalaya): New thermochronologic data and numerical modeling. *Geology*, **37**, 731-734.

Sawyer, E.W., 2008. Atlas of Migmatites. The Canadian Mineralogist Special Publications, **9**.

Schneider, C. & Masch, L., 1993. The metamorphism of the Tibetan Series from the Manang area, Marsyandi valley, central Nepal. In: *Himalayan Tectonics* (eds Treloar, P.J. & Searle, M.P.) *Geological Society of London Special Publications*, **74**, 357-374.

Searle, M.P., 2010. Low-angle normal faults in the compressional Himalayan orogen: Evidence from the Annapurna-Dhaulagiri Himalaya, Nepal. *Geosphere*, **6**, 296-315.

Spandler, C., Hammerli, J., Sha, P., Hilbert-Wolft, H., Hu, Y., Roberts, E. & Schmitz, M., 2016. MKED1: A new titanite standard for in situ analyses of Sm-Nd isotopes and U-Pb geochronology. *Chemical Geology*, **425**, 110-126.

Spencer, K.J., Hacker, B.R., Kylander-Clark, A.R.C., Andersen, T.B., Cottle, J.M., Stearns, M.A., Poletti, J.E. & Seward, G.G.E., (2013). Campaign-style titanite U-Pb dating by laser-ablation ICP: implications for crustal flow, phase transformations and titanite closure. *Chemical Geology*, **341**, 84-101.

Stearns, M.A., Cottle, J.M., Hacker, B.R., Kylander-Clark, A.R.C., 2016. Extracting thermal histories from the near-rim zoning in titanite using coupled U-Pb and trace element depth profiles by single-shot laser-ablation split stream (SS-LASS) ICP-MS. *Chemical Geology,* **422**, 13-24.

Rahn, M.K., Brandon, M.T., Batt, G.E., & Garver, J.I., 2004. A zero-damage model for fission-track annealing in Zircon. *American Mineralogist*, **89**, 473-484.

Tagami, T., & Dumitru, T.A., 1996. Provenance and thermal history of the Franciscan accretionary complex: Constraints from fission track thermochronology. *Journal of Geophysical Research*, **101**, 11353-11364.

Tagami, T., Carter, A., & Hurford, A.J., 1996. Natural long-term annealing of the zircon fission track system in Vienna Basin deep borehole samples: Constraints upon the partial annealing zone and closure temperature. *Chemical Geology*, **130**, 147-157.

Tagami, T., Galbraith, R.F., Yamada, R., & Laslett, G.M., 1998. Revised annealing kinetics of fission tracks in zircon and geological implications. In: *Advances in Fission-Track Geochronology* (eds Van den Haute, P., & De Corte, F.), *Springer*, 99-112.

Thomas, J.B., Watson, E.B., Spear, F.S., Shemella, P.T., Nayak, S.K. & Lanzirotti, A., 2010. TitaniQ under pressure: The effect of pressure and temperature on the solubility of Ti in quartz. *Contributions to Mineralogy and Petrology*, **160**, 743-759.

Vannay, J.C. & Hodges, K.V., 1996. Tectonometamorphic evolution of the Himalayan metamorphic core between the Annapurna and Dhaulagiri, central Nepal. *Journal of Metamorphic Geology*, **14**, 635-656.

Yin, A. & Harrison, T.M., 2000. Geologic evolution of the Himalayan-Tibetan Orogen. *Annual Reviews in Earth and Planetary Science*, **28**, 211-280.

Yin, A., 2006. Cenozoic tectonic evolution of the Himalayan orogeny as constrained by along-strike variation of structural geometry, exhumation history, and foreland sedimentation. *Earth-Science Reviews*, **76**, 1-131.

APPENDIX A

Electron Microprobe Data

Table A.1   Plagioclase Compositions

Analysis	1	2	3	4	5	6	7
Sample (KN14-)	18B	18B	18B	20E2	20E2	20E2	20E2
SiO_2	60.99	61.73	61.66	58.65	59.28	56.50	61.35
Al_2O_3	24.76	24.21	24.31	25.51	25.41	27.43	24.33
FeO	0.07	0.06	0.00	0.04	0.06	0.07	0.00
CaO	5.96	5.22	5.45	7.20	6.93	8.90	6.10
Na_2O	8.77	9.10	9.16	7.80	8.00	6.76	8.40
K_2O	0.14	0.19	0.11	0.19	0.13	0.17	0.16
Total	100.69	100.50	100.70	99.39	99.82	99.82	100.33
Si	2.680	2.713	2.703	2.622	2.637	2.528	2.714
Al	1.282	1.254	1.256	1.344	1.332	1.446	1.268
Fe	0.003	0.002	0.000	0.002	0.002	0.003	0.000
Ca	0.281	0.246	0.256	0.345	0.330	0.427	0.289
Na	0.747	0.775	0.779	0.676	0.690	0.586	0.720
K	0.008	0.010	0.006	0.011	0.007	0.010	0.009
Total	5.000	5.000	5.000	5.000	5.000	5.000	5.000
An	27.10	23.83	24.61	33.43	32.13	41.73	28.38
Ab	72.14	75.16	74.82	65.51	67.14	57.33	70.74
Or	0.75	1.01	0.57	1.06	0.73	0.93	0.88
Analysis	8	9	10	11	12	13	14
Sample (KN14-)	22B	22B	22B	24A	24A	24A	24A
SiO_2	50.57	56.82	50.50	43.77	43.96	44.72	43.43
Al_2O_3	31.45	26.79	31.39	35.50	35.58	35.45	35.49
FeO	0.02	0.04	0.00	0.04	0.00	0.00	0.09
CaO	13.78	8.78	13.83	19.10	19.15	18.56	19.12
Na_2O	3.86	7.11	3.87	0.48	0.53	0.86	0.50
K_2O	0.06	0.16	0.06	0.01	0.01	0.01	0.01
Total	99.74	99.69	99.65	98.90	99.23	99.60	98.63
Si	2.299	2.541	2.298	2.044	2.045	2.069	2.033
Al	1.685	1.412	1.683	1.954	1.951	1.933	1.958
Fe	0.001	0.001	0.000	0.002	0.000	0.000	0.003
Ca	0.671	0.421	0.674	0.956	0.955	0.920	0.959
Na	0.341	0.616	0.341	0.043	0.048	0.077	0.045
K	0.004	0.009	0.004	0.001	0.001	0.001	0.001
Total	5.000	5.000	5.000	5.000	5.000	5.000	5.000
An	66.11	40.22	66.16	95.61	95.15	92.19	95.42
Ab	33.54	58.90	33.48	4.32	4.79	7.72	4.52
Or	0.35	0.87	0.35	0.07	0.05	0.08	0.07

| Analysis | 15 | 16 | 17 | 18 | 19 | 20 | 21 |
Sample (KN14-)	24A	56B	56B	56B	53A	53A	53A
SiO_2	43.96	61.19	59.59	58.82	59.82	63.70	60.41
Al_2O_3	35.36	24.17	25.68	26.05	25.74	22.78	25.50
FeO	0.06	0.00	0.11	0.08	0.06	0.03	0.03
CaO	18.80	5.78	7.19	7.70	7.17	3.83	7.03
Na_2O	0.63	8.81	7.79	7.47	7.94	9.93	7.99
K_2O	0.01	0.20	0.29	0.15	0.21	0.09	0.16
Total	98.83	100.14	100.65	100.26	100.93	100.35	101.13
Si	2.053	2.703	2.634	2.614	2.634	2.793	2.656
Al	1.946	1.258	1.338	1.365	1.336	1.177	1.322
Fe	0.002	0.000	0.004	0.003	0.002	0.001	0.001
Ca	0.941	0.274	0.340	0.367	0.338	0.180	0.331
Na	0.057	0.754	0.667	0.643	0.678	0.844	0.681
K	0.001	0.011	0.017	0.008	0.012	0.005	0.009
Total	5.000	5.000	5.000	5.000	5.000	5.000	5.000
An	94.21	26.34	33.24	36.02	32.91	17.47	32.46
Ab	5.70	72.60	65.14	63.18	65.97	82.06	66.69
Or	0.08	1.06	1.61	0.81	1.12	0.47	0.86
Analysis	22	23	24	25	26	27	28
Sample (KN14-)	53A	33B	33B	33B	33B	33B	33B
SiO_2	63.41	51.22	51.84	57.80	55.83	52.39	57.90
Al_2O_3	22.76	30.54	29.98	25.45	27.35	29.56	25.82
FeO	0.05	0.01	0.04	0.00	0.01	0.03	0.00
CaO	4.04	13.28	12.71	7.72	9.30	12.29	7.79
Na_2O	9.53	3.91	4.33	7.63	6.36	4.55	7.41
K_2O	0.31	0.10	0.11	0.09	0.12	0.11	0.12
Total	100.09	99.06	99.01	98.69	98.96	98.94	99.04
Si	2.794	2.346	2.370	2.604	2.526	2.394	2.603
Al	1.182	1.649	1.615	1.352	1.458	1.592	1.368
Fe	0.002	0.000	0.002	0.000	0.000	0.001	0.000
Ca	0.191	0.652	0.623	0.372	0.451	0.602	0.375
Na	0.814	0.347	0.384	0.666	0.558	0.403	0.646
K	0.017	0.006	0.006	0.005	0.007	0.007	0.007
Total	5.000	5.000	5.000	5.000	5.000	5.000	5.000
An	18.66	64.86	61.47	35.67	44.39	59.50	36.49
Ab	79.66	34.55	37.91	63.84	54.95	39.85	62.84
Or	1.68	0.59	0.62	0.49	0.66	0.66	0.68

Analysis	29	30	31	32	33
Sample (KN14-)	51A	51A	50A	50A	50A
SiO_2	43.15	43.34	59.75	56.16	57.83
Al_2O_3	35.94	36.55	25.21	26.94	26.72
FeO	0.00	0.01	0.07	0.31	0.25
CaO	19.97	19.91	6.95	9.24	8.50
Na_2O	0.25	0.20	7.92	6.63	7.12
K_2O	0.01	0.00	0.20	0.15	0.11
Total	99.33	100.01	100.10	99.43	100.52
Si	2.009	2.004	2.654	2.527	2.568
Al	1.972	1.992	1.320	1.429	1.399
Fe	0.000	0.001	0.003	0.012	0.009
Ca	0.996	0.986	0.330	0.446	0.405
Na	0.022	0.018	0.682	0.579	0.613
K	0.001	0.000	0.011	0.009	0.006
Total	5.000	5.000	5.000	5.000	5.000
An	97.75	98.21	32.28	43.14	39.53
Ab	2.19	1.79	66.62	56.03	59.87
Or	0.06	0.00	1.10	0.83	0.60

Table A.2   Alkali Feldspar Compositions

Analysis	1	2	3	4	5	6	7
Sample (KN14-)	18B	18B	18B	20E2	20E2	22B	22B
SiO_2	64.91	64.70	64.61	64.51	64.92	64.44	64.80
Al_2O_3	18.44	18.57	18.76	18.15	18.75	18.54	18.66
FeO	0.03	0.10	0.03	0.02	0.06	0.01	0.00
CaO	0.00	0.02	0.00	0.00	0.03	0.03	0.09
Na_2O	0.79	0.76	0.77	0.91	1.10	0.95	0.67
K_2O	15.74	15.62	15.58	15.60	15.30	15.50	16.08
Total	99.92	99.76	99.75	99.18	100.16	99.45	100.30
Si	2.997	2.993	2.988	2.998	2.985	2.985	2.981
Al	1.004	1.012	1.023	0.994	1.016	1.012	1.012
Fe	0.001	0.004	0.001	0.001	0.002	0.000	0.000
Ca	0.000	0.001	0.000	0.000	0.001	0.001	0.004
Na	0.071	0.068	0.069	0.082	0.098	0.086	0.060
K	0.927	0.922	0.919	0.925	0.897	0.916	0.943
Total	5.000	5.000	5.000	5.000	5.000	5.000	5.000
An	0.01	0.11	0.00	0.00	0.14	0.13	0.42
Ab	7.09	6.83	7.01	8.16	9.84	8.53	5.96
Or	92.89	93.05	92.99	91.83	90.02	91.34	93.62
Analysis	8	9	10	11	12	13	14
Sample (KN14-)	56B	56B	53A	53A	33B	33B	51A
SiO_2	65.23	64.90	64.51	64.57	64.10	63.96	64.87
Al_2O_3	18.58	18.36	18.49	18.45	18.30	18.39	18.41
FeO	0.02	0.03	0.05	0.03	0.04	0.01	0.00
CaO	0.04	0.02	0.00	0.00	0.01	0.06	0.00
Na_2O	1.22	0.90	0.64	0.50	0.75	0.78	0.31
K_2O	15.19	15.68	16.08	16.36	15.81	15.60	16.52
Total	100.27	99.89	99.77	99.91	99.00	98.80	100.11
Si	2.995	2.995	2.984	2.984	2.986	2.986	2.996
Al	1.005	0.999	1.008	1.005	1.005	1.011	1.002
Fe	0.001	0.001	0.002	0.001	0.001	0.000	0.000
Ca	0.002	0.001	0.000	0.000	0.000	0.003	0.000
Na	0.108	0.081	0.057	0.045	0.068	0.071	0.028
K	0.889	0.923	0.949	0.964	0.939	0.929	0.973
Total	5.000	5.000	5.000	5.000	5.000	5.000	5.000
An	0.17	0.12	0.02	0.00	0.05	0.29	0.00
Ab	10.83	8.02	5.70	4.44	6.71	7.04	2.81
Or	89.00	91.86	94.28	95.56	93.24	92.66	97.19

Analysis	15	16
Sample (KN14-)	51A	50A
SiO$_2$	64.54	65.18
Al$_2$O$_3$	18.35	18.37
FeO	0.00	0.09
CaO	0.02	0.00
Na$_2$O	0.39	1.09
K$_2$O	16.34	15.06
Total	99.65	99.79
Si	2.994	3.011
Al	1.003	1.000
Fe	0.000	0.004
Ca	0.001	0.000
Na	0.035	0.098
K	0.967	0.887
Total	5.000	5.000
An	0.09	0.00
Ab	3.51	9.93
Or	96.39	90.07

Table A.3   **Scapolite Compositions** [1]

Analysis Sample (KN14-)	1 18B	2 20E2	3 22B	4 24A	5 33B	6 50A
SiO_2	48.85	48.48	46.44	44.59	46.42	46.11
Al_2O_3	26.23	26.44	27.17	27.39	26.84	27.62
FeO	0.14	0.15	0.11	0.00	0.01	0.15
MnO	0.04	0.00	0.00	0.06	0.00	0.00
MgO	0.00	0.00	0.03	0.01	0.02	0.01
CaO	15.03	15.81	17.89	17.66	17.09	18.48
Na_2O	5.24	4.65	3.49	3.05	3.57	3.13
K_2O	0.44	0.46	0.11	0.34	0.35	0.11
SO_3	0.06	0.10	0.02	0.01	0.00	0.00
Cl	0.98	0.71	0.02	0.39	0.35	0.00
Total	97.01	96.80	95.27	93.49	94.66	95.62
O=Cl	-0.22	-0.16	0.00	-0.09	-0.08	0.00
Total	96.79	96.64	95.27	93.40	94.58	95.62
Si	7.349	7.304	7.112	6.983	7.156	7.045
Al	4.651	4.696	4.903	5.054	4.878	4.974
Fe	0.018	0.019	0.015	0.000	0.001	0.020
Mn	0.004	0.000	0.000	0.008	0.000	0.000
Mg	0.000	0.000	0.006	0.001	0.005	0.002
Ca	2.423	2.553	2.934	2.963	2.824	3.025
Na	1.527	1.359	1.035	0.925	1.066	0.928
K	0.084	0.089	0.021	0.067	0.070	0.021
Total	16.055	16.020	16.026	16.000	15.999	16.015
SO_4	0.007	0.010	0.002	0.001	0.000	0.000
Cl	0.232	0.168	0.004	0.093	0.083	0.000
CO_3 [2]	0.761	0.821	0.994	0.906	0.917	1.000
X_{Me}	0.60	0.64	0.74	0.75	0.71	0.76
X_{EqAn}	0.55	0.57	0.63	0.68	0.63	0.66

[1] Atomic proportions normalized to Al + Si = 12
[2] CO3 = 1 - (Cl + SO3)

Table A.4   **Amphibole Compositions** [1]

Analysis		1	2	3	4	5	6	7
Location		rim	core	core	rim	incl, core	incl, rim	core
Sample (KN14-)		18B	18B	20E2	20E2	22B	22B	24A
SiO_2		42.08	42.36	40.52	40.64	53.05	53.33	53.11
TiO_2		0.43	0.41	1.48	1.29	0.10	0.08	0.01
Al_2O_3		11.24	10.63	13.45	12.96	3.75	3.35	1.95
FeO		20.25	20.71	17.39	18.81	12.75	12.11	14.30
MnO		0.18	0.27	0.10	0.23	0.07	0.05	0.16
MgO		7.87	8.16	8.21	7.79	14.86	15.16	13.63
CaO		11.64	11.69	11.64	11.73	12.49	12.67	12.32
Na_2O		1.35	1.44	1.18	1.20	0.64	0.54	0.16
K_2O		1.55	1.41	2.16	2.02	0.06	0.07	0.13
F		0.30	0.37	0.33	0.28	0.57	0.49	0.22
Cl		0.32	0.24	0.07	0.25	0.00	0.02	0.01
Subtotal		97.21	97.69	96.51	97.18	98.32	97.86	96.00
O=F,Cl		-0.20	-0.21	-0.15	-0.17	-0.24	-0.21	-0.09
Total		97.01	97.48	96.36	97.01	98.08	97.65	95.90
T:	Si	6.469	6.478	6.228	6.248	7.607	7.662	7.858
	Al_{iv}	1.531	1.522	1.772	1.752	0.393	0.338	0.142
M(1-3):	Al_{vi}	0.506	0.394	0.664	0.597	0.241	0.229	0.198
	Ti	0.049	0.048	0.171	0.149	0.011	0.008	0.001
	Fe^{3+}	0.415	0.528	0.229	0.282	0.179	0.139	-0.023
	Mg	1.802	1.860	1.881	1.784	3.175	3.245	3.006
	Mn	0.024	0.035	0.013	0.030	0.008	0.007	0.020
	Fe^{2+}	2.188	2.121	2.007	2.136	1.350	1.317	1.792
	Ca	0.015	0.014	0.035	0.022	0.036	0.056	0.006
M4:	Fe	0.000	0.000	0.000	0.000	0.000	0.000	0.000
	Ca	1.903	1.902	1.882	1.910	1.882	1.895	1.947
	Na	0.097	0.098	0.118	0.090	0.118	0.105	0.053
A:	Na	0.306	0.328	0.232	0.268	0.059	0.045	-0.008
	K	0.303	0.275	0.423	0.397	0.011	0.013	0.025
OH:	OH	1.769	1.757	1.822	1.799	1.740	1.774	1.896
	F	0.148	0.181	0.161	0.135	0.260	0.222	0.102
	Cl	0.083	0.062	0.017	0.066	0.000	0.004	0.003
Total		15.609	15.603	15.656	15.665	15.070	15.059	15.017
Sum A		0.609	0.603	0.656	0.665	0.070	0.059	0.017
$Mg/(Mg+Fe^{2+})$		0.452	0.467	0.484	0.455	0.702	0.711	0.626

Analysis		8	9	10	11	12	13	14
Location		rim	rim	core	rim	core	rim	rim
Sample (KN14-)		24A	56B	56B	53A	53A	53A	33B
SiO_2		42.63	42.28	41.73	54.46	54.00	55.05	52.88
TiO_2		0.16	0.44	0.56	0.07	0.03	0.01	0.08
Al_2O_3		11.73	11.60	12.47	2.35	2.79	1.83	3.15
FeO		19.32	18.69	19.46	9.23	9.08	9.63	10.09
MnO		0.03	0.32	0.26	0.23	0.33	0.34	0.02
MgO		7.89	8.44	8.24	16.88	16.74	16.69	16.38
CaO		11.84	11.54	11.61	12.78	12.71	12.84	12.58
Na_2O		0.88	1.50	1.45	0.36	0.47	0.25	0.28
K_2O		1.38	2.05	2.08	0.19	0.23	0.10	0.21
F		0.26	0.99	0.98	0.50	0.54	0.47	0.26
Cl		0.19	0.02	0.03	0.00	0.01	0.01	0.01
Subtotal		96.32	97.85	98.87	97.04	96.93	97.22	95.93
O=F,Cl		-0.16	-0.42	-0.42	-0.21	-0.23	-0.20	-0.11
Total		96.16	97.43	98.45	96.83	96.70	97.02	95.82
T:	Si	6.542	6.473	6.335	7.804	7.749	7.885	7.675
	Al_{iv}	1.458	1.527	1.665	0.196	0.251	0.115	0.325
M(1-3):	Al_{vi}	0.664	0.567	0.567	0.201	0.221	0.194	0.214
	Ti	0.019	0.050	0.064	0.007	0.003	0.001	0.008
	Fe^{3+}	0.386	0.273	0.364	0.027	0.068	-0.019	0.080
	Mg	1.804	1.926	1.863	3.605	3.580	3.563	3.543
	Mn	0.004	0.041	0.033	0.028	0.040	0.042	0.003
	Fe^{2+}	2.094	2.120	2.107	1.080	1.023	1.172	1.144
	Ca	0.029	0.023	0.002	0.052	0.065	0.047	0.008
M4:	Fe	0.000	0.000	0.000	0.000	0.000	0.000	0.000
	Ca	1.918	1.871	1.887	1.910	1.890	1.925	1.949
	Na	0.082	0.129	0.113	0.090	0.110	0.069	0.051
A:	Na	0.180	0.315	0.315	0.009	0.022	0.000	0.026
	K	0.271	0.401	0.403	0.035	0.043	0.019	0.039
OH:	OH	1.821	1.515	1.521	1.775	1.755	1.783	1.879
	F	0.129	0.480	0.473	0.225	0.243	0.214	0.119
	Cl	0.051	0.005	0.006	0.000	0.002	0.003	0.002
Total		15.451	15.715	15.718	15.044	15.065	15.013	15.065
Sum A		0.451	0.715	0.718	0.044	0.065	0.013	0.065
$Mg/(Mg+Fe^{2+})$		0.463	0.476	0.469	0.770	0.778	0.752	0.756

Analysis		15	16	17	18	19
Location		core	rim	rim	rim	core
Sample (KN14-)		33B	33B	51A	50A	50A
SiO_2		54.03	49.12	54.99	40.94	40.86
TiO_2		0.07	0.05	0.16	1.08	1.10
Al_2O_3		2.09	7.14	3.29	12.88	12.96
FeO		10.21	11.36	5.93	21.00	21.02
MnO		0.05	0.04	0.02	0.20	0.13
MgO		16.84	14.50	19.10	6.08	6.29
CaO		12.57	12.38	13.05	11.47	11.46
Na_2O		0.16	0.65	0.17	0.99	1.02
K_2O		0.20	0.67	0.21	1.74	1.79
F		0.31	0.34	0.21	0.27	0.19
Cl		0.01	0.04	0.03	0.01	0.01
Subtotal		96.53	96.29	97.16	96.66	96.84
O=F,Cl		-0.13	-0.15	-0.09	-0.12	-0.08
Total		96.39	96.14	97.07	96.55	96.75
T:	Si	7.797	7.183	7.725	6.347	6.317
	Al_{iv}	0.203	0.817	0.275	1.653	1.683
M(1-3):	Al_{vi}	0.153	0.414	0.271	0.701	0.678
	Ti	0.007	0.005	0.017	0.126	0.128
	Fe^{3+}	0.027	0.258	-0.014	0.285	0.315
	Mg	3.622	3.160	3.999	1.405	1.450
	Mn	0.006	0.005	0.003	0.026	0.017
	Fe^{2+}	1.186	1.131	0.711	2.437	2.403
	Ca	0.000	0.027	0.014	0.019	0.011
M4:	Fe	0.020	0.000	0.000	0.000	0.000
	Ca	1.944	1.914	1.950	1.886	1.888
	Na	0.036	0.086	0.045	0.114	0.112
A:	Na	0.009	0.096	0.000	0.184	0.193
	K	0.036	0.126	0.038	0.344	0.354
OH:	OH	1.855	1.833	1.901	1.863	1.902
	F	0.142	0.156	0.092	0.135	0.095
	Cl	0.003	0.011	0.006	0.002	0.003
Total		15.045	15.222	15.034	15.528	15.547
Sum A		0.045	0.222	0.034	0.528	0.547
$Mg/(Mg+Fe^{2+})$		0.753	0.736	0.849	0.366	0.376

[1]Normalization after Holland and Blundy (1994)

Table A.5   **Diopside Compositions**

Analysis	1	2	3	4	5	6	7
Location	Core	Rim	Rim	Core	core	rim	rim
Sample (KN14-)	18B	18B	18B	18B	22B	22B	24A
SiO$_2$	51.98	52.77	52.95	51.87	53.50	53.38	51.95
TiO$_2$	0.06	0.15	0.02	0.05	0.00	0.05	0.02
Al$_2$O$_3$	1.40	0.26	0.57	1.15	0.46	0.68	0.51
FeO	13.71	13.82	11.78	14.50	9.57	9.48	12.58
MnO	0.22	0.23	0.22	0.25	0.14	0.13	0.16
MgO	9.15	9.18	10.66	8.68	11.84	11.82	9.64
CaO	22.99	23.80	23.53	22.85	24.07	24.23	23.90
Na$_2$O	0.43	0.14	0.28	0.39	0.17	0.23	0.12
Total	99.94	100.35	100.01	99.73	99.74	100.00	98.87
Si	1.991	2.022	2.011	1.999	2.020	2.009	2.009
Ti	0.002	0.004	0.000	0.001	0.000	0.001	0.001
Al	0.063	0.012	0.026	0.052	0.020	0.030	0.023
Fe	0.439	0.443	0.374	0.467	0.302	0.298	0.407
Mn	0.007	0.008	0.007	0.008	0.004	0.004	0.005
Mg	0.522	0.525	0.604	0.499	0.666	0.663	0.556
Ca	0.943	0.977	0.957	0.944	0.974	0.977	0.990
Na	0.032	0.011	0.021	0.029	0.012	0.017	0.009
Total	4.000	4.000	4.000	4.000	4.000	4.000	4.000
Mg/(Mg+Fe)	0.54	0.54	0.62	0.52	0.69	0.69	0.58
Analysis	8	9	10	11	12	13	14
Location	core	rim	rim	core	core	core	rim
Sample (KN14-)	24A	24A	24A	53A	53A	33B	33B
SiO$_2$	51.89	51.92	51.66	53.75	54.26	53.41	52.95
TiO$_2$	0.05	0.03	0.03	0.02	0.01	0.00	0.03
Al$_2$O$_3$	0.85	0.53	0.79	0.47	0.19	0.30	0.45
FeO	12.79	13.03	12.32	7.52	6.66	6.96	8.41
MnO	0.20	0.25	0.17	0.43	0.41	0.10	0.01
MgO	9.56	9.26	9.83	12.86	13.42	13.88	12.92
CaO	23.28	23.44	23.66	24.05	24.59	24.20	23.99
Na$_2$O	0.15	0.18	0.15	0.26	0.11	0.07	0.09
Total	98.76	98.64	98.62	99.36	99.65	98.93	98.85
Si	2.010	2.018	1.999	2.020	2.029	2.007	2.004
Ti	0.001	0.001	0.001	0.000	0.000	0.000	0.001
Al	0.039	0.024	0.036	0.021	0.008	0.013	0.020
Fe	0.414	0.424	0.399	0.236	0.208	0.219	0.266
Mn	0.006	0.008	0.006	0.014	0.013	0.003	0.000
Mg	0.552	0.536	0.567	0.721	0.748	0.778	0.729
Ca	0.966	0.976	0.981	0.969	0.985	0.974	0.973
Na	0.011	0.013	0.011	0.019	0.008	0.005	0.007
Total	4.000	4.000	4.000	4.000	4.000	4.000	4.000
Mg/(Mg+Fe)	0.57	0.56	0.59	0.75	0.78	0.78	0.73

Analysis	15	16	17
Location	rim	rim	core
Sample (KN14-)	33B	51A	51A
SiO_2	53.09	54.60	54.69
TiO_2	0.05	0.05	0.05
Al_2O_3	0.87	0.47	0.71
FeO	7.76	3.35	3.23
MnO	0.07	0.06	0.07
MgO	13.26	16.36	16.45
CaO	23.72	24.87	24.70
Na_2O	0.20	0.05	0.09
Total	99.03	99.80	99.98
Si	1.998	2.001	1.998
Ti	0.001	0.001	0.001
Al	0.039	0.020	0.031
Fe	0.244	0.103	0.099
Mn	0.002	0.002	0.002
Mg	0.744	0.894	0.896
Ca	0.957	0.976	0.967
Na	0.014	0.003	0.006
Total	4.000	4.000	4.000
Mg/(Mg+Fe)	0.75	0.90	0.90

Table A.6   Biotite Compositions

Analysis	1	2	3	4	5	6	7
Sample (KN14-)	20E2	22B	56B	53A	33B	51A	50A
SiO_2	36.80	39.90	39.24	39.43	38.04	40.45	36.49
TiO_2	2.96	0.68	0.68	0.61	1.53	1.20	2.62
Al_2O_3	15.89	14.85	14.78	14.51	15.85	14.74	17.61
FeO	19.03	12.25	17.19	11.48	13.95	10.48	22.18
MnO	0.16	0.00	0.17	0.24	0.08	0.07	0.07
MgO	10.11	16.09	12.09	17.09	13.47	17.52	6.73
CaO	0.00	0.00	0.00	0.11	0.09	0.02	0.02
Na_2O	0.05	0.06	0.05	0.06	0.00	0.02	0.02
K_2O	9.95	9.83	9.61	9.90	9.86	9.94	9.84
F	0.47	1.25	1.94	1.67	0.67	0.74	0.39
Cl	0.21	0.03	0.02	0.03	0.07	0.19	0.01
Subtotal	95.63	94.96	95.76	95.11	93.60	95.36	95.98
O=F,Cl	-0.25	-0.53	-0.82	-0.71	-0.30	-0.36	-0.17
Total	95.38	94.42	94.94	94.40	93.30	95.01	95.81
Si	5.635	5.945	5.981	5.893	5.788	5.929	5.613
Al_{iv}	2.365	2.055	2.019	2.107	2.212	2.071	2.387
Al_{vi}	0.504	0.554	0.636	0.450	0.630	0.476	0.807
Ti	0.340	0.076	0.078	0.068	0.175	0.132	0.303
Fe	2.438	1.527	2.191	1.435	1.775	1.285	2.854
Mn	0.020	0.001	0.022	0.030	0.010	0.009	0.009
Mg	2.309	3.574	2.746	3.807	3.055	3.828	1.543
Ca	0.000	0.000	0.000	0.017	0.014	0.003	0.002
Na	0.014	0.017	0.015	0.018	0.000	0.006	0.006
K	1.944	1.869	1.868	1.887	1.913	1.859	1.931
OH	3.718	3.403	3.061	3.205	3.659	3.608	3.807
F	0.227	0.589	0.935	0.789	0.323	0.344	0.191
Cl	0.055	0.008	0.005	0.006	0.018	0.048	0.002
Total	19.569	19.617	19.555	19.712	19.573	19.598	19.455

Analysis	8
Sample (KN14-)	50A
SiO_2	35.34
TiO_2	2.87
Al_2O_3	17.24
FeO	22.03
MnO	0.07
MgO	6.84
CaO	0.02
Na_2O	0.07
K_2O	9.53
F	0.33
Cl	0.02
Subtotal	94.35
O=F,Cl	-0.14
Total	94.21
Si	5.540
Al_{iv}	2.460
Al_{vi}	0.727
Ti	0.338
Fe	2.889
Mn	0.009
Mg	1.598
Ca	0.003
Na	0.022
K	1.905
OH	3.833
F	0.163
Cl	0.005
Total	19.492

Table A.7   Epidote Compositions[1]

Analysis Sample (KN14-)	1 18B	2 18B	3 18B	4 20E2	5 20E2	6 20E2	7 20E2
SiO_2	38.86	38.75	38.53	38.50	38.22	38.08	38.23
TiO_2	0.12	0.10	0.03	0.11	0.12	0.07	0.08
Al_2O_3	26.69	27.15	26.25	24.69	24.56	24.88	24.88
Fe_2O_3	10.63	9.58	11.24	13.26	12.99	13.33	13.41
MnO	0.06	0.08	0.09	0.11	0.08	0.09	0.12
MgO	0.01	0.01	0.00	0.00	0.00	0.00	0.00
CaO	23.21	23.37	23.39	23.13	22.96	22.94	22.98
Na_2O	0.00	0.00	0.00	0.00	0.00	0.00	0.01
H_2O	1.93	1.93	1.92	1.91	1.89	1.90	1.91
Total	101.51	100.97	101.45	101.71	100.82	101.29	101.61
Si	2.998	2.998	2.985	2.995	2.998	2.976	2.979
Ti	0.007	0.006	0.002	0.007	0.007	0.004	0.005
Al	2.427	2.476	2.397	2.264	2.270	2.291	2.284
Fe^{3+}	0.617	0.558	0.655	0.776	0.767	0.784	0.786
Mn	0.004	0.005	0.006	0.007	0.005	0.006	0.008
Mg	0.001	0.001	0.000	0.000	0.000	0.000	0.000
Ca	1.918	1.937	1.942	1.928	1.929	1.921	1.918
Na	0.000	0.000	0.000	0.000	0.000	0.000	0.001
OH	1.000	1.000	1.000	1.000	1.000	1.000	1.000
Total	8.973	8.980	8.987	8.978	8.977	8.982	8.982
Fe/(Fe+Al)	0.20	0.18	0.21	0.26	0.25	0.25	0.26

Analysis	8	9	10	11	12	13	14
Sample (KN14-)	22B	22B	24A	24A	24A	56B	56B
SiO_2	39.32	39.47	38.95	38.44	38.56	38.45	38.29
TiO_2	0.00	0.00	0.00	0.01	0.08	0.03	0.02
Al_2O_3	30.14	30.34	28.75	28.43	27.07	26.79	26.31
Fe_2O_3	5.38	5.55	7.12	7.62	9.40	10.17	11.12
MnO	0.01	0.00	0.00	0.04	0.00	0.07	0.11
MgO	0.00	0.00	0.00	0.00	0.01	0.00	0.00
CaO	23.92	23.84	23.41	23.50	23.28	23.32	23.27
Na_2O	0.00	0.00	0.00	0.00	0.00	0.00	0.00
H_2O	1.96	1.96	1.93	1.92	1.91	1.92	1.91
Total	100.72	101.16	100.17	99.95	100.31	100.74	101.03
Si	3.003	3.001	3.008	2.985	3.000	2.988	2.978
Ti	0.000	0.000	0.000	0.000	0.005	0.002	0.001
Al	2.714	2.719	2.617	2.602	2.482	2.454	2.412
Fe^{3+}	0.309	0.317	0.414	0.446	0.550	0.595	0.651
Mn	0.001	0.000	0.000	0.002	0.000	0.005	0.007
Mg	0.000	0.000	0.000	0.000	0.001	0.000	0.000
Ca	1.958	1.943	1.937	1.955	1.941	1.942	1.939
Na	0.000	0.000	0.000	0.000	0.000	0.000	0.000
OH	1.000	1.000	1.000	1.000	1.000	1.000	1.000
Total	8.985	8.980	8.976	8.991	8.979	8.985	8.989
Fe/(Fe+Al)	0.10	0.10	0.14	0.15	0.18	0.20	0.21
Analysis	15	16	17	18	19	20	21
Sample (KN14-)	53A	53A	53A	33B	33B	50A	50A
SiO_2	38.15	38.28	37.82	38.94	39.06	38.73	38.67
TiO_2	0.07	0.05	0.12	0.00	0.01	0.00	0.00
Al_2O_3	25.33	25.20	26.93	29.46	30.35	28.06	27.93
Fe_2O_3	12.47	12.86	9.77	5.80	4.93	8.77	8.85
MnO	0.07	0.09	0.22	0.01	0.00	0.08	0.09
MgO	0.02	0.03	0.03	0.02	0.02	0.00	0.00
CaO	23.20	23.02	23.25	23.78	23.78	23.49	23.58
Na_2O	0.00	0.00	0.00	0.01	0.00	0.00	0.00
H_2O	1.90	1.91	1.90	1.94	1.95	1.93	1.93
Total	101.21	101.43	100.05	99.97	100.10	101.05	101.04
Si	2.977	2.982	2.962	3.004	2.998	2.985	2.983
Ti	0.004	0.003	0.007	0.000	0.000	0.000	0.000
Al	2.329	2.313	2.486	2.679	2.745	2.548	2.539
Fe^{3+}	0.732	0.754	0.576	0.337	0.285	0.508	0.514
Mn	0.005	0.006	0.014	0.001	0.000	0.005	0.006
Mg	0.002	0.004	0.003	0.002	0.003	0.000	0.000
Ca	1.939	1.921	1.951	1.966	1.956	1.940	1.949
Na	0.000	0.000	0.000	0.001	0.000	0.000	0.000
OH	1.000	1.000	1.000	1.000	1.000	1.000	1.000
Total	8.989	8.982	9.000	8.989	8.987	8.987	8.990
Fe/(Fe+Al)	0.24	0.25	0.19	0.11	0.09	0.17	0.17

Analysis	22
Sample (KN14-)	50A
SiO$_2$	38.12
TiO$_2$	0.03
Al$_2$O$_3$	26.07
Fe$_2$O$_3$	11.65
MnO	0.05
MgO	0.00
CaO	23.28
Na$_2$O	0.00
H$_2$O	1.91
Total	101.10
Si	2.969
Ti	0.002
Al	2.393
Fe^{3+}	0.683
Mn	0.003
Mg	0.000
Ca	1.943
Na	0.000
OH	1.000
Total	8.992
Fe/(Fe+Al)	0.22
[1]Assuming all Fe is Fe^{3+}	

Table A.8   Garnet Compositions

Analysis	1	2
Location	core	rim
Sample (KN14-)	50A	50A
SiO_2	37.57	37.65
TiO_2	0.02	0.02
Al_2O_3	21.21	21.29
Fe2O3	0.27	0.11
FeO	26.04	26.11
MnO	1.73	1.74
MgO	1.29	1.28
CaO	12.06	11.88
Total	100.19	100.09
Si	2.985	2.991
Ti	0.001	0.001
Al	1.986	1.994
Fe3+	0.016	0.007
Fe2+	1.730	1.735
Mn	0.116	0.117
Mg	0.152	0.152
Ca	1.026	1.012
Total	8.013	8.007
Alm	57.19	57.54
Prp	5.04	5.03
Grs	33.63	33.42
Sps	3.84	3.87
Adr	0.27	0.11

Table A.9   Titanite Compositions

Analysis	1	2	3	4	5	6	7
Sample (KN14-)	18B	18B	20E2	20E2	22B	22B	24A
SiO_2	30.65	30.61	30.49	30.42	31.06	31.00	30.73
TiO_2	32.19	32.20	36.26	36.60	32.47	30.83	33.08
Al_2O_3	4.19	4.20	2.04	1.62	4.73	5.91	3.98
FeO	0.81	0.92	0.56	0.71	0.36	0.33	0.41
MnO	0.00	0.00	0.10	0.01	0.02	0.03	0.03
MgO	0.00	0.01	0.00	0.00	0.00	0.04	0.00
CaO	27.69	27.55	27.62	27.56	28.18	28.27	27.94
Na_2O	0.01	0.00	0.01	0.00	0.00	0.00	0.00
F	1.30	1.34	0.49	0.46	1.53	1.92	1.11
Sub Total	95.52	95.48	97.07	96.92	98.34	98.32	96.17
O=F	-0.55	-0.56	-0.21	-0.19	-0.65	-0.81	-0.47
Total	94.98	94.92	96.86	96.73	97.70	97.51	95.70
Si	1.246	1.254	1.087	1.084	1.296	1.385	1.204
Al	0.201	0.202	0.086	0.068	0.233	0.311	0.184
Ti	0.984	0.992	0.973	0.981	1.019	1.036	0.974
Fe	0.028	0.032	0.016	0.021	0.013	0.012	0.013
Mn	0.000	0.000	0.003	0.000	0.000	0.001	0.001
Mg	0.000	0.001	0.000	0.000	0.000	0.003	0.000
Ca	1.206	1.209	1.055	1.052	1.259	1.353	1.174
F	-0.665	-0.689	-0.220	-0.207	-0.820	-1.101	-0.550
Total	3.000	3.000	3.000	3.000	3.000	3.000	3.000
Ti/(Ti+Al+Fe)	0.81	0.81	0.91	0.92	0.81	0.76	0.83

Analysis Sample (KN14-)	8 24A	9 24A	10 56B	11 56B	12 56B	13 53A	14 53A
SiO_2	30.70	30.69	30.97	30.64	30.83	30.54	30.42
TiO_2	33.17	32.80	31.11	31.88	30.73	36.20	35.70
Al_2O_3	4.06	4.08	5.32	4.85	5.34	1.89	2.29
FeO	0.50	0.50	0.61	0.63	0.93	0.46	0.55
MnO	0.01	0.01	0.03	0.00	0.03	0.06	0.03
MgO	0.00	0.00	0.04	0.02	0.02	0.00	0.00
CaO	27.80	27.83	27.95	27.88	27.94	27.49	27.70
Na_2O	0.00	0.00	0.00	0.00	0.00	0.00	0.00
F	1.25	1.18	1.77	1.66	1.68	0.55	0.73
Sub Total	96.23	95.90	97.79	97.56	97.50	97.18	97.40
O=F	-0.53	-0.50	-0.74	-0.70	-0.71	-0.23	-0.31
Total	95.70	95.40	97.05	96.86	96.79	96.95	97.10
Si	1.231	1.220	1.353	1.320	1.327	1.104	1.127
Al	0.192	0.191	0.274	0.246	0.271	0.080	0.100
Ti	1.000	0.980	1.022	1.033	0.995	0.984	0.995
Fe	0.017	0.017	0.023	0.022	0.034	0.014	0.017
Mn	0.000	0.000	0.001	0.000	0.001	0.002	0.001
Mg	0.000	0.000	0.003	0.001	0.001	0.000	0.000
Ca	1.195	1.185	1.309	1.286	1.288	1.064	1.100
F	-0.636	-0.593	-0.985	-0.908	-0.917	-0.249	-0.340
Total	3.000	3.000	3.000	3.000	3.000	3.000	3.000
Ti/(Ti+Al+Fe)	0.83	0.83	0.78	0.79	0.77	0.91	0.90

Analysis Sample (KN14-)	15 33B	16 33B	17 51A	18 51A	19 51A	20 50A	21 50A
SiO_2	30.38	30.24	30.44	30.28	30.48	30.58	30.69
TiO_2	36.06	35.50	36.79	36.98	36.92	34.91	35.00
Al_2O_3	2.30	2.48	2.11	1.72	2.14	2.97	2.69
FeO	0.17	0.32	0.19	0.15	0.17	0.52	0.62
MnO	0.03	0.00	0.00	0.00	0.00	0.02	0.01
MgO	0.00	0.00	0.00	0.00	0.00	0.00	0.00
CaO	28.54	28.70	28.59	28.16	28.40	28.26	28.28
Na_2O	0.00	0.00	0.01	0.00	0.00	0.00	0.00
F	0.65	0.73	0.46	0.33	0.60	0.75	0.59
Sub Total	98.13	97.96	98.58	97.62	98.71	98.02	97.87
O=F	-0.27	-0.31	-0.19	-0.14	-0.25	-0.32	-0.25
Total	97.86	97.65	98.39	97.48	98.46	97.70	97.62
Si	1.102	1.111	1.068	1.054	1.094	1.126	1.103
Al	0.099	0.107	0.087	0.071	0.090	0.129	0.114
Ti	0.984	0.980	0.971	0.968	0.996	0.966	0.946
Fe	0.005	0.010	0.005	0.004	0.005	0.016	0.018
Mn	0.001	0.000	0.000	0.000	0.000	0.001	0.000
Mg	0.000	0.000	0.000	0.000	0.000	0.000	0.000
Ca	1.109	1.130	1.075	1.050	1.092	1.115	1.089
F	-0.300	-0.338	-0.206	-0.147	-0.277	-0.352	-0.271
Total	3.000	3.000	3.000	3.000	3.000	3.000	3.000
Ti/(Ti+Al+Fe)	0.90	0.89	0.91	0.93	0.91	0.87	0.88

Analysis	22
Sample (KN14-)	50A
SiO$_2$	30.39
TiO$_2$	36.09
Al$_2$O$_3$	2.16
FeO	0.41
MnO	0.00
MgO	0.00
CaO	27.90
Na$_2$O	0.00
F	0.45
Sub Total	97.40
O=F	-0.19
Total	97.21
Si	1.014
Al	0.085
Ti	0.906
Fe	0.011
Mn	0.000
Mg	0.000
Ca	0.998
F	-0.189
Total	3.000
Ti/(Ti+Al+Fe)	0.90

Table A.10   Calcite Compositions

| Analysis | 1 | 2 | 3 | 4 | 5 | 6 | 7 |
Sample (KN14-)	18B	20E2	22B	24A	53A	33B	51A
FeO	0.41	0.75	0.28	0.32	0.25	0.37	0.23
MgO	0.00	0.00	0.00	0.00	0.00	0.00	0.00
CaO	54.13	52.99	54.43	53.00	53.61	53.20	53.67
SrO	0.00	0.00	0.00	0.00	0.00	0.00	0.00
Total	54.54	53.75	54.70	53.32	53.86	53.57	53.89
Fe	0.012	0.022	0.008	0.009	0.007	0.011	0.007
Mg	0.000	0.000	0.000	0.000	0.000	0.000	0.000
Ca	1.988	1.978	1.992	1.991	1.993	1.989	1.993
Sr	0.000	0.000	0.000	0.000	0.000	0.000	0.000
Total	2.000	2.000	2.000	2.000	2.000	2.000	2.000
Cal	99.42	98.90	99.60	99.53	99.63	99.47	99.67

| Analysis | 8 |
Sample (KN14-)	50A
FeO	0.43
MgO	0.00
CaO	53.51
SrO	0.00
Total	53.94
Fe	0.012
Mg	0.000
Ca	1.988
Sr	0.000
Total	2.000
Cal	99.38

Table A.11   EPMA Standards

Mineral Analyzed	F	Na	Mg	Al	Si	Cl
Epidote	Apatite	Jadeite	MgO	Augite	Augite	
Feldspar		Jadeite		Garnet	Wollastonite	
Garnet			Garnet	Garnet	Garnet	
Ca-Amphibole	Apatite	Jadeite	MgO	Labradorite	Wollastonite	Scapolite
Mica	Apatite	Jadeite	Garnet	Garnet	Wollastonite	Scapolite
Clinopyroxene		Jadeite	MgO	Garnet	Wollastonite	
Calcite			Dolomite			
Titanite	Apatite	Jadeite	Garnet	Garnet	Wollastonite	

Mineral Analyzed	K	Ca	Ti	Mn	Fe	Sr
Epidote		Wollastonite	Titanite	Spessartine	Biotite	
Feldspar	Orthoclase	Wollastonite			Garnet	
Garnet		Wollastonite	Titanite	Spessartine	Garnet	
Ca-Amphibole	Orthoclase	Labradorite	Titanite	Spessartine	Biotite	
Mica	Orthoclase	Anorthite	Titanite	Spessartine	Biotite	
Clinopyroxene		Wollastonite	Titanite	Spessartine	Biotite	
Calcite		Calcite			Siderite	Strontianite
Titanite		Anorthite	Ilmenite	Spessartine	Biotite	

APPENDIX B

Detailed Petrography

KN14-18b

The structurally lowest sample KN14-18b is granoblastic with weak banding of diopside and calcite. Diopside ($Mg/(Mg+Fe) = 0.52$-0.62) forms rounded $\leq 4mm$ grains. In one location diopside grows into hornblende ($Mg/(Mg+Fe^{2+}) = 0.45$-0.47). Epidote ($Fe/(Fe+Al) = 0.18$-0.21) occurs as symplectic masses with quartz and rims over allanite. Scapolite (Me_{60}) is often rimmed by plagioclase. Small $\sim 100\ \mu m$ rounded grains of plagioclase (An_{24-27}) not in contact with scapolite also occur. Alkali feldspar ($Or_{\sim93}$), calcite, and quartz are other common matrix phases. Titanite is the most common accessory phase and exhibits lenticular habits. Zoning in backscattered electron imaging (BSEI) ranges from patchy to weak oscillatory. Other accessory minerals are zircon, apatite, and allanite.

KN14-20E2

Sample KN14-20E2 is gneissic with 1mm to 1 cm thick alternating bands of quartz and aligned hornblende grains. Hornblende ($Mg/(Mg+Fe^{2+}) = 0.46$-0.48) has minor zoning in Fe-Mg and ranges in size from 10 μm to 1 cm. Large optically continuous biotite grains ($Fe/(Mg+Fe) = 0.3$) are often intersected by or contain hornblende. Epidote ($Fe/(Fe+Al) = 0.25$-0.26) occurs as symplectic masses with quartz, overgrowths on allanite, or as thin lenses following grain boundaries. Rare scapolite (Me_{64}) forms small unzoned grains. Plagioclase exhibits a wide range of compositions (An_{28-41}) with patchy low An zones, that occur next to calcite and epidote. Alkali feldspar (Or_{90}) forms irregular grains with peninsular growths encroaching into plagioclase and quartz. Quartz appears as rounded matrix grains, elongate bands, and in symplectites with plagioclase, biotite, and epidote. Calcite forms small lenses following grain boundaries.

Titanite is the most common accessory phase. The largest grains (4-5 mm) are wedge shaped and completely unzoned in BSEI, while more common small lobate masses show patchy zoning. Light zones in BSEI have increased Ti + Fe and decreased Al. Other accessory phases include allanite, apatite, and zircon.

<u>KN14-22b</u>

Sample KN14-22b is a granoblastic calc-silicate. Diopside (Mg/(Mg+Fe) = 0.69) occurs as 0.2-5 mm unzoned and rounded grains. Rare actinolite (Mg/(Mg+Fe^{2+}) = 0.7) appears as a single bladed inclusion in diopside and in the matrix adjacent to diopside grains. Epidote (Fe/(Al+Fe) = 0.10) forms symplectic masses with quartz and calcite. Scapolite (Me$_{74}$) occurs as inclusion poor xenoblastic grains, often rimmed by plagioclase (An$_{66}$). Anorthite content decreases with distance from scapolite and in one case transitions into a symplectite of low-An plagioclase and quartz. Plagioclase (An$_{40-66}$) also appears as small rounded grains that display albite twinning. Alkali feldspar forms large rounded grains with slight core (Or$_{91}$) to rim (Or$_{93}$) zoning. Quartz is uncommon, occurring only in symplectites or small lobate grains. Calcite occurs both in the matrix and as inclusions in epidote and scapolite. Titanite (≤ 2 mm) is the most common accessory mineral. Most grains have an overall wedge habit; however, some faces are irregular and feature large grain boundary filling peninsulas. Zoning in BSEI is irregular and patchy, some bright zones are visible reflected light. Other accessory phases include allanite and zircon.

<u>KN14-24A</u>

Sample KN14-24A is granoblastic with weakly lineated of diopside. Diopside (Mg/(Mg+Fe) = 0.56-0.59) occurs as 0.1-5 mm rounded and irregular grains with weak

patchy zoning visible in BSEI. Inclusion rich grains contain scapolite, calcite, and titanite. Irregular grains intersect along boundaries from multiple nucleation points. A single amphibole grain with an actinolite core ($Mg/(Mg+Fe^{2+}) = 0.7$) and ferrohornblende rim ($Mg/(Mg+Fe^{2+}) = 0.45$) was found. Epidote ($Fe/(Fe+Al) = 0.14$-0.18) appear as 0.3-0.5 mm diameter homogenous grains or as thin lenses following grain boundaries. The large grains display weak symplectic textures with quartz. Grain boundary lenses of epidote occur adjacent to scapolite and calcite, while the large grains contain scapolite and calcite inclusions. Scapolite (Me_{75}) occurs as large (~ 0.5 mm) rounded grains. Plagioclase (An_{92-96}) appears as large unzoned grains and less commonly as rims around scapolite with An content decreasing inward. Quartz occurs as thin lenses around grain boundaries or as inclusions in epidote. Calcite forms large coherent grains, small fracture/grain boundary filling lenses, and inclusions in plagioclase and diopside. Titanite is the most common accessory phase, forming medium to small lenticular or stubby grains. Larger 2-5 mm grains have irregular and lobate habits. While some grains are completely unzoned, others show both light-to-dark or dark-to-light core to rim zoning. The dark zones are slightly lower in Ti; however, Al and Fe remain unchanged. Other accessory phases include allanite, apatite, and zircon.

KN14-56b

Sample KN14-56b is a gneiss with oriented biotite and large $\leq$ 5 mm hornblende. The sample is dominated by hornblende ($Mg/(Mg+Fe^{2+}) = 0.47$) which contain inclusions of titanite, biotite, and quartz. Hornblende rims are 0.2 mole higher in Si. Biotite ($Fe/(Mg+Fe) = 0.44$) is a common matrix mineral and often contains inclusions of titanite. Epidote ($Fe/(Fe+Al) = 0.20$-0.21) is uncommon, only occurring as small $\leq$0.1

mm irregularly shaped grains forming around allanite or amphibole. There are two types of plagioclase; large xenoblastic grains (An_{33-36}), which show patchy low An zones along rims in contact with quartz and alkali feldspar, and symplectites with quartz (An_{26}). Alkali feldspar (Or_{89-92}) consists of large xenoblastic grains with minor perthitic textures. Quartz commonly occurs as rounded grains in the matrix. Titanite is the most common accessory phase and either shows oscillatory light core to dark rim zoning or no zoning in BSEI. Light cores have ~0.2 mol lower Al than dark rims. Allanite and zircon are the other accessory phases.

KN14-53A

KN14-53A is a gneiss with fine compositional banding, leading to considerable heterogeneity in mineral abundances (table 1). The sample has 0.2-1.5 cm wide Bt + Qtz + Pl + Tur rich psammitic bands, a 2 mm thick band of actinolite, and 2-3 mm thick bands of Cal + Qtz. The majority of the sample is Di + Qtz + Pl + Kfs + Cal + Ttn ± Ep. Diopside (Mg/(Mg+Fe) = 0.75-0.78) forms blocky grains partially or wholly rimmed by actinolite. Actinolite ($Mg/(Mg+Fe^{2+})$ = 0.77-0.78) occurs as overgrowths of diopside or as ≤2 mm long blades. Bladed actinolite display dark rims with higher K and Al. Epidote (Fe/(Fe+Al) = 0.19-0.25) forms overgrowths of allanite or lenses between grain boundaries commonly adjacent to plagioclase. Biotite (Fe/(Fe+Mg) = 0.27) appears as oriented grains (≤ 0.5 mm long) in actinolite poor regions. Plagioclase (An_{66-82}) forms blocky grains with patchy zoning in BSE. Alkali feldspar (Or_{94-96}) is found as rounded grains or as irregular rims on plagioclase. Quartz occurs as rounded grains and along with calcite and plagioclase makes up the majority of the sample. Calcite appears as large xenoblastic grains. Titanite is the most common accessory phase and occurs as blocky or

oriented lenticular grains. Zoning is patchy, erratic, and sometimes non-existant. In some of the largest grains, the zones are polygonal with well-defined boarders. The light core analyzed is only ~ 0.01 mol higher in Ti than the dark rim. Allanite occurs as cores in epidote. Apatite, zircon, and tourmaline are other accessory phases.

KN14-33B

KN14-33B is a calc-silicate gneiss with aligned biotite, diopside, and actinolite. Diopside ($Mg/(Mg+Fe)$ = 0.73-0.78) is commonly xenoblastic and overgrown by actinolite. Scapolite and calcite are commonly included in the large (~ 2mm) poikioblastic grains. Actinolite ($Mg/(Mg+Fe^{2+})$ = 0.74-0.77) forms irregular grains with occasional quasi-symplectic textures with quartz. Zoning is patchy and coincides with changes in Al, Fe, and A site occupancy. Epidote ($Fe/(Fe+Al)$ = 0.09-0.11) forms rims over allanite or symplectites with quartz. Oriented biotite ($Fe/(Fe+Mg)$ = 0.25) occurs in 3-10 mm thick patches and defines the overall foliation. Scapolite (Me_{71}) and alkali feldspar (Or_{93}) form rounded grains ranging in size from 50 to 400 µm. Plagioclase (An_{36-65}) occurs as small (50-80 µm) rounded grains. Quartz occurs as irregular to rounded grains with inclusions of scapolite, alkali feldspar, calcite, and actinolite. Xenoblastic calcite is the most common matrix phase, making up a larger proportion of the sample compared to the others considered. Titanite is the most common accessory phase, forming blocky and irregular grains. Zoning in BSE is weak to non-existent. Other accessory phases include allanite, tourmaline, apatite, and zircon.

KN14-51A

Sample KN14-51A is medium grained with sparse poikiloblasts of diopside. Diopside ($Mg/(Mg+Fe)$ = 0.90) occur as 1-7 mm wide irregular colorless grains with

inclusions of quartz, calcite, and biotite. Actinolite ($Mg/(Mg+Fe^{2+}) = 0.85$) and calcite form reaction rims over diopside. Plagioclase (An_{98}) and alkali feldspar (Or_{96-97}) appear as semi-rounded unzoned grains. Quartz is found as rounded and irregular grains in the matrix and as inclusions in alkali-feldspar, titanite, and diopside. Titanite occurs as wedge to irregularly shaped grains with patchy polygonal zones, and rare quasi-oscillatory zoning driven by variations in Ti content. Zircon is also present as an accessory phase.

KN14-50A

Sample KN14-50A is a biotite rich calc-schist with coarse grained calcite-poor hornblende-rich dilatational fractures oriented ~30 ° to the major foliation. Hornblende ($Mg/(Mg+Fe^{2+}) = 0.37-0.38$) occurs as 1-3 mm wide piokiloblastic grains. These grains are inclusion rich (~50 vol % inclusions) with oval-shaped (100-150 µm wide) quartz and scapolite. The dilatational fractures also contain rare ~ 1 mm diameter garnet ($Grs_{34}Alm_{57}Prp_5Sps_4$). Biotite ($Fe/(Fe+Mg) = 0.64-0.65$) forms the majority of the sample, except in hornblende rich zones. Epidote ($Fe/(Fe+Al) = 0.17-0.22$) occurs as overgrowths of allanite adjacent to scapolite and plagioclase. Scapolite (Me_{76}) occurs throughout the sample as rounded grains. Plagioclase (An_{46-60}) occurs as weakly zoned grains, symplectites with quartz, and as rims overgrowing scapolite. Alkali feldspar (Or_{90}) occurs as rounded and xenoblastic grains in the matrix. Some alkali feldspar grains show zoning in BSEI with Ba rich rims. Quartz is abundant throughout the matrix, occurring as symplectites with biotite and plagioclase and as inclusions in garnet and hornblende. Titanite occurs as large 0.5 mm irregularly shaped grains with peninsulas growing around other matrix phases. Zoning is patchy, irregular, or non-existent. Where

zoning does occur it is driven by changing Ti content. Allanite and zircon are other common accessory phases.

APPENDIX C

LA-ICP-MS Analysis Locations
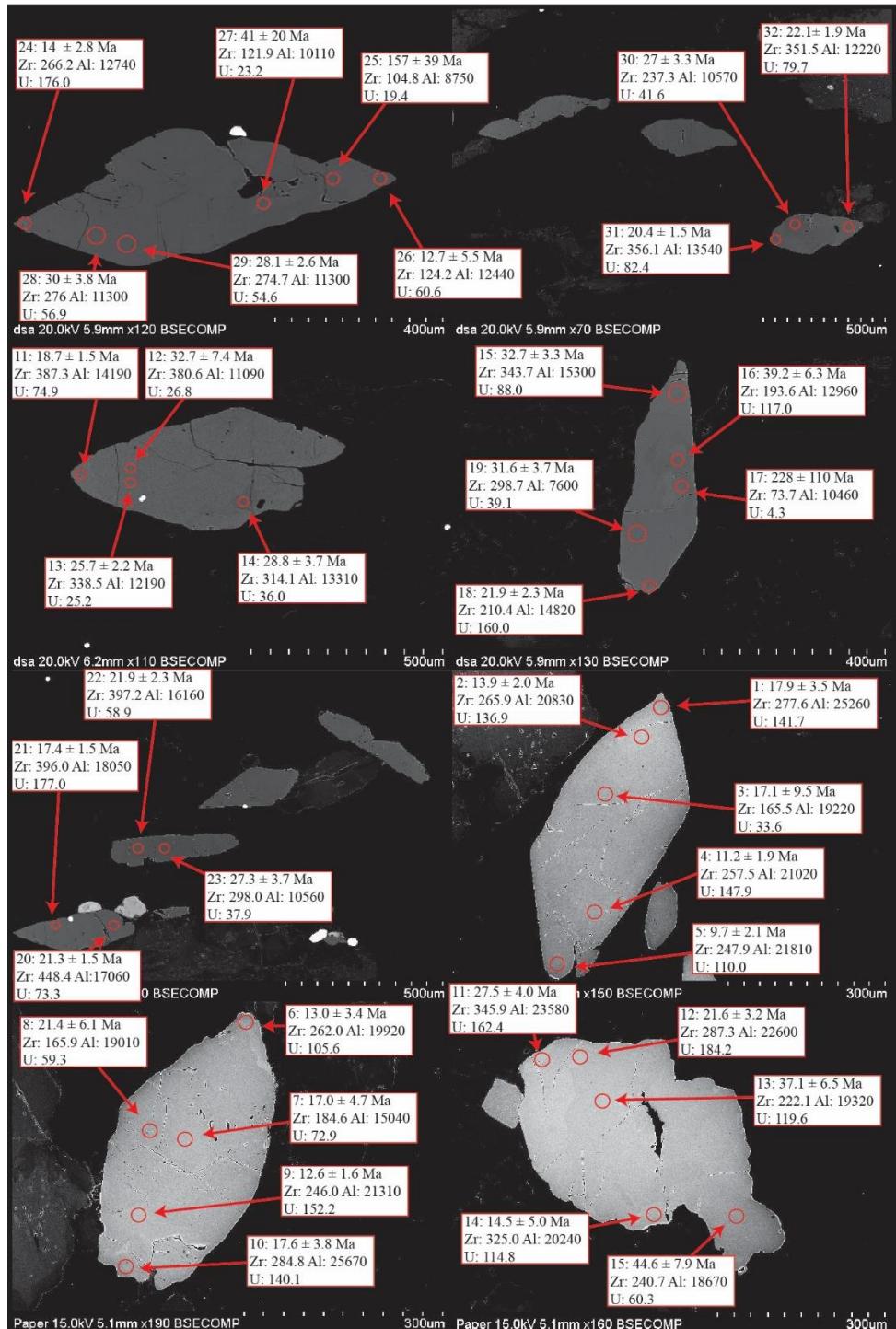
Figure C.1.   LA-ICP-MS sample locations for KN14-18B
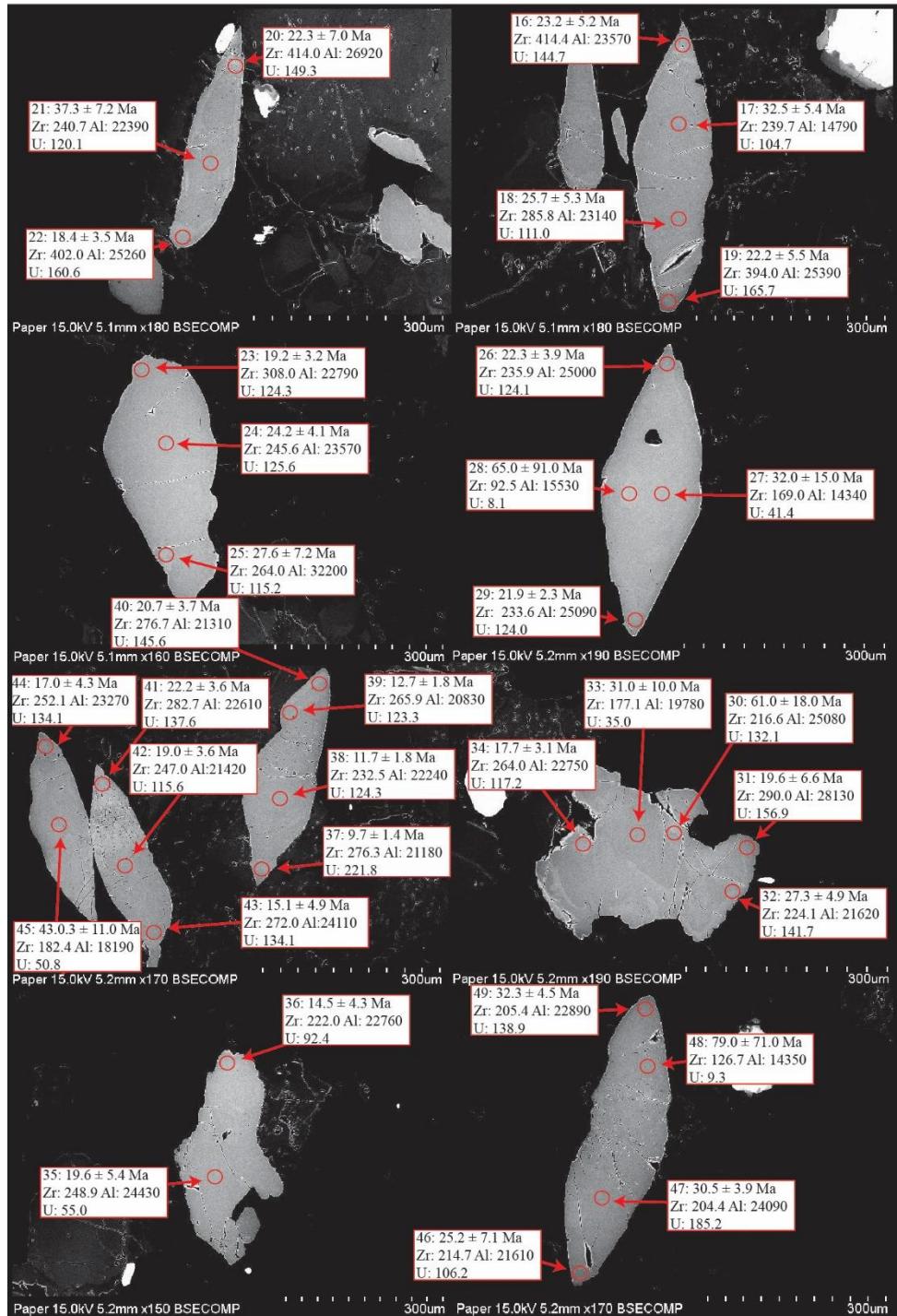
Figure C.2.   LA-ICP-MS sample locations for KN14-18B.

Figure C.3.   LA-ICP-MS sample locations for KN14-20E2.
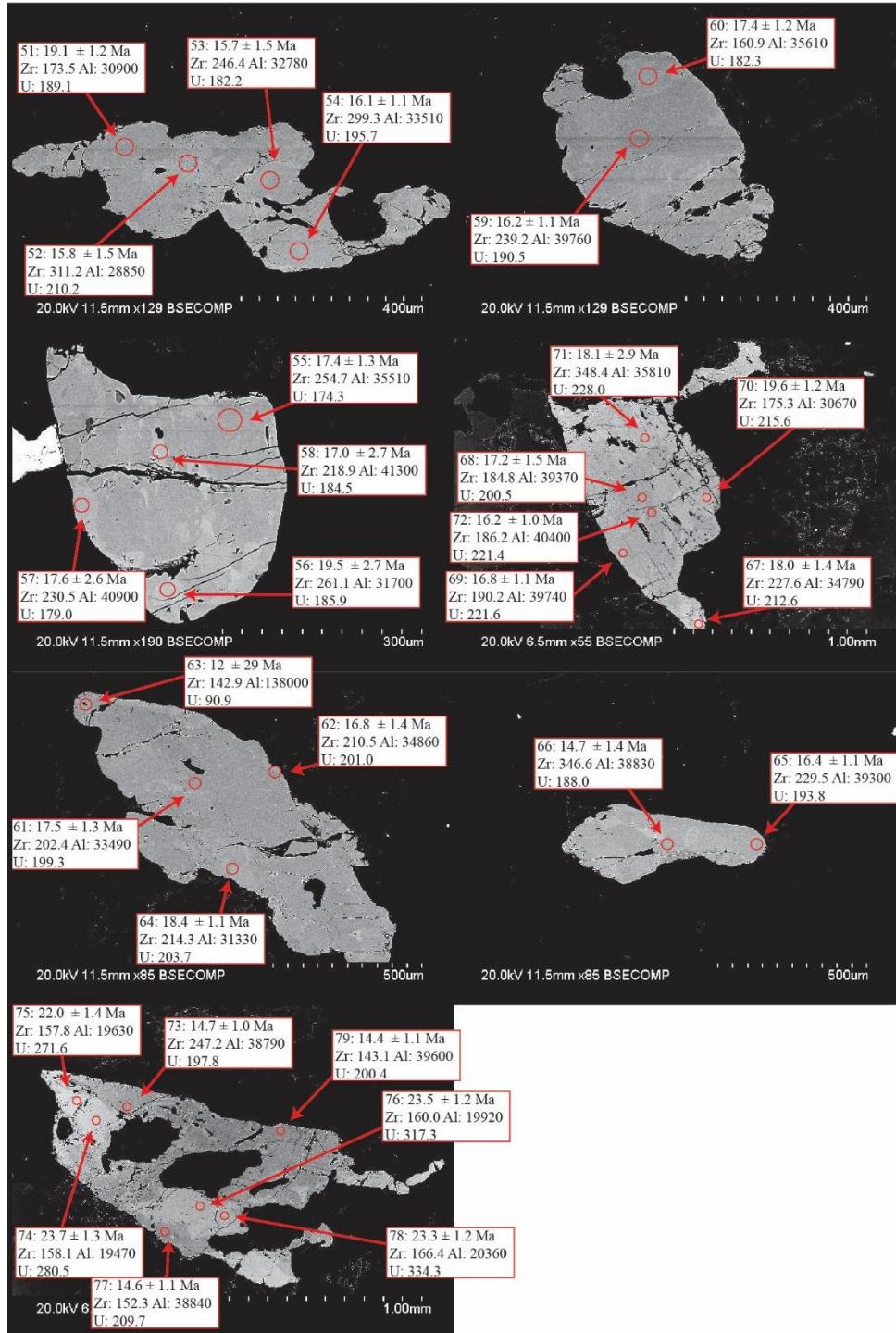
Figure C.3.   LA-ICP-MS sample locations for KN14-22B.

Figure C.4.   LA-ICP-MS sample locations for KN14-24A.
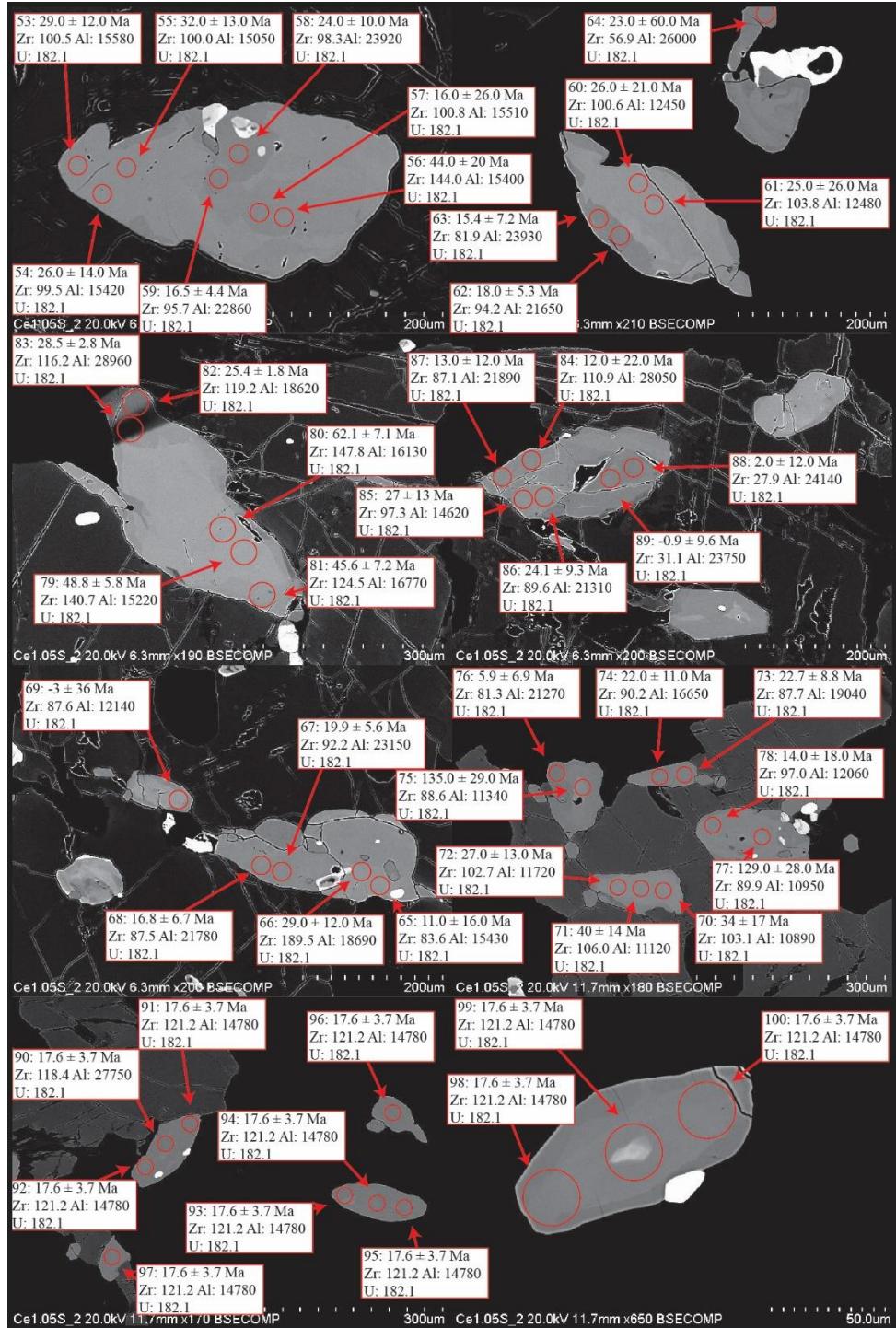
Figure C.5.   LA-ICP-MS sample locations for KN14-56B.
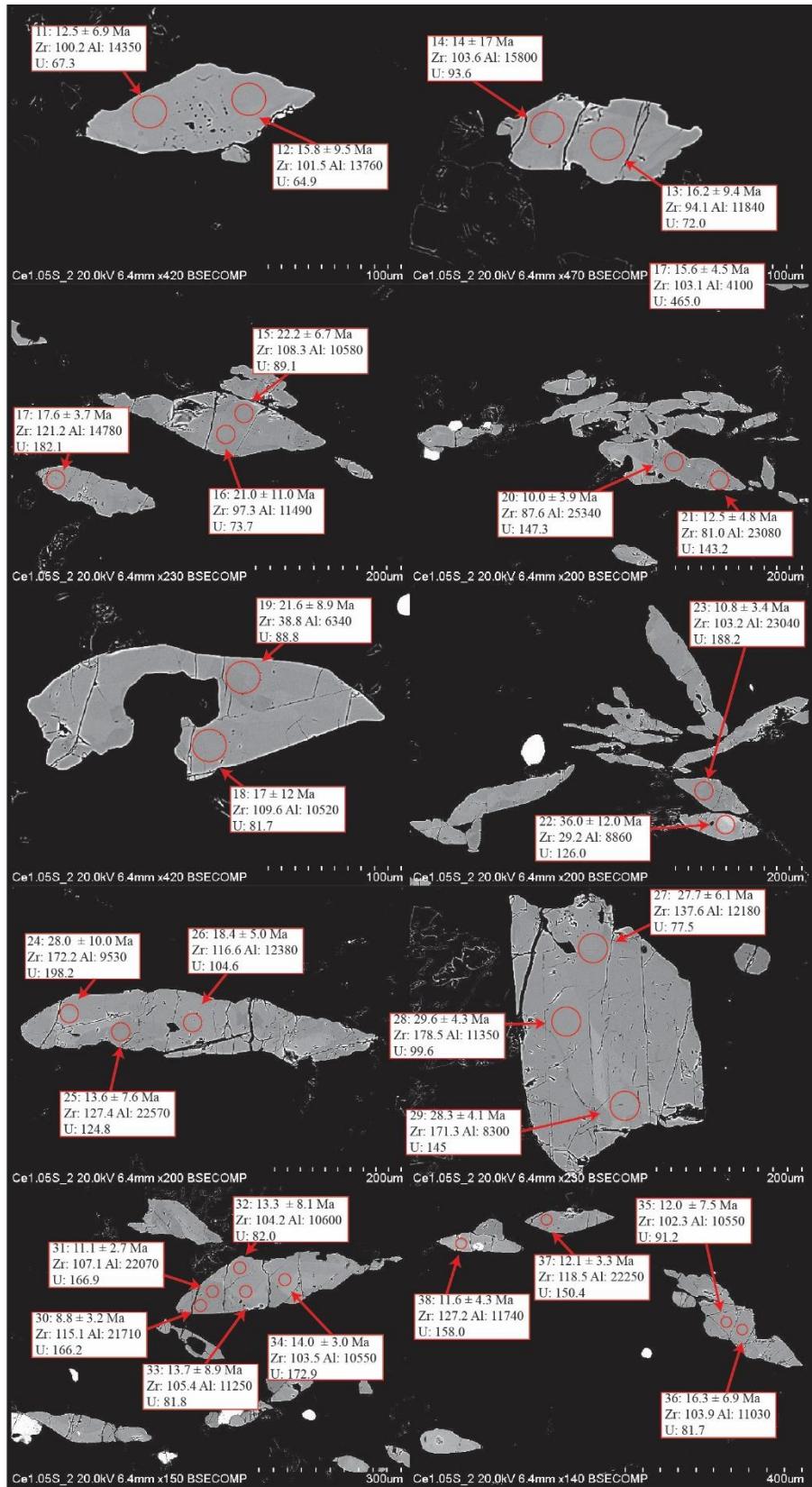
Figure C.6. **LA-ICP-MS sample locations for KN14-53A.**
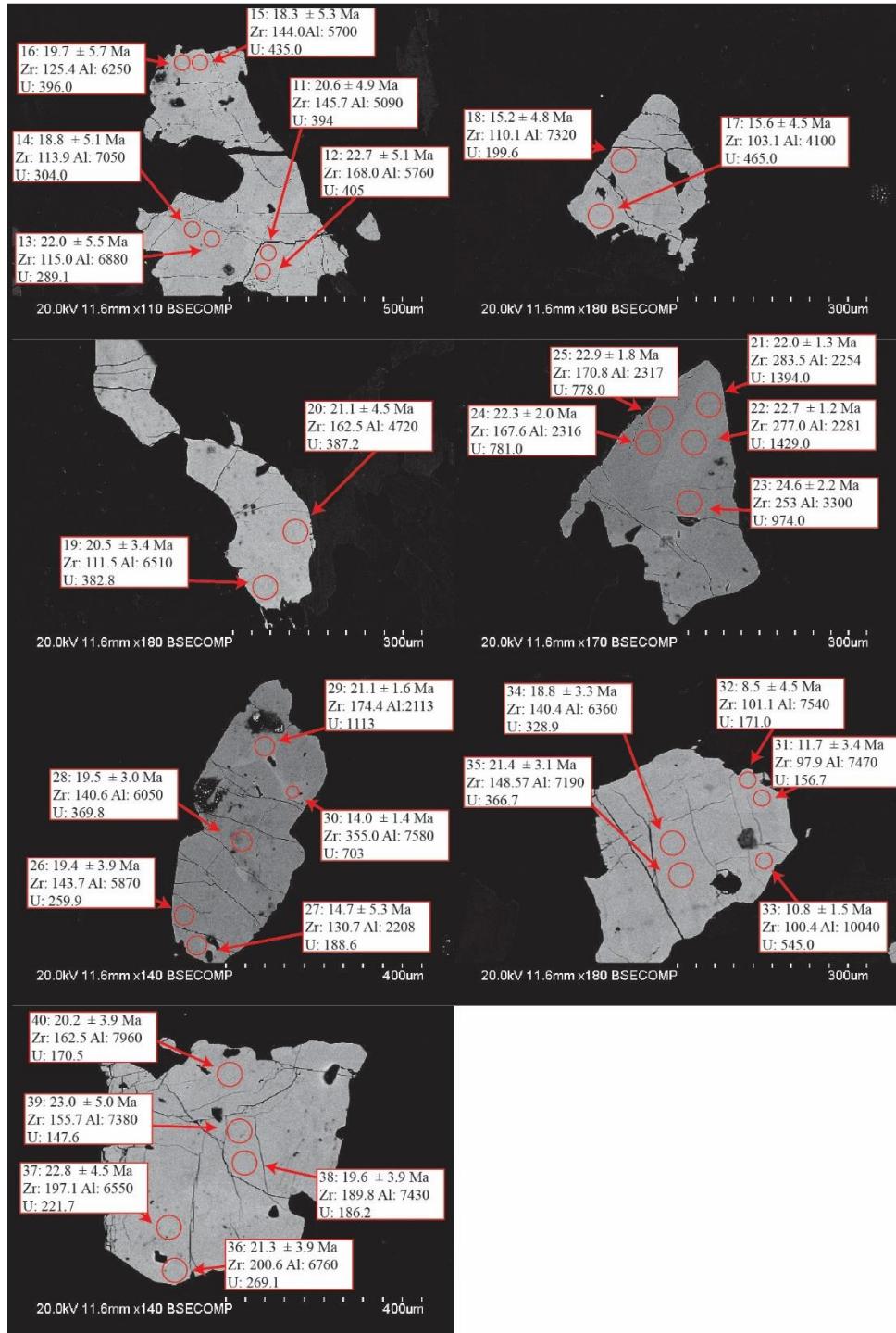
Figure C.7.   LA-ICP-MS sample locations for KN14-33B.
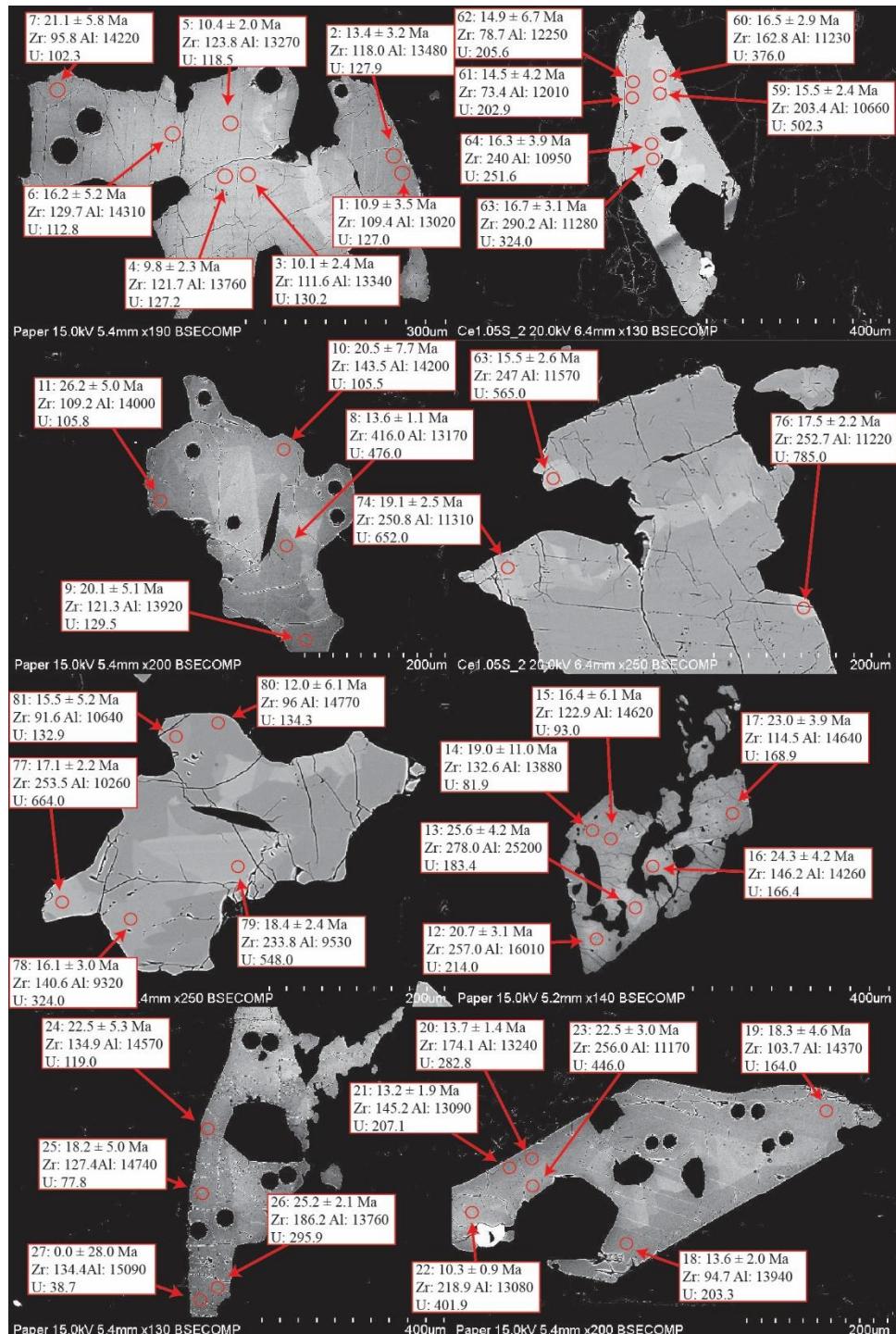
Figure C.8.   LA-ICP-MS sample locations for KN14-51A.

Figure C.9.   LA-ICP-MS sample locations for KN14-50A.

APPENDIX D

LA-ICP-MS Data

Table D.1   LA-ICP-MS Data for KN14-18B

Analysis	Spot Size (µm)	Al (ppm)	2σ	Zr (ppm)	2σ	T (°C)[1]	2σ	U (ppm)	2σ	^{238}U/^{206}Pb	2σ	^{207}Pb/^{206}Pb	2σ	Rho	Age (Ma)[2]	2σ
11	40	14190	330	387.3	9.3	848	13	74.9	2.1	185.5	6.2	0.4780	0.0270	0.6	18.7	1.5
12	40	11090	470	380.6	8.6	847	13	26.8	0.7	30.8	1.2	0.8340	0.0290	0.3	32.7	7.4
13	40	12190	340	338.5	7.1	839	13	25.2	0.5	39.0	1.4	0.8270	0.0260	0.1	27.1	5.1
14	40	13310	290	314.1	6.1	835	13	36.0	1.3	57.5	1.8	0.7400	0.0260	0.4	28.8	3.7
15	40	15330	420	343.7	6.4	840	13	88.0	1.6	64.1	7.4	0.6760	0.0320	-0.6	32.7	3.3
16	25	12960	390	193.6	8.0	805	13	117.0	12.0	77.5	13.2	0.5390	0.0460	-0.4	39.2	6.3
17	25	10460	170	73.7	2.3	751	12	4.3	0.2	3.3	0.2	0.8700	0.0500	0.6	228	110
18	25	14820	240	210.4	4.6	810	13	160.0	3.5	161.0	7.5	0.4680	0.0370	0.5	21.9	2.3
19	40	7600	400	298.7	6.2	832	13	39.1	1.4	63.7	3.0	0.6880	0.0290	0.1	31.6	3.7
20	40	17060	330	448.4	7.9	857	13	73.3	1.6	163.1	5.3	0.4750	0.0260	0.3	21.3	1.5
21	25	18050	330	396.0	11.0	849	13	177.0	3.8	316.5	18.0	0.1830	0.0330	0.5	17.4	1.5
22	40	16160	340	397.2	8.5	849	13	58.9	1.1	112.7	6.7	0.6220	0.0300	0.0	21.9	2.3
23	40	10560	480	298.0	5.9	831	13	37.9	1.9	66.1	2.1	0.7180	0.0290	0.5	27.3	3.7
24	25	12740	390	266.2	9.3	825	13	176.0	8.8	281.7	28.6	0.4090	0.0680	0.7	14	2.8
25	25	8750	160	104.8	3.0	770	12	19.4	0.5	5.3	0.3	0.8580	0.0270	0.1	157	39
26	25	12440	260	124.2	3.9	780	12	60.6	1.3	190.8	22.2	0.6300	0.1200	0.8	12.7	5.5
27	25	10110	220	121.9	4.2	779	12	23.2	1.0	30.2	2.3	0.8000	0.0770	0.7	41	20
28	40	12530	510	276.0	7.0	827	13	56.9	1.0	53.5	3.1	0.7470	0.0260	-0.1	30	3.8
29	40	11350	510	274.7	5.9	826	13	54.6	1.2	95.1	2.8	0.5920	0.0290	0.5	28.1	2.6
30	40	10570	510	237.3	4.8	818	13	41.6	0.7	71.6	1.9	0.6990	0.0290	0.5	27	3.3
31	40	13540	430	356.1	6.8	843	13	82.4	2.0	165.0	6.5	0.4920	0.0260	0.3	20.4	1.5
32	40	12220	550	351.5	7.9	842	13	79.7	1.9	133.0	5.1	0.5540	0.0280	0.3	22.1	1.9

Analysis	Spot Size (µm)	Al (ppm)	2σ	Zr (ppm)	2σ	T (°C)[1]	2σ	U (ppm)	2σ	^{238}U/^{206}Pb	2σ	^{207}Pb/^{206}Pb	2σ	Rho	Age (Ma)[2]	2σ
1	25	25260	490	277.6	9.2	827	11	141.7	3.8	192.3	15.2	0.4810	0.0660	0.8	17.9	3.5
2	25	20830	380	265.9	8.0	824	11	136.9	4.1	246.9	15.9	0.4810	0.0550	0.4	13.9	2.0
5	25	21810	390	247.9	7.1	820	11	110.0	2.2	293.3	22.4	0.5660	0.0680	0.7	9.7	2.1
6	25	19920	480	262.0	12.0	824	12	105.6	3.7	159.7	14.3	0.6790	0.0680	0.3	13.0	3.4
7	25	15040	280	184.6	5.7	803	11	72.9	2.0	99.4	8.9	0.7350	0.0590	0.2	17.0	4.7
8	25	19010	410	165.9	4.8	796	11	59.3	1.8	83.3	5.7	0.7220	0.0620	0.6	21.4	6.1
9	25	21310	330	246.0	7.0	820	11	152.2	3.2	292.4	16.2	0.4460	0.0510	0.4	12.6	1.6
10	25	25670	450	284.8	8.8	829	11	140.1	3.4	120.5	16.0	0.6730	0.0450	0.2	17.6	3.8
11	25	23580	460	345.9	8.3	841	11	162.4	2.9	105.7	7.5	0.5580	0.0470	0.3	27.5	4.0
12	25	22600	250	287.3	8.8	829	11	184.2	7.0	138.7	8.5	0.5460	0.0480	0.5	21.6	3.2
13	25	19320	370	222.1	5.7	814	11	119.6	3.6	103.8	10.0	0.4200	0.0620	0.5	37.1	6.5
14	25	20240	370	325.0	9.0	837	11	114.8	2.0	237.5	23.1	0.4800	0.1300	0.9	14.5	5.0
15	25	18670	550	240.7	4.8	818	11	60.3	2.3	64.9	5.1	0.5590	0.0580	0.4	44.6	7.9
16	25	23570	660	414.4	9.9	852	11	144.7	2.4	95.1	6.0	0.6600	0.0570	0.7	23.2	5.2
17	25	14790	250	239.7	5.8	818	11	104.7	2.2	84.1	5.0	0.5830	0.0500	0.6	32.5	5.4
18	25	23140	430	285.8	7.0	829	11	111.0	4.4	114.7	7.9	0.5520	0.0650	0.8	25.7	5.3
19	25	25390	500	394.0	12.0	849	11	165.7	2.7	180.8	15.4	0.3980	0.0600	0.4	22.2	3.4
20	25	26920	450	414.0	17.0	852	12	149.3	6.6	71.9	5.7	0.7370	0.0620	0.5	22.3	7.0
21	25	22390	710	240.7	7.7	818	11	120.1	4.3	49.5	3.7	0.7120	0.0460	0.1	37.3	7.2
22	25	25260	340	402.0	12.0	850	11	160.6	5.0	218.8	17.2	0.3960	0.0690	0.9	18.4	3.5
23	25	22790	540	308.0	14.0	834	12	124.3	4.0	198.0	25.5	0.4300	0.0760	-0.2	19.2	3.2
24	25	23570	400	245.6	6.2	820	11	125.6	2.1	130.0	7.8	0.5240	0.0580	0.7	24.2	4.1
25	25	32200	1100	264.0	18.0	824	13	115.2	4.2	67.1	8.1	0.7110	0.0560	0.2	27.6	7.2
26	25	25000	530	235.9	6.0	817	11	124.1	3.2	124.4	9.6	0.5770	0.0540	0.3	22.3	3.9
27	25	14340	310	169.0	5.1	798	11	41.1	3.7	36.9	3.9	0.8090	0.0730	0.3	32.0	15.0
28	25	15530	290	92.5	3.6	764	11	8.1	0.6	9.5	1.2	0.8900	0.1200	0.7	65.0	91.0
29	25	25090	390	233.6	5.5	817	11	124.0	3.2	128.0	9.8	0.5730	0.0720	0.9	21.9	5.3
30	25	25080	850	216.6	9.9	812	12	132.1	8.1	27.2	5.8	0.7410	0.0810	-0.5	61.0	18.0
31	25	28130	660	290.0	13.0	830	12	156.9	6.4	125.8	13.4	0.6230	0.0950	0.6	19.6	6.6
32	25	21620	510	224.1	6.5	814	11	141.7	3.9	98.8	6.6	0.5890	0.0560	0.4	27.3	4.9

Analysis	Spot Size (µm)	Al (ppm)	2σ	Zr (ppm)	2σ	T (°C)[1]	2σ	U (ppm)	2σ	^{238}U/^{206}Pb	2σ	^{207}Pb/^{206}Pb	2σ	Rho	Age (Ma)[2]	2σ
33	25	19780	360	177.1	4.6	800	10	35.0	0.9	57.1	6.2	0.7240	0.0700	0.4	31.0	10.0
34	25	22750	350	264.0	12.0	824	12	117.2	5.5	188.3	14.2	0.4970	0.0650	0.4	17.7	3.1
35	25	24430	400	248.9	6.0	820	11	55.0	1.3	120.9	7.6	0.6360	0.0780	0.8	19.6	5.4
36	25	22760	540	222.0	13.0	814	12	92.4	6.0	169.5	31.6	0.6230	0.0700	0.2	14.5	4.3
37	25	21180	390	276.3	7.3	827	11	221.8	4.4	315.5	19.9	0.5370	0.0490	0.4	9.7	1.4
38	25	22240	360	232.5	6.4	816	11	124.3	3.2	265.3	14.8	0.5290	0.0510	0.7	11.7	1.8
39	25	23330	360	254.7	7.2	822	11	123.3	2.7	262.5	20.0	0.4970	0.0470	0.3	12.7	1.8
40	25	21310	440	276.7	7.5	827	11	145.6	4.7	168.9	12.3	0.4720	0.0620	0.7	20.7	3.7
41	25	22610	390	282.7	5.8	828	11	137.6	2.7	109.8	8.2	0.6270	0.0430	0.4	22.2	3.6
42	25	21420	300	247.0	6.7	820	11	115.6	2.1	124.1	7.1	0.6390	0.0500	0.7	19.0	3.6
43	25	24110	690	272.0	11.0	826	11	134.1	5.6	186.9	18.2	0.5700	0.1000	0.8	15.1	4.9
44	25	23270	350	252.1	8.9	821	11	128.1	4.6	157.5	16.9	0.5910	0.0660	0.7	17.0	4.3
45	25	18190	310	182.4	5.6	802	11	50.8	1.2	39.7	3.5	0.7340	0.0520	0.4	43.0	11.0
46	25	21610	400	214.7	7.4	812	11	106.2	3.6	100.5	9.1	0.6130	0.0750	0.9	25.2	7.1
47	25	24090	420	204.4	6.2	809	11	185.2	3.2	108.6	8.7	0.5000	0.0430	0.2	30.5	3.9
48	25	14350	280	126.7	3.8	781	10	9.3	0.7	11.4	1.4	0.8500	0.1100	0.5	79.0	71.0
49	25	22890	420	205.4	5.3	809	11	138.9	3.3	82.6	6.8	0.5930	0.0440	0.0	32.3	4.5

[1]Calculated at 11.9 kbar,
[2]Initial ^{207}Pb/^{206}Pb = 0.9810± 0.0352 2σ

Table D.2   LA-ICP-MS data for KN14-20E2

Analysis	Spot Size (µm)	Al (ppm)	2σ	Zr (ppm)	2σ	T (°C)[1]	2σ	U (ppm)	2σ	^{238}U/^{206}Pb	2σ	^{207}Pb/^{206}Pb	2σ	Rho	Age (Ma)[2]	2σ
11	40	10370	140	134.5	1.7	768	12	19.7	0.3	10.6	0.2	0.8200	0.0120	0.3	25.5	9.7
12	40	10490	140	133.1	1.9	767	12	19.2	0.3	19.8	0.3	0.7930	0.0160	0.6	24.5	6.8
13	40	12670	190	130.4	1.9	766	12	18.2	0.3	19.85	0.3	0.7930	0.0170	0.6	24.6	7.2
14	40	10110	160	180	2.4	784	12	164.5	2.1	104.4	1.5	0.5610	0.0093	0.5	22.4	0.9
15	40	5820	110	231.8	4	799	13	393.2	6.3	233.4	4.8	0.3360	0.0130	0.2	17.7	0.6
16	40	5840	100	226.2	3.5	797	12	443.9	6.5	243.8	4.9	0.3180	0.0120	0.4	17.5	0.6
17	40	6110	94	208.1	3.9	792	12	428.1	5.7	221.5	4.3	0.3140	0.0130	0.4	19.4	0.7
18	40	6440	110	224.7	4	797	12	384.8	6.0	225.3	4.2	0.3330	0.0120	0.4	18.4	0.5
19	40	6990	120	232.5	4.4	799	13	193.1	3.8	38.0	6.2	0.6770	0.0270	-0.8	37.1	3.9
20	40	8260	330	214.4	4.2	794	12	210.5	4.5	138.3	4.2	0.4260	0.0170	0.4	24.7	1.4
21	40	8700	450	215.9	4.5	795	13	189.1	4.7	128.5	3.8	0.4540	0.0220	0.6	24.8	1.9
22	40	7960	180	219.8	4	796	12	258.2	7.5	116.3	13.5	0.4380	0.0240	-0.7	28.5	2.4
23	40	7890	140	199.9	3.2	790	12	15.8	0.2	7.0	0.6	0.8360	0.0210	0.1	20.0	24.0
24	40	7780	180	196.2	3.6	789	12	15.6	0.3	11.3	0.8	0.8250	0.0260	0.1	20.0	19.0
25	40	8110	230	211.1	3.7	793	12	26.2	0.4	24.0	0.5	0.7670	0.0250	0.6	28.9	8.6
26	40	7630	180	196.3	3.3	789	12	22.7	0.3	22.2	0.6	0.7880	0.0270	0.6	24.0	10.0
27	40	5670	150	155.6	4	776	12	213.5	5.1	120.6	13.8	0.5480	0.0290	-0.6	20.2	1.9
28	40	6350	120	209.8	3.9	793	12	323.4	5.6	222.6	4.5	0.3860	0.0130	0.4	16.8	0.7
29	40	6397	98	228.2	4.3	798	13	216.7	3.7	80.4	1.4	0.6650	0.0150	0.5	18.7	1.7
30	40	8310	330	175.5	3.9	783	12	30.1	1.7	29.9	1.3	0.7070	0.0290	0.2	39.2	8.1
31	40	6980	130	198.7	3.7	790	12	72.5	1.1	64.2	2.0	0.6400	0.0210	0.5	26.6	3.1
32	40	7080	160	183.5	3.2	785	12	43.9	1.4	46.6	1.4	0.6950	0.0270	0.6	27.2	5.1

[1]Calculated at 10.2 kbar

[2]Initial ^{207}Pb/^{206}Pb = 0.8538 ± 0.0118 2σ

Table D.3 LA-ICP-MS Data for KN14-22

Analysis	Spot Size (µm)	Al (ppm)	2σ	Zr (ppm)	2σ	T (°C)[1]	2σ	U (ppm)	2σ	$^{238}U/^{206}Pb$	2σ	$^{207}Pb/^{206}Pb$	2σ	Rho	Age (Ma)[2]	2σ
51	40	30900	460	173.5	3.3	809	12	189.1	3.1	215.5	6.5	0.3400	0.0210	0.5	19.1	1.2
52	40	28850	440	311.2	5.7	845	13	210.2	3.4	149.7	5.4	0.5640	0.0250	0.1	15.8	1.5
53	40	32780	450	246.4	4	830	13	182.2	3.3	199.2	8.7	0.4210	0.0300	0.2	15.7	1.5
54	40	33510	500	299.3	4.3	842	13	195.7	3.3	251.9	10.2	0.3500	0.0240	0.2	16.1	1.1
55	40	35510	570	254.7	4.2	832	13	174.3	4.2	243.9	10.7	0.3240	0.0260	0.4	17.4	1.3
56	25	31700	1600	261.1	7	834	13	185.9	5.3	153.1	8.2	0.4840	0.0410	0.5	19.5	2.7
57	25	40900	2500	230.5	6.2	826	13	179.0	4.4	216.0	13.5	0.3820	0.0510	0.6	17.6	2.6
58	25	41300	3000	218.9	7.1	823	13	184.5	6.3	205.3	13.1	0.4200	0.0530	0.5	17.0	2.7
59	40	39760	580	239.2	3.4	828	13	190.5	2.4	257.7	10.0	0.3340	0.0230	0.4	16.2	1.1
60	40	35610	510	160.9	3.2	805	12	182.3	2.5	246.3	9.1	0.3200	0.0240	0.4	17.4	1.2
61	40	33490	460	202.4	3.6	818	13	199.3	2.5	238.1	9.1	0.3340	0.0230	0.6	17.5	1.3
62	40	34860	480	210.5	2.7	821	12	201.0	2.4	160.0	5.4	0.5230	0.0240	0.1	16.8	1.4
63	40	138000	6600	142.9	4.6	798	13	90.9	3.0	6.0	0.4	0.8550	0.0200	0.4	12.0	29.0
64	40	31330	500	214.3	3.5	822	13	203.7	3.6	185.2	7.5	0.4320	0.0260	-0.4	18.4	1.1
65	40	39300	650	229.5	4.4	826	13	193.8	3.8	253.2	9.6	0.3360	0.0220	0.4	16.4	1.1
66	40	38830	640	346.6	6.6	851	13	188.0	3.9	152.9	5.1	0.5780	0.0230	0.3	14.7	1.4
67	40	34790	640	227.6	5.9	825	13	212.6	3.1	176.4	6.5	0.4600	0.0230	0.3	18.0	1.4
68	40	39370	580	184.8	3	813	12	200.5	3.0	183.8	13.2	0.4630	0.0350	-0.4	17.2	1.5
69	40	39740	580	190.2	3	815	12	221.6	3.7	214.6	6.9	0.4060	0.0220	0.3	16.8	1.1
70	40	30670	400	175.3	3	810	12	215.6	3.2	217.9	8.1	0.3210	0.0190	0.4	19.6	1.2
71	40	35180	470	348.4	5.2	852	13	228.0	3.1	56.5	2.7	0.7340	0.0170	0.2	18.1	2.9
72	40	40400	650	186.2	3.1	813	12	221.4	3.6	263.2	9.0	0.3220	0.0200	0.4	16.2	1.0
73	40	38790	600	247.2	4.4	830	13	197.8	2.8	254.5	7.8	0.3900	0.0240	0.4	14.7	1.0
74	40	19470	310	158.1	3.1	804	12	280.5	4.5	168.1	4.2	0.3580	0.0180	0.5	23.7	1.3
75	40	19630	320	157.8	2.8	804	12	271.6	3.5	153.6	6.1	0.4350	0.0200	0.0	22.0	1.4
76	40	19920	320	160	3.2	804	12	317.3	4.2	156.3	4.4	0.3980	0.0180	0.2	23.5	1.2
77	40	38840	600	152.3	2.8	801	12	209.7	2.6	242.7	7.7	0.4130	0.0240	0.6	14.6	1.1
78	40	20360	290	166.4	3.1	807	12	334.3	4.0	140.1	6.5	0.4500	0.0220	-0.4	23.3	1.2
79	40	39600	600	143.1	2.7	798	12	200.4	3.3	270.3	9.5	0.3700	0.0280	0.5	14.4	1.1

[1]Calculated at 12.9 kbar
[2]Initial $^{207}Pb/^{206}Pb$ = 0.8904 ± 0.0629 2σ

Table D.4   LA-ICP-MS Data for KN14-24A

Analysis	Spot Size (μm)	Al (ppm)	2σ	Zr (ppm)	2σ	T (°C)[1]	2σ	U (ppm)	2σ	^{238}U/^{206}Pb	2σ	^{207}Pb/^{206}Pb	2σ	Rho	Age (Ma)[2]	2σ
50	40	11300	1200	140.0	10.0	762	14	90.3	7.9	46.3	2.8	0.7070	0.0240	-0.1	22.9	5.2
51	40	11230	220	1260.0	28.0	900	14	315.7	8.4	4.8	0.1	0.0881	0.0021	0.2	1201.0	140.0
53	40	21730	570	223.7	6.4	789	13	184.4	6.4	82.4	2.8	0.6230	0.0280	0.3	21.2	3.3
54	40	19000	400	154.1	3.1	767	12	62.9	1.7	41.0	1.4	0.7270	0.0260	0.5	21.9	6.4
55	40	21430	440	221.2	5.4	788	13	163.5	5.0	89.0	2.7	0.6320	0.0260	0.4	18.8	2.9
56	40	21120	410	272.5	5.4	800	13	207.3	5.4	116.0	5.5	0.5260	0.0230	-0.2	21.9	1.9
57	40	19750	540	261.9	6.3	798	13	164.4	6.2	112.7	4.2	0.5520	0.0240	0.4	20.6	2.3
58	40	20460	310	150.7	2.5	766	12	269.9	4.7	117.0	2.6	0.4680	0.0170	0.4	25.7	1.6
59	40	19890	340	146.0	2.5	764	12	174.8	2.5	88.3	2.2	0.5570	0.0190	0.5	25.8	2.4
60	40	19890	350	149.2	2.7	765	12	179.3	2.8	88.0	2.1	0.5600	0.0170	0.4	25.7	2.2
61	40	20180	310	147.2	2.5	765	12	172.4	2.3	85.3	2.1	0.5690	0.0170	0.5	25.6	2.4
62	40	19890	320	149.3	3.1	765	12	202.4	3.5	56.9	1.2	0.6750	0.0160	0.6	23.2	3.4
63	40	25540	490	262.1	4.8	798	13	186.3	2.8	109.3	3.7	0.6130	0.0250	0.3	16.7	2.3
64	40	19450	380	278.9	5.0	802	13	231.4	4.2	130.7	3.6	0.4830	0.0220	0.6	22.1	1.9
65	40	19400	450	275.2	4.9	801	13	233.1	4.5	126.9	3.1	0.4640	0.0200	0.4	24.0	1.7
66	40	17400	350	128.8	2.5	757	12	120.8	2.0	56.6	1.5	0.6860	0.0240	0.5	21.8	4.4
67	40	13690	590	159.6	2.9	769	12	211.3	3.1	51.6	2.0	0.6670	0.0180	-0.1	26.9	3.8
68	40	15010	500	174.5	2.9	774	12	225.4	3.2	69.3	1.6	0.6340	0.0200	0.6	23.9	3.2

Analysis	Spot Size (µm)	Al (ppm)	2σ	Zr (ppm)	2σ	T (°C)[1]	2σ	U (ppm)	2σ	$^{238}U/^{206}Pb$	2σ	$^{207}Pb/^{206}Pb$	2σ	Rho	Age (Ma)[2]	2σ
69	40	17160	330	128.4	2.7	757	12	124.2	1.8	54.9	1.2	0.6560	0.0200	0.6	26.9	4.0
70	40	19600	370	161.9	3.7	770	12	92.0	2.4	44.9	1.3	0.7300	0.0280	0.6	19.4	6.1
71	40	19370	320	293.3	6.4	805	13	220.6	8.2	133.2	7.1	0.5220	0.0260	-0.2	19.3	1.8
72	40	26130	550	277.2	5.3	801	13	160.8	3.2	189.0	8.2	0.4040	0.0300	0.6	18.7	1.9
73	40	16070	600	154.7	3.5	767	12	193.1	3.8	73.3	2.4	0.5960	0.0250	0.5	26.8	3.6
74	40	15360	660	142.7	3.2	763	12	194.7	3.7	71.8	1.7	0.6340	0.0190	0.3	23.1	2.9
75	40	19220	340	161.8	3.0	770	12	321.8	5.2	113.6	3.1	0.5180	0.0180	0.5	22.9	1.9
76	40	19720	360	167.5	3.1	772	12	327.5	6.2	114.7	2.8	0.5250	0.0160	0.4	22.2	1.7
77	40	16970	750	280.7	5.9	802	13	209.9	4.4	107.0	3.3	0.5500	0.0210	0.3	21.9	2.1
78	40	19170	420	289.4	5.9	804	13	199.0	3.9	74.0	1.8	0.6630	0.0260	0.5	19.2	3.5

[1]Calculated at 9.4 kbar

[2]Initial $^{207}Pb/^{206}Pb = 0.8422 \pm 0.0251$ 2σ

Table D.5   LA-ICP-MS Data for KN14-56B

Analysis	Spot Size (µm)	Al (ppm)	2σ	Zr (ppm)	2σ	T (°C)[1]	2σ	U (ppm)	2σ	^{238}U/^{206}Pb	2σ	^{207}Pb/^{206}Pb	2σ	Rho	Age (Ma)[2]	2σ
53	25	15580	280	100.5	3.0	762	12	37.5	0.8	43.7	2.3	0.6440	0.0580	0.6	29.0	12.0
54	25	15420	280	99.5	3.2	762	12	37.7	1.1	43.9	2.9	0.6580	0.0680	0.6	26.0	14.0
55	25	15050	340	100.0	2.5	762	12	34.9	1.2	43.3	2.4	0.6260	0.0610	0.8	32.0	13.0
56	25	15400	350	144.0	9.3	782	14	27.0	1.0	27.5	1.4	0.6480	0.0590	0.6	44.0	20.0
57	25	15510	290	100.8	3.2	763	12	21.0	0.6	26.2	1.8	0.7400	0.0780	0.8	16.0	26.0
58	25	23920	540	98.3	3.2	761	12	73.7	2.2	52.9	6.4	0.6400	0.0580	0.2	24.0	10.0
59	25	22860	590	95.7	2.8	760	12	85.2	3.5	116.4	8.4	0.5670	0.0510	0.5	16.5	4.5
60	25	12450	210	100.6	3.2	762	12	22.2	0.8	26.9	1.7	0.7070	0.0630	0.7	26.0	21.0
61	25	12480	260	103.8	3.0	764	12	21.3	0.8	26.8	1.7	0.7120	0.0790	0.8	25.0	26.0
62	25	21650	460	94.2	3.5	759	12	64.8	2.2	85.7	6.0	0.6110	0.0510	0.1	18.0	5.3
63	25	23930	420	81.9	3.1	751	12	62.8	1.7	104.9	7.9	0.6020	0.0760	0.8	15.4	7.2
64	25	26000	3500	56.9	7.5	732	18	42.9	5.4	12.2	8.0	0.7560	0.0990	-0.7	23.0	60.0
65	25	15430	300	83.6	2.7	752	12	30.3	0.9	43.5	3.0	0.7340	0.0780	0.8	11.0	16.0
66	25	18690	400	89.5	3.0	756	12	39.2	1.4	56.5	3.8	0.6020	0.0700	0.7	29.0	12.0
67	25	23150	440	92.2	3.3	758	12	74.0	1.9	105.4	7.1	0.5460	0.0580	0.6	19.9	5.6
68	25	21780	410	87.5	3.3	755	12	59.5	3.0	95.9	7.0	0.6030	0.0670	0.6	16.8	6.7
69	25	12140	240	87.6	3.3	755	12	13.6	0.8	14.4	1.2	0.7930	0.0610	0.5	-3.0	36.0
70	25	10890	230	103.1	2.8	764	12	27.2	1.1	30.4	1.9	0.6690	0.0570	0.4	34.0	17.0
71	25	11120	250	106.0	3.2	765	12	30.2	1.2	32.6	1.7	0.6370	0.0480	0.5	40.0	14.0
72	25	11720	230	102.7	3.2	764	12	36.9	1.2	40.0	2.6	0.6650	0.0570	0.6	27.0	13.0
73	25	19040	470	87.7	2.7	755	12	49.4	2.3	71.4	5.6	0.6010	0.0590	0.7	22.7	8.4
74	25	16650	610	90.2	3.3	756	12	39.1	1.3	45.5	4.1	0.6750	0.0560	0.3	22.0	11.0
75	25	11340	290	88.6	4.0	756	13	34.6	1.7	22.2	1.9	0.4410	0.0520	0.7	135.0	29.0
76	25	21270	410	81.3	2.7	751	12	46.3	1.4	116.3	8.5	0.7090	0.0890	0.9	5.9	6.9
77	25	10950	210	89.9	3.5	756	12	33.9	2.0	18.1	1.0	0.3710	0.0420	0.7	129.0	28.0
78	25	12060	260	97.0	2.7	760	12	25.9	0.9	32.8	1.9	0.7340	0.0670	0.8	14.0	18.0
79	40	15220	560	140.7	1.9	781	12	50.4	1.0	36.4	1.1	0.5830	0.0210	0.4	48.8	5.8
80	40	16130	640	147.8	2.9	784	12	43.0	0.7	32.6	0.9	0.5540	0.0220	0.6	62.1	7.1
81	40	16770	580	124.5	2.9	774	12	46.6	0.8	34.8	1.5	0.6050	0.0240	0.5	45.6	7.2

Analysis	Spot Size (µm)	Al (ppm)	2σ	Zr (ppm)	2σ	T (°C)[1]	2σ	U (ppm)	2σ	$^{238}U/^{206}Pb$	2σ	$^{207}Pb/^{206}Pb$	2σ	Rho	Age (Ma)[2]	2σ
82	40	18620	610	119.2	2.5	772	12	135.1	2.3	138.5	5.0	0.3820	0.0200	0.5	25.4	1.8
83	40	28960	460	116.2	2.6	770	12	112.8	2.2	78.3	5.0	0.5310	0.0250	-0.2	28.5	2.8
84	25	28050	560	110.9	2.3	768	12	28.9	1.3	27.9	4.0	0.7510	0.0690	0.4	12.0	22.0
85	25	14620	260	97.3	3.2	761	12	32.7	0.8	44.4	2.8	0.6500	0.0620	0.7	27.0	13.0
86	25	21310	360	89.6	2.8	756	12	53.0	1.8	58.5	5.1	0.6260	0.0590	0.2	24.1	9.3
87	25	21890	400	87.1	2.9	755	12	54.2	1.2	50.0	7.5	0.7160	0.0640	0.3	13.0	12.0
88	25	24140	460	27.9	1.6	697	12	37.2	1.0	151.1	16.4	0.7600	0.2100	0.8	2.0	12.0
89	25	23750	380	31.1	1.6	702	12	34.3	0.9	133.7	14.3	0.7900	0.1500	0.7	-0.9	9.6
90	25	27750	410	118.4	3.3	771	12	78.9	1.9	127.4	8.1	0.5770	0.0700	0.7	14.4	5.4
91	25	25670	390	129.2	3.4	776	12	111.8	2.3	227.8	14.5	0.4790	0.0470	0.8	11.8	2.4
92	25	23960	450	120.4	3.9	772	12	58.9	1.5	71.4	5.1	0.6140	0.0480	0.3	21.2	6.4
93	25	25040	390	100.7	3.3	762	12	47.7	1.5	69.4	6.8	0.6250	0.0610	0.5	20.4	8.6
94	25	26730	400	104.0	2.9	764	12	65.9	1.6	109.2	7.0	0.5280	0.0530	0.5	20.7	4.9
95	25	23590	430	107.7	3.3	766	12	44.8	1.0	69.0	6.2	0.6590	0.0700	0.7	16.3	9.7
96	25	27370	360	112.5	3.2	769	12	95.3	1.7	141.4	8.2	0.4450	0.0590	0.8	21.1	4.6
97	25	27350	880	82.3	5.9	752	14	27.1	2.2	8.2	1.7	0.8020	0.0420	0.1	-15.0	45.0
98	25	19610	680	99.1	5.7	762	13	38.0	2.1	16.9	3.7	0.7500	0.0560	0.4	20.0	30.0
99	25	11560	200	100.9	4.4	763	13	38.5	0.9	28.5	1.4	0.4880	0.0460	0.6	91.0	17.0
100	25	13340	230	123.7	3.2	774	12	43.6	0.8	43.1	1.9	0.6720	0.0530	0.6	23.0	11.0

[1]Calculated at 11.3 kbar

[2]Initial $^{207}Pb/^{206}Pb$ = 0.7887 ± 0.0202 2σ

Table D.6   LA-ICP-MS Data for KN14-53A

Analysis	Spot Size (µm)	Al (ppm)	2σ	Zr (ppm)	2σ	T (°C)[1]	2σ	U (ppm)	2σ	^{238}U/^{206}Pb	2σ	^{207}Pb/^{206}Pb	2σ	Rho	Age (Ma)[2]	2σ
11	25	14350	250	100.2	3.0	754	12	67.3	1.3	224.7	15.1	0.4960	0.0690	0.7	9.8	7.3
12	25	13760	250	101.5	2.9	755	12	64.9	1.6	170.9	13.1	0.5090	0.0710	0.8	12.0	10.0
13	25	11840	270	94.1	3.7	751	12	72.0	2.6	167.8	11.5	0.5070	0.0720	0.7	13.0	10.0
14	25	15800	1000	103.6	8.0	756	14	93.6	7.0	126.6	24.0	0.6240	0.0910	0.5	8.0	17.0
15	25	10580	190	108.3	3.1	759	12	89.1	2.3	152.4	8.1	0.4240	0.0420	0.6	18.9	7.1
16	25	11490	210	97.3	3.3	753	12	73.7	1.6	108.2	10.3	0.5560	0.0540	0.4	15.0	12.0
17	25	14780	700	121.2	4.0	765	12	182.1	5.6	245.1	13.8	0.3090	0.0300	0.5	16.2	3.9
18	25	10520	160	109.6	3.1	759	12	81.7	1.6	101.1	7.3	0.6300	0.0590	0.4	9.0	13.0
19	25	6340	470	38.8	3.6	705	14	88.8	6.5	106.2	6.1	0.5600	0.0440	0.4	15.1	9.4
20	25	25340	460	87.6	2.6	747	12	147.3	2.5	370.4	27.4	0.3870	0.0540	0.7	8.7	4.1
21	25	23080	340	81.0	4.7	743	13	143.2	6.2	274.0	31.5	0.4210	0.0530	0.1	10.6	4.9
22	25	8860	250	29.2	3.1	692	15	126.0	9.7	97.5	7.1	0.4080	0.0440	0.6	31.0	13.0
23	25	23040	660	103.2	3.7	756	12	188.2	5.1	409.8	31.9	0.2970	0.0470	0.5	10.0	3.5
24	25	9530	160	172.2	4.1	785	12	198.2	3.6	72.5	7.4	0.5910	0.0390	-0.2	18.0	11.0
25	25	22570	340	127.4	3.1	768	12	124.8	2.1	216.5	28.6	0.4790	0.0630	0.4	10.9	7.8
26	25	12380	190	116.6	2.7	763	12	104.6	2.3	201.6	11.0	0.3840	0.0400	0.5	16.2	5.3
27	40	12180	550	137.6	3.0	772	12	77.5	1.6	70.7	2.5	0.4060	0.0230	0.5	43.1	8.9
28	40	11350	610	178.5	4.1	787	12	99.6	2.7	83.8	2.7	0.3290	0.0170	0.3	45.0	6.1
29	40	8300	270	171.3	3.7	784	12	145.0	2.9	68.2	1.7	0.4160	0.0160	0.1	43.3	5.7
30	25	21710	370	115.0	3.3	762	12	166.2	3.6	442.5	29.4	0.3710	0.0590	0.6	7.6	3.5
31	25	22070	350	107.1	2.9	758	12	166.9	2.8	420.2	30.0	0.2650	0.0370	0.4	10.4	2.8
32	25	10600	190	104.2	3.2	757	12	82.0	1.9	186.6	19.8	0.5370	0.0590	0.7	9.7	8.2
33	25	11250	230	105.4	3.8	757	12	81.8	1.9	195.7	18.0	0.5110	0.0720	0.8	10.5	9.3
34	25	10550	150	103.5	5.1	756	13	172.9	7.0	310.6	16.4	0.3040	0.0380	0.3	12.9	3.2
35	25	10550	230	102.3	2.8	756	12	91.2	2.4	155.0	12.0	0.6130	0.0550	0.5	7.1	7.9
36	25	11030	180	103.9	3.1	756	12	81.7	2.3	161.3	9.1	0.5180	0.0490	0.7	12.4	7.3
37	25	22250	410	118.5	3.6	764	12	150.4	4.6	339.0	25.3	0.3340	0.0400	0.3	11.0	3.4
38	25	11740	260	127.2	3.5	767	12	158.0	4.6	312.5	19.5	0.3940	0.0490	1.0	10.1	4.5

[1]Calculated at 10.5 kbar,
[2]Initial ^{207}Pb/^{206}Pb = 0.7522 ± 0.1015 2σ

Table D.7 LA-ICP-MS Data for KN14-33B

Analysis	Spot Size (μm)	Al (ppm)	2σ	Zr (ppm)	2σ	T (°C)[1]	2σ	U (ppm)	2σ	$^{238}U/^{206}Pb$	2σ	$^{207}Pb/^{206}Pb$	2σ	Rho	Age (Ma)[2]	2σ
11	40	5090	340	145.7	4.2	802	13	394.0	12.0	183.8	10.8	0.3750	0.0430	0.7	20.6	4.9
12	40	5760	270	168.0	5.1	810	13	405.0	12.0	178.3	12.4	0.3420	0.0390	0.6	22.7	5.1
13	40	6880	180	115.0	3.9	788	12	289.1	9.4	178.9	16.0	0.3560	0.0390	0.5	22.0	5.5
14	40	7050	180	113.9	3.7	788	12	304.0	10.0	188.7	14.2	0.4040	0.0470	0.5	18.8	5.1
15	40	5700	230	144.0	6.5	801	13	435.0	16.0	210.1	15.0	0.3680	0.0540	0.7	18.3	5.3
16	40	6250	190	125.4	5.2	793	13	396.0	14.0	213.2	18.6	0.3250	0.0450	0.9	19.7	5.7
17	40	4100	320	103.1	2.7	782	12	465.0	15.0	230.4	19.6	0.3990	0.0440	0.7	15.6	4.5
18	40	7320	150	110.1	3.3	786	12	199.6	5.3	198.8	12.6	0.4690	0.0530	0.5	15.2	4.8
19	40	6510	140	111.5	3.1	787	12	382.8	9.5	208.8	10.9	0.3150	0.0330	0.4	20.5	3.4
20	40	4720	290	162.5	4.3	808	13	387.2	7.6	163.4	8.3	0.4170	0.0380	0.5	21.1	4.5
21	40	2254	37	283.5	4.5	842	13	1394.0	20.0	240.4	6.4	0.1900	0.0100	0.4	22.0	1.3
22	40	2281	35	277.0	4.3	840	13	1429.0	21.0	229.6	5.0	0.1970	0.0098	0.5	22.7	1.2
23	40	3300	190	253.0	4.3	835	13	974.0	14.0	150.8	8.2	0.3850	0.0230	-0.5	24.6	2.2
24	40	2316	42	167.6	3.0	810	12	781.0	11.0	221.2	7.3	0.2330	0.0160	0.5	22.3	2.0
25	40	2317	51	170.8	2.8	811	12	778.0	11.0	216.9	6.1	0.2280	0.0170	0.3	22.9	1.8
26	40	5870	130	143.7	3.1	801	12	259.9	5.4	179.9	8.7	0.4120	0.0390	0.4	19.4	3.9
27	40	2208	82	130.7	3.6	796	12	188.6	3.6	174.2	10.9	0.5270	0.0520	0.7	14.7	5.3
28	40	6050	110	140.6	3.3	800	12	369.8	6.5	223.2	10.5	0.3040	0.0290	0.6	19.5	3.0
29	40	2113	46	174.4	5.0	812	13	1113.0	22.0	235.8	6.1	0.2280	0.0160	0.5	21.1	1.6
30	25	7580	200	355.0	10.0	856	13	703.0	18.0	393.7	18.6	0.1620	0.0140	0.4	14.0	1.4
31	25	7470	180	97.9	4.1	779	13	156.7	4.1	359.7	31.1	0.3240	0.0630	0.4	11.7	3.4
32	25	7540	270	101.1	5.0	781	13	171.0	6.2	366.3	34.9	0.4600	0.1100	0.2	8.5	4.7
33	25	10040	320	100.4	4.3	781	13	545.0	16.0	515.5	31.9	0.1540	0.0220	0.3	10.8	1.5
34	40	6360	270	140.4	4.1	800	12	328.9	9.0	228.8	14.1	0.3110	0.0330	0.4	18.8	3.3
35	40	7190	130	148.7	4.0	803	12	366.7	6.8	214.6	9.7	0.2750	0.0290	0.6	21.4	3.1
36	40	6760	200	200.6	4.3	821	13	269.1	5.7	197.6	13.3	0.3230	0.0300	0.5	21.3	3.9
37	40	6550	220	197.1	4.0	820	13	221.7	5.9	180.8	12.1	0.3340	0.0390	0.3	22.8	4.5
38	40	7430	140	189.8	3.9	817	13	186.2	4.3	193.8	11.6	0.3740	0.0380	0.4	19.6	3.9
39	40	7380	130	155.7	3.5	806	12	147.6	3.1	167.8	10.4	0.3650	0.0370	0.6	23.0	5.0
40	40	7960	150	162.5	3.0	808	12	170.5	3.3	183.5	11.1	0.3860	0.0350	0.3	20.2	3.9

[1]Calculated at 13.2 kbar
[2]Initial $^{207}Pb/^{206}Pb = 0.8469 \pm 0.0552$ 2σ

Table D.8   LA-ICP-MS Data for KN14-51A

Analysis[1]	Spot Size (µm)	Al (ppm)	2σ	Zr (ppm)	2σ	T (°C)[2]	2σ	U (ppm)	2σ	$^{238}U/^{206}Pb$	2σ	$^{207}Pb/^{206}Pb$	2σ	Rho	Age (Ma)[3]	2σ
59	25	10660	230	203.4	6.1	793	13	502.3	9.4	319.5	16.3	0.2430	0.0220	0.5	15.5	2.4
60	25	11230	310	162.8	6.0	780	13	376.0	11.0	321.5	18.6	0.1940	0.0230	0.7	16.5	2.9
61	25	12010	330	73.4	4.1	737	13	202.9	6.6	296.7	23.8	0.3270	0.0470	0.5	14.5	4.2
62	25	12250	320	78.7	3.3	741	12	205.6	5.1	282.5	28.7	0.3400	0.0710	0.8	14.9	6.7
63	25	11280	230	290.2	9.0	814	13	324.0	12.0	293.3	18.1	0.2500	0.0290	0.4	16.7	3.1
64	25	10950	210	240.0	13.0	803	14	251.6	7.5	288.2	19.1	0.2750	0.0390	0.6	16.3	3.9
74	25	11310	280	250.8	7.4	806	13	652.0	15.0	220.8	7.3	0.3390	0.0210	0.5	19.1	2.5
75	25	11570	330	247.0	13.0	805	14	565.0	27.0	289.9	12.6	0.3040	0.0300	0.5	15.5	2.6
76	25	11220	280	252.7	5.9	806	13	785.0	21.0	252.5	9.6	0.3130	0.0190	0.4	17.5	2.2
77	25	10260	260	253.5	8.1	806	13	664.0	18.0	304.0	12.9	0.2110	0.0200	0.4	17.1	2.2
78	25	9320	260	140.6	5.0	772	13	406.0	13.0	261.1	13.0	0.3410	0.0300	0.4	16.1	3.0
79	25	9530	240	233.8	6.2	801	13	548.0	11.0	278.6	12.4	0.2190	0.0230	0.3	18.4	2.4
80	25	14770	360	96.0	3.6	751	12	134.3	4.0	291.5	26.3	0.4340	0.0770	0.8	12.0	6.1
81	25	10640	280	91.6	3.8	749	12	132.9	2.8	246.9	18.3	0.4010	0.0570	0.5	15.5	5.2
1	25	13020	290	109.4	6.1	758	12	127.0	3.4	255.8	21.6	0.5220	0.0940	0.7	10.9	3.5
2	25	13480	270	118.0	5.8	762	11	127.9	3.7	295.0	24.4	0.3700	0.0590	0.5	13.4	3.2
3	25	13340	360	111.6	4.8	759	11	130.2	3.3	367.6	32.4	0.3990	0.0760	0.9	10.1	2.4
4	25	13760	350	121.7	4.2	764	11	127.2	4.3	350.9	32.0	0.4370	0.0740	0.6	9.8	2.3
5	25	13270	250	123.8	5.3	765	11	118.5	2.8	339.0	27.6	0.4260	0.0650	0.6	10.4	2.0
6	25	14310	240	129.7	6.0	768	11	112.8	3.7	139.5	9.9	0.5900	0.0800	0.6	16.2	5.2
7	25	14220	260	95.8	4.1	751	11	102.3	3.1	149.9	16.6	0.4720	0.0760	0.7	21.1	5.8
8	25	13170	290	416.0	23.0	837	13	476.0	17.0	340.1	17.4	0.2840	0.0270	0.5	13.6	1.1
9	25	13920	300	121.3	4.8	764	11	129.5	2.5	175.7	17.9	0.4240	0.0800	0.7	20.1	5.1
10	25	14200	290	143.5	4.1	773	10	105.5	3.0	143.9	13.7	0.5000	0.1100	1.0	20.5	7.7
11	25	14000	280	109.2	5.8	758	11	105.8	5.4	118.3	8.5	0.4800	0.0550	0.7	26.2	5.0
12	25	16010	930	257.0	10.0	807	11	214.0	9.1	214.1	17.9	0.3080	0.0550	0.5	20.7	3.1
13	25	25200	3700	278.0	14.0	812	12	183.4	7.2	148.8	14.8	0.3870	0.0520	0.3	25.6	4.2
14	25	13880	280	132.6	5.5	769	11	81.9	2.4	126.6	11.5	0.5700	0.1500	1.0	19.0	11.0
15	25	14620	220	122.9	5.3	765	11	93.0	2.2	141.4	13.6	0.5810	0.0920	0.7	16.4	6.1

Analysis[1]	Spot Size (µm)	Al (ppm)	2σ	Zr (ppm)	2σ	T (°C)[2]	2σ	U (ppm)	2σ	$^{238}U/^{206}Pb$	2σ	$^{207}Pb/^{206}Pb$	2σ	Rho	Age (Ma)[3]	2σ
16	25	14260	360	146.2	5.9	774	11	166.4	3.9	154.6	12.9	0.3950	0.0600	0.5	24.3	4.2
17	25	14640	370	114.5	5.5	761	11	168.9	3.8	204.1	17.9	0.2740	0.0570	0.8	23.0	3.9
18	25	13940	270	94.7	3.7	750	11	203.3	5.5	321.5	21.7	0.3160	0.0550	0.6	13.6	2.0
19	25	14370	290	103.7	4.1	755	11	164.0	5.6	158.5	18.8	0.5070	0.0710	0.3	18.3	4.6
20	25	13240	320	174.1	7.1	784	11	282.8	8.2	349.7	22.0	0.2610	0.0390	0.4	13.7	1.4
21	25	13090	260	145.2	4.4	774	11	207.1	5.2	299.4	24.2	0.3710	0.0450	0.5	13.2	1.9
22	25	13080	330	218.9	6.1	797	11	401.9	8.2	497.5	29.7	0.2150	0.0300	0.4	10.3	0.9
23	25	11170	840	256.0	20.0	807	14	446.0	35.0	229.4	17.4	0.2120	0.0540	0.5	22.5	3.0
24	25	14570	260	134.9	6.0	770	11	119.0	3.2	168.4	17.9	0.3900	0.0810	0.5	22.5	5.3
25	25	14740	250	127.4	5.4	767	11	77.8	3.7	157.7	16.7	0.5090	0.0810	0.4	18.2	5.0
26	25	13760	260	186.2	7.0	788	11	295.9	8.1	208.3	12.2	0.2070	0.0310	0.3	25.0	2.1
27	25	15090	290	134.4	4.8	770	11	38.7	1.3	137.2	18.3	0.8800	0.2800	0.9	0.0	28.0
28	25	19170	380	167.0	6.5	782	11	97.5	3.4	125.6	13.1	0.5300	0.1000	0.8	21.6	7.9

[1]40µm spots 65-73 did not have standards post run, and are therefore removed.
[2]Calculated at 10.4 kbar
[3]Initial $^{207}Pb/^{206}Pb$ = 0.9167 ± 0.1383 2σ

Table D.8 LA-ICP-MS Data for KN14-50A

Analysis	Spot Size (µm)	Al (ppm)	2σ	Zr (ppm)	2σ	T (°C)[1]	2σ	U (ppm)	2σ	^{238}U/^{206}Pb	2σ	^{207}Pb/^{206}Pb	2σ	Rho	Age (Ma)[2]	2σ
101	40	25530	390	162.6	3.3	780	12	91.4	1.7	162.9	5.6	0.4070	0.0270	0.5	24.2	1.8
102	40	24910	420	140.4	2.7	772	12	73.9	1.4	144.3	6.9	0.5280	0.0370	0.5	21.5	2.6
103	40	24520	410	166.3	4.3	782	12	70.6	2.3	136.2	5.8	0.4720	0.0350	0.6	25.6	2.8
104[3]	25	4190	720	22.7	4.7	679	22	33.9	6.5	222.2	64.2	0.8100	0.4100	0.8	5.0	14.0
105	25	13350	640	171.3	5.7	783	13	96.6	2.4	220.8	17.1	0.4890	0.0570	0.7	15.3	2.8
106	25	11120	230	80.3	2.6	742	12	97.5	2.1	310.6	25.1	0.4060	0.0670	0.4	12.7	2.1
107	25	13610	610	74.0	2.4	737	12	86.2	2.8	317.5	24.2	0.4470	0.0580	0.4	11.6	1.8
108	25	14680	260	150.7	3.4	776	12	76.8	1.2	168.6	12.2	0.4980	0.0740	0.6	19.7	4.1
109	25	12240	190	159.5	3.5	779	12	87.2	1.8	173.0	12.0	0.4330	0.0600	0.6	21.8	3.5
110	25	14160	230	422.0	12.0	838	13	160.3	3.7	189.4	13.3	0.3650	0.0500	0.4	22.4	2.8
111	25	13350	230	383.8	7.1	832	13	152.5	2.9	193.1	9.3	0.4430	0.0410	0.7	19.1	2.3
112	25	14030	490	72.5	3.1	736	12	120.0	6.0	214.6	23.9	0.4210	0.0780	0.4	17.9	3.8
113	25	16230	350	142.3	3.6	773	12	75.2	1.9	135.3	15.0	0.5600	0.0950	1.0	21.4	7.8
114	25	13110	220	179.0	4.0	786	12	141.3	1.9	216.9	11.3	0.3740	0.0340	0.7	19.2	1.9
115	25	13290	210	393.6	6.8	833	13	195.9	3.4	220.3	11.6	0.3130	0.0330	0.4	20.9	1.8
116	25	14480	220	155.2	3.3	778	12	75.2	1.2	159.5	9.2	0.4480	0.0650	0.7	23.0	3.9
117	25	14290	250	181.4	4.2	787	12	98.0	1.9	171.8	11.2	0.4940	0.0560	0.6	19.5	3.2
118	25	15250	260	223.1	8.4	799	13	110.0	1.7	176.4	10.3	0.4350	0.0460	0.4	21.3	2.6
119[3]	25	15750	370	146.3	5.2	774	13	52.8	1.9	133.3	19.6	0.8300	0.3800	1.0	8.0	21.0
120	25	14140	290	538.0	17.0	853	14	123.0	3.6	164.5	10.8	0.4240	0.0720	0.6	23.3	4.1
121[3]	25	15890	450	188.8	8.0	789	13	48.4	1.4	138.9	21.2	0.8100	0.1800	0.8	8.0	10.0
122	25	14820	270	143.4	4.3	773	12	48.8	1.2	129.5	13.4	0.6300	0.1200	0.8	18.6	7.9
123	25	15490	250	128.1	3.7	767	12	40.8	1.0	123.5	13.0	0.6180	0.0850	0.5	20.2	6.2
124	25	14790	370	500.0	11.0	848	13	57.8	1.7	107.8	9.8	0.5810	0.0910	0.2	25.5	6.7
125[3]	25	15640	480	155.0	7.8	778	13	70.2	2.1	184.8	24.6	0.7000	0.3400	1.0	11.0	14.0
126	25	15640	310	140.7	3.5	772	12	64.2	1.6	164.5	14.3	0.5470	0.0850	0.7	18.1	4.8
127	25	16490	350	173.7	4.9	784	13	65.0	2.3	160.5	16.5	0.5960	0.0970	0.7	16.5	5.5
128	25	14340	270	186.9	4.7	788	13	68.0	2.4	144.3	15.0	0.4200	0.1000	0.7	26.7	7.0

[1]Calculated at 10.4 kbar
[2]Initial 207Pb/206Pb = 1.0180 ± 0.1758 2σ
[3]Quickly drilled through titanite, data not included in interpretations.